

Cornelia Lex

Maximum Tire-Road Friction Coefficient Estimation

Monographic Series TU Graz

Reihe Fahrzeugtechnik

Band 5

Herausgeber:
Institut für Fahrzeugtechnik

Monographic Series TU Graz

Cornelia Lex

Maximum Tire-Road Friction Coefficient Estimation

This work is based on the dissertation “*Estimation of the Maximum Coefficient of Friction between Tire and Road Based on Vehicle State Measurements*”, presented by Cornelia Lex at Graz University of Technology, Faculty of Mechanical Engineering and Economic Sciences, 2015

.

© 2015 Verlag der Technischen Universität Graz

Herausgeber	Institut für Fahrzeugtechnik
Layout	Alexander Harrich, Wolfgang Karl, Haymo Niederkofler, TU Graz
Druck	TU Graz / Büroservice

Verlag der Technischen Universität Graz

www.ub.tugraz.at/Verlag

ISBN (print) 978-3-85125-422-8

ISBN (e-book) 978-3-85125-423-5

DOI 10.3217/978-3-85125-422-8

<http://creativecommons.org/licenses/by-nc-nd/3.0/at/>



Erschienen in der Reihe Fahrzeugtechnik der Monographic Series

Band 1 Niederkofler, Haymo

Analyse radselektiv eingreifender Fahrdynamikregelsysteme für die Anwendung in Elektromechanischen Corner-Modulen, Dissertation, Verlag der TU Graz, ISBN978-3-85125-220-0, 2012

Band 2 Rojas Rojas, Andrés Eduardo

Passenger Vehicles with In-Wheel Motors: fundamentals, potentials and limitations, Dissertation, Verlag der TU Graz, ISBN 978-3-85125-234-7, 2012

Band 3 Daniel Wallner

Experimental and Numerical Investigations on Brake Squeal, Dissertation, Verlag der TU Graz, ISBN 978-3-85125-269-9, 2013

Band 4 Alexander Harrich

CAD-basierte Methoden zur Unterstützung der Karosseriekonstruktion in der Konzeptphase, Dissertation, Verlag der TU Graz, ISBN 978-3-85125- 420-4, 2015

Acknowledgement

I would like to thank Prof. Dr. Wolfgang Hirschberg for his supervision and for giving me the opportunity to do this research project as a scientific assistant at the Institute of Automotive Engineering at Graz University of Technology. I would also like to thank Prof. Dr. Bengt Jacobson from Chalmers University for his kind willingness to support my thesis as a second assessor.

At the Institute of Automotive Engineering, I would like to thank current and former colleagues as well as the students for all the discussions and the support. In particular, I offer my gratitude to Assoc.Prof. Dr. Arno Eichberger.

Although this project was not realised within an industry-funded research project, I had the chance to collaborate with and receive support from the following people outside our university: Prof. Dr. Gundolf Haase of the Institute of Mathematics and Scientific Computing of Graz University, Dipl.-Ing. (FH) Andreas Kerschbaumer of Virtual Vehicle Research Center, Graz, Dipl.-Ing. Friedrich Eppel of ÖAMTC, Vienna, and Dr. Hans-Ulrich Kobialka of Fraunhofer Institute for Intelligent Analysis and Information Systems, Bonn.

Finally, my deepest gratitude goes to my partner, my family and my friends for their incredible patience and encouragement.

Abstract

The extent to which a certain driver input causes a desired vehicle reaction depends strongly on the road and tire conditions. This also holds true for the interventions of advanced driver assistance systems (ADAS). ADAS are currently developed to meet requirements for accident prevention on dry roads. This is necessary in order to avoid incorrect ADAS interventions due to unreliable information. The present work describes a method for estimating the current road and tire conditions based on on-board sensors that measure and process the vehicle's dynamic state.

The first part of this thesis addresses the first research topic, namely determining which of the investigated vehicle state variables are sensitive to road and tire conditions, and are therefore theoretically suitable for estimating road and tire conditions. To this end, a sensitivity analysis was conducted by means of a two-track vehicle model described by a non-linear ordinary differential equation system. As expected, the wheel rotational speeds showed the highest sensitivity to the road and tire conditions for all investigated driving states. The second part of the thesis presents a method for estimating the road and tire conditions based on the sensor signals present in a vehicle equipped with electronic stability control. To this end, a particle filter is applied, which serves as a non-linear observer within the Bayesian probability framework and makes it possible to solve a state estimation problem while dealing with measurement noise and uncertainties. The research investigated whether the road and tire conditions can be estimated accurately enough to be used within the intervention strategy of an adaptive emergency brake system (AEB).

The results show that the proposed vehicle-dynamics-based method has the potential to improve existing techniques for estimating current road and tire conditions. Since the proposed method is based on the measurement of the dynamic reactions of the vehicle, the estimation accuracy increases with increasing dynamic excitation. The results demonstrate that the required accuracy for an AEB can be reached for certain driving states.

Kurzfassung

Straßen- und Reifenzustände beeinflussen maßgeblich, in welchem Ausmaß eine Fahrerinnen- und Fahrereingabe in eine Fahrzeugreaktion umgesetzt werden kann. Diese physikalischen Grenzen gelten auch für aktive Eingriffe von Fahrerassistenzsystemen. Fahrerassistenzsysteme, wie sie aktuell serienmäßig verfügbar sind, sind auf die Anforderungen auf trockener Fahrbahn ausgelegt, um Fehlauflösungen aufgrund von unsicheren Informationen zu vermeiden. In der vorliegenden Arbeit wird ein Verfahren zur Schätzung des aktuellen Straßen- und Reifenzustands vorgestellt, welches auf Messungen des fahrdynamischen Zustands des Fahrzeuges beruht. Als Basis für die verwendete Sensorik dient ein mit Elektronischer Stabilitätskontrolle ausgestattetes Fahrzeug.

Im ersten Teil der Arbeit wird die Forschungsfrage beantwortet, welche Fahrzustandsgrößen sensitiv auf eine Änderung des Straßen- und Reifenzustands reagieren, und damit zur Schätzung des aktuellen Straßen- und Reifenzustands theoretisch in Frage kommen. Dafür wird eine Sensitivitätsanalyse mit Hilfe eines Zweispurmodells durchgeführt, welches durch gewöhnliche Differentialgleichungen beschrieben ist. Für alle Fahrzustände zeigen die Raddrehzahlen die größte Sensitivität auf eine Änderung des Straßen- und Reifenzustands. Im zweiten Teil der Arbeit wird eine Methode zur fahrdynamikbasierten Schätzung von Straßen- und Reifenzustand vorgestellt. Dazu wird ein Partikelfilter verwendet, der nichtlineare Zustandsschätzung unter Verwendung von verrauschten Messwerten mit Hilfe des Bayes'schen Wahrscheinlichkeitsbegriffs ermöglicht. Es wird untersucht, ob die erreichten Schätzwerte genau genug sind, um die Auslösestrategie eines Automatisierten Notbremsassistenten (AEB) anpassen zu können.

Es wird gezeigt, dass das vorgeschlagene Verfahren Potential zur Verbesserung von bestehenden Methoden der Straßen- und Reifenzustandsschätzung bietet. Da es sich um ein Verfahren der Messung der dynamischen Reaktion des Fahrzeugs handelt, ist die Schätzergenauigkeit abhängig von der dynamischen Anregung während der Fahrt. Die notwendige Genauigkeit für einen AEB kann trotzdem über einige Fahrbereiche erreicht werden.

List of abbreviations

ACC	Adaptive cruise control
ABS	Anti-lock braking system
AD	Automatic differentiation
ADAS	Advanced driver assistance system
AEB	Automated emergency braking system
AFS	Active front steering system
AI	Alcohol detection and interlock system
ANN	Artificial neural network
ARB	Anti-roll bar
AuHi	Automated highway system
AWD	All-wheel drive
BA	Braking assist
C2C	Car-to-car communication system
C2I	Car-to-infrastructure communication system
C2x	Car-to-x communication system
CAN	Controller area network
CEN	European Committee for Standardization
CENELEC	European Committee for Electrotechnical Standardization
COG	Centre of gravity
CWS	Collision warning system
DLC	Double lane change manoeuvre
DOF	Degrees of freedom
DVM	Driver vigilance monitoring
EMA	Evasive manoeuvre assistant
ESC	Electronic stability control
ETSI	European Telecommunications Standards Institute

FWD	Front-wheel drive
GNSS	Global navigation satellite system
GSM	Global system for mobile communications
GPS	Global positioning system
ICA	Intersection collision avoidance system
ISO	International Organization for Standardization
LKA	Lane keeping assistant
LPB	Last point to brake
LPS	Last point to steer
LQ	Longitudinal-lateral manoeuvre
MAE	Mean absolute error
MEMS	Micro-electromechanical system
ODE	Ordinary differential equation
PDF	Probability density function
PID	Proportional-integral-derivative controller
PROMETHEUS	Programme for a European traffic of highest efficiency and unprecedented safety
QL	Lateral-longitudinal manoeuvre
SD	Standard deviation
SLS	Speed limiting system
TCS	Traction control system
TRFE	Tire road friction estimator
RNN	Recurrent neural network
VDC	Vehicle dynamics control
WDWS	Weather data management system
ZEDATU	Database for fatal accidents in Austria ¹

¹Abbreviation in German for **Z**entrale **D**atenbank zur **T**iefenanalyse von **V**erkehrsunfällen

List of symbols

Mathematical objects within this work are denoted as follows:

- a scalar,
- \mathbf{a} vector,
- \mathbf{A} matrix.

When present, symbols in sub- and superscripts of a variable x are used in the form ${}_1x_{2,3,4}^5$. The numbers denote the position of the following optional assignments:

- 1 ... the coordinate system, eg. b for *body*
- 2 ... a description or distinction, eg. r_e for *effective* tire radius
- 3 ... a position, eg. C for wheel centre
- 4 ... an index, eg. x for longitudinal direction or i for the tire index
- 5... an exponent or an additional assignment, eg. x^{\max} for the maximum value of x

Coordinate systems

- $\{\mathcal{O}_b, x_b, y_b, z_b\}$ origin and Cartesian coordinate axes of vehicle-fixed coordinate system
- $\{\mathcal{O}_i, x_i, y_i, z_i\}$ origin and Cartesian coordinate axes of i -th wheel-fixed horizontal coordinate system
- $\{\mathcal{O}_g, x_g, y_g, z_g\}$ origin and Cartesian coordinate axes of global coordinate system (inertial frame)

Variables, parameters and constants²

- $a_{1(2)}$ parameters of *TMsimple* tire model
- ${}_b a_{x(y)}$ acceleration in longitudinal (lateral) direction in vehicle-fixed coordinates

²SI units are used. Unless specifically noted otherwise, the unit rad was used for all angles.

$ba_{x(y)}^{\max}$	maximum value of $ba_{x(y)}$
$ba_{x(y)}^{\min}$	minimum value of $ba_{x(y)}$ (deceleration)
$\overline{\Delta a_y}$	mean relative deviation of ba_y
A_e	effective area for friction-locking mechanism in contact patch
A_p	projected frontal area of the vehicle
$A_{x(y)}$	longitudinal (lateral) parameter of <i>TMsimple</i> tire model
$b_{1(2)}$	parameters of <i>TMsimple</i> tire model
$B_{x(y)}$	longitudinal (lateral) parameter of <i>TMsimple</i> tire model
c	sensitivity parameter
Δc	variation of sensitivity parameter
$c_{1(2)}$	parameters of <i>TMsimple</i> tire model
$c_{ARB,j}$	stiffness of anti-roll bar (ARB) of j -th axle
c_D	air drag coefficient
c_L	light speed
$c_{S,i}$	spring stiffness of j -th axle
$c_{tot,j}$	total spring stiffness of j -th axle
$c_{T,x(y)}$	linear longitudinal (lateral) stiffness of the tire
$c_{T,z}$	linear vertical stiffness of the tire
C	wheel centre according to <i>ISO 8855</i> , [fSI11]
$\mathbf{d}(t)$	disturbance vector as a function of time t
d_M	measurement range of vehicle-fixed environmental sensor
d_W	warning distance between vehicle and obstacle
d_y	lateral tire damping coefficient
dY_0	initial stiffness of tire characteristics
f	index of vehicle's front axle
f_0	radar sensor frequency
\mathbf{f}_c	vector with partial derivatives of f_l to parameter c
fl	index of front left wheel
f_l	right-hand side of equation for \dot{y}_l
fr	index of front right wheel
$f_{r,i}$	rolling resistance coefficient of i -th tire
f_s	scaling factor for manoeuvre control
F	magnitude of combined tire contact forces

F	vector of combined tire contact force
F_A	aerodynamic force acting on vehicle
F_F	friction force acting in contact plane
F_F^{\max}	maximum friction force acting in contact plane
F_N	normal force acting on contact plane
$F_{z,nom}$	nominal value of the vertical tire load
F_R	tire's rolling resistance force
$F_{x(y)}^b$	basis value for longitudinal (lateral) tire forces
$F_{x(y),i}$	longitudinal (lateral) tire force on i -th tire in wheel-fixed coordinate system
${}_bF_{x(y),i}$	longitudinal (lateral) tire force on i -th tire in vehicle-fixed coordinate system
$F_{y,i}^D$	dynamic lateral tire force for i -th tire
$\overline{\Delta F_{y,i}}$	mean relative deviation of $F_{y,i}$ between reference simulation and parameter variation
$F_{W,x(y)}$	longitudinal (lateral) wind force acting on vehicle
$F_{z,i}$	tire load (normal force) on i -th tire
$F_{z,j}$	vertical axle load (normal force) on j -th axle
$\Delta F_{z,\phi,j}$	tire load variation due to ${}_b a_y$
g	gravitational acceleration
G	weight force of vehicle
G_s	weighting factor for combined tire forces
h	index of particles for particle filter
h_{CG}	height of vehicle's COG over road surface
$h_{IC,\phi}$	height of instantaneous centre of roll movement
$h_{IC,\theta}$	height of instantaneous centre of pitch movement
i	wheel index, $i = \{fl, fr, rl, rr\}$
I_i	moment of inertia of i -th wheel around y_i axis
I_z	moment of inertia of vehicle around z_b axis
IC_R	instantaneous centre of rotation
j	axle index, $j = \{f, r\}$
J	Jacobian matrix of vehicle state
k	discrete time step
k	vector of gyroscopic and centrifugal forces acting on vehicle
$k _{s_x=0}$	initial slip slope (at $s_x = 0$)
$K_{x(y)}$	longitudinal (lateral) parameter of <i>TMsimple</i> tire model

l	index for state variables
l_f	distance from vehicle's COG to front axle
l_r	distance from vehicle's COG to rear axle
l_{wb}	vehicle's wheel base
L	length of contact patch in longitudinal direction
m	index for sensitivity parameters
m_b	vehicle mass
m_w	wheel mass
M	mass and inertia matrix of vehicle
$M_{D,i}$	driving and braking torque of i -th wheel
M_{eng}	engine torque
$M_{R,i}$	rolling resistance torque of i -th wheel
n	number of elements in state variable vector \mathbf{z}
N	number of particles with index h
N_k	number of discrete time steps
o	number of elements in sensitivity parameter vector \mathbf{c}
p	sensitivity vector
p_B	braking pressure
p_l	sensitivity variable with index l
p_j	percentage of yaw moment supported by j -th axle
$p_{v,x}$	sensitivity of v_x with respect to μ^{\max}
$p_{v,y}$	sensitivity of v_y with respect to μ^{\max}
p_β	sensitivity of β with respect to μ^{\max}
q	vector of vehicle's applied forces
q_h	relative measurement likelihood function
r	index of vehicle's rear axle
r_0	unloaded tire radius
$r_{e,i}$	effective tire radius (e.g. dynamic tire radius) of i -th wheel
rl	index of rear left wheel
$r_{r,i}$	reference effective tire radius of i -th wheel
r_S	static tire radius
rr	index of rear right wheel
$r_{x(y),i}$	longitudinal (lateral) distance from \mathcal{O}_b to the i -th wheel centre C

r_α	lateral tire relaxation length
R^{\min}	turning circle of vehicle
\mathbf{s}	combined slip vector
$s_{x(y),i}$	longitudinal (lateral) slip in contact patch of i -th wheel
s_α	lateral slip (alternative definition for lateral tire dynamics, see Appendix B.2)
S	covariance matrix
t	time
Δt	time interval between two discrete time steps $k + 1$ and k
t_j	track width of j -th axle
T	measurement time (radar sensor)
\mathbf{T}_b^g	rotation matrix from vehicle-fixed to global coordinate system
\mathbf{T}_i^b	rotation matrix from i -th wheel-fixed to vehicle-fixed coordinate system
TTC	time-to-collision
u	exemplary variable
\mathbf{u}	control vector
U_e	effective rolling circumference of tire
\mathbf{v}	vehicle's velocity at COG
$\mathbf{v}_{C,i}$	translational velocity of i -th wheel centre C
$v_{C,x(y)}$	longitudinal (lateral) component of velocity of wheel centre C
\mathbf{v}_S	sliding velocity in contact patch
$v_{S,x(y)}$	longitudinal (lateral) component of sliding velocity in contact patch
v_x	vehicle's longitudinal velocity at COG
$v_{x,0}$	initial longitudinal velocity of vehicle at COG
$\bar{v}_{x(y)}$	vehicle's normalised longitudinal (lateral) velocity
v_x^{\max}	vehicle's maximum longitudinal velocity
Δv_x	relative velocity between vehicle and obstacle
$\Delta \bar{v}_x$	resolution of Δv_x measurement with radar sensor
v_y	vehicle's lateral velocity at COG
w	exemplary variable
w^{ref}	reference value from reference simulation
w^{var}	value from parameter variation
W	wheel contact point according to <i>ISO 8855</i> , [fSI11]

$\overline{\Delta w}$	mean relative deviation of w between reference simulation and parameter variation
$\mathbf{x}(k)$	state vector at discrete time step k
$\hat{\mathbf{x}}(k)$	estimate of state vector at discrete time step k
$x_{R,y}$	lateral relaxation length of tire
X	slip quantity (longitudinal or lateral)
${}_g\mathbf{Y}$	position vector of vehicle's COG in global coordinate system
y_e	lateral tire deflection
Y	tire force quantity (longitudinal or lateral)
$Y_{1(2)}$	parameters of <i>TMsimple</i> tire model
Y_{max}	peak value of tire characteristics
Y_∞	saturation value of tire characteristics
${}_b\mathbf{z}$	state vector of vehicle in vehicle-fixed coordinate system
Δz	vertical deflection of tire
$z_{b,i}$	body-fixed vertical coordinate in quarter vehicle model
z_i	vertical displacement of i -th wheel
z_l	state variable of vehicle with index l
$\Delta z_{S,i}$	spring deflection of i -th wheel
$z_{R,i}$	road-fixed vertical coordinate
α_i	lateral slip angle at i -th wheel contact point W^3
β	side slip angle in vehicle's COG
$\Delta\beta$	additional side slip angle at ${}_b a_y > 0$
$\Delta\beta^{\max}$	maximum value of $\Delta\beta$
$\overline{\Delta\beta}$	mean relative deviation of β
β_0	side slip angle at $ {}_b a_y \rightarrow 0$
β_0^{\max}	maximum value of β_0
β_r	slope of road profile
β_s	combined tire force angle
δ_i	wheel steering angle of i -th wheel
δ_S	steering wheel angle
$\overline{\Delta\delta_S}$	mean relative deviation of δ_S
$\Delta\phi_w$	phase shift between w^{ref} and w^{var}
ψ	yaw angle of vehicle in global coordinate system

³cf. Figure 2.2

μ	coefficient of friction between tire and road
$\hat{\mu}$	friction potential estimate
$\Delta\mu$	tolerable deviation of friction potential estimate
μ_0	nominal coefficient of friction in tire test bench measurements
μ^{\max}	friction potential (Maximum coefficient of friction between tire and road)
μ^{ref}	reference (real) value of the friction potential
μ_D	demanded coefficient of friction between tire and road
μ_G^{\max}	combined friction potential on vehicle level (global)
$\mu_{G,x(y)}^{\max}$	friction potential on vehicle level (global) in longitudinal (lateral) direction
$\mu_{L,x(y)}$	local coefficient of friction in longitudinal (lateral) direction
μ_S	safety margin (Difference between μ^{\max} and μ_D)
$\mu_{x(y)}$	coefficient of friction in longitudinal (lateral) direction between tire and road
σ_z	local normal stress in tire contact patch
τ	time function for lateral tire dynamics
τ_M	tolerable time delay of friction potential estimate
$\tau_{x(y)}$	local shear stress in contact patch in longitudinal (lateral) direction
$\tau_{x(y)}^{\max}$	maximum local shear stress in contact patch in longitudinal (lateral) direction
ω_i	rotational speed of i -th wheel
$\bar{\omega}_i$	normalised speed of i -th wheel
${}_b\omega_x$	vehicle body rotational speed around x_b axis
${}_b\omega_y$	vehicle body rotational speed around y_b axis
${}_b\omega_z$	vehicle body rotational speed around z_b axis
$\bar{\omega}_z$	normalised vehicle rotational speed around x_b axis
$\overline{\Delta\omega_z}$	mean relative deviation of ${}_b\omega_z$
ρ_a	air density

Contents

List of abbreviations	ix
List of symbols	xi
1. Introduction	1
1.1. Significance of friction potential for traffic safety	1
1.2. Traffic safety measures	3
1.3. Advanced driver assistance systems and vehicle dynamics controls	5
1.3.1. Significance of friction potential for ADAS and VDC	7
1.3.2. Requirements for an estimate of the friction potential for ADAS	9
1.3.3. Requirements for an estimate of the friction potential for VDC	14
1.4. Thesis contribution and outline	14
2. Estimation of the friction potential	17
2.1. Definition of the friction potential	17
2.1.1. Rubber physics	18
2.1.2. Friction potential of the rotating tire	19
2.1.3. Overview of relevant influencing factors	24
2.2. State of the art	29
2.2.1. Cause-based approaches	30
2.2.2. Effect-based approaches	31
2.2.3. Car-to-x communication systems (C2x)	35
2.2.4. Sensorfusion	36
2.3. Requirements for a friction potential estimation method	36
3. Vehicle model	39
3.1. Assessment of required model accuracy	39
3.1.1. Evaluation criteria	40
3.1.2. Investigated manoeuvres	42
3.1.3. Model parameters	44

3.1.4.	Results for double lane change manoeuvre	45
3.1.5.	Results for longitudinal manoeuvres	46
3.2.	Selected vehicle model	50
3.2.1.	Applied forces	53
3.2.2.	Vertical tire load variation	55
3.2.3.	Effective tire radius	58
3.2.4.	Steering model	59
3.3.	Tire model	59
3.3.1.	Combined tire forces	59
3.3.2.	Lateral tire dynamics	60
3.4.	Environment model	61
4.	Sensitivity Analysis	63
4.1.	Sensitivity analysis of ordinary differential equation systems	63
4.1.1.	Basic theory of direct sensitivity analysis	64
4.1.2.	Initial values of sensitivities	65
4.1.3.	Sensitivities of functions related to state variables	65
4.2.	Numerical implementation	66
4.3.	Sensitivity analysis using vehicle model	67
4.3.1.	Driving manoeuvres to cover parameter space	67
4.3.2.	Validity and limitations	68
4.4.	Normalisation of sensitivities	73
4.4.1.	Kinematic relation for normalisation	74
4.5.	Results and discussion of sensitivity analysis	76
4.5.1.	Resulting normalised sensitivities at different driving states	78
4.5.2.	Sensitivities for all-wheel-driven vehicle	84
4.5.3.	Sensitivities for front-braked vehicle (theoretical)	85
4.6.	Choice of sensitive parameters for the estimation observer	87
5.	Tire/road friction estimator	91
5.1.	Recursive Bayesian state estimation	91
5.1.1.	The recursive Bayesian state estimator	92
5.2.	Particle filtering	93
5.3.	Choice of observer model	96
5.3.1.	Overview on observer model	97
5.3.2.	Friction potential and longitudinal tire force	98

5.4. Observer structure	99
5.4.1. Measurement inputs	100
5.4.2. Model parameters	102
5.5. Considerations for the calculation of the longitudinal tire forces	103
5.5.1. Estimation of the longitudinal slip	104
5.5.2. Estimation of the slip angles	105
5.5.3. Wheel's torque	105
6. Results and conclusion	107
6.1. Strong acceleration manoeuvre with constant μ^{\max}	107
6.1.1. Results without resampling step	108
6.1.2. Results with resampling step	110
6.1.3. Resampling step with particle re-initialisation	111
6.2. Strong braking manoeuvre with varying μ^{\max}	113
6.3. Gentle braking manoeuvre on varying μ^{\max}	117
6.4. Braking manoeuvre on μ split conditions	119
6.5. Comparison of results with requirements of an AEB	122
6.6. Discussion and outlook	123
7. Summary	127
A. Friction potentials in literature	131
B. Tire model TMsimple and tire dynamics	133
B.1. Parameter relationships between static tire model	133
B.2. Modelling time function τ_y	134
C. Vehicle model structure for sensitivity analysis	137
C.1. Numerical implementation of vehicle model for automatic differentiation	138
C.1.1. Find maximum out of two values	139
C.1.2. Absolute value	139
D. Vehicle and tire model parameters	141
E. Longitudinal velocity estimation	145
E.1. Estimation of the longitudinal velocity using only ESC sensors	145
E.2. Observer-based estimation of the longitudinal velocity	146
E.3. Radar-based estimation of the longitudinal velocity	147

Contents

E.4. GNSS-based estimation of the longitudinal velocity	148
---	-----

Bibliography	150
---------------------	------------

1. Introduction

In the year 2000, more than 40,000 people died and 1.7 million people were injured in road traffic in the European Union. These numbers and the related societal consequences have led the European Commission to define its long term *zero-vision*, setting the goal of reducing all fatalities to a value close to zero by 2050, [Off01]. In 2009, the European Commission resolved to halve the number of fatalities by 2020 as an additional measure, [Off11]. To reach these ambitious goals, countermeasures are necessary that focus on the complex interactions between driver, vehicle and environment and also consider the different levels of traffic safety, see Sections 1.1 and 1.2. To develop countermeasures, traffic research is necessary.

1.1. Significance of friction potential for traffic safety

In the year 2011, approx. 9 % of all accidents involving personal injury in Germany were related to the road surface and lighting conditions, [Deu12]. Poor road conditions lead to a reduced maximum coefficient of friction between tire and road, which is referred to as friction potential. In most cases, road surface conditions themselves were not the main accident cause. Improper driving, e.g. exceeding speed limits or failing to observe the priority rules in traffic, and improper pedestrian behaviour were identified as the cause in 90 % of accidents. In combination with the aforementioned cases of reduced friction potential, these improper driving behaviours could often not be corrected in time and resulted in accidents. In comparison, technical or maintenance faults of vehicles were responsible for only 0.7 % of accidents according to the same statistical source, [Deu12].

When considering only severe accidents, the relative number of motorcycles and bicycles involved in accidents on slippery roads¹ is lower than the overall average, see Figure 1.1. In contrast, the percentage of involvement for pedestrians and drivers of mopeds is higher than average under these conditions. A possible explanation may be

¹Three road condition categories are used in [Deu12] that can be described as dry, slippery and very slippery (e.g. ice and snow). In this section, slippery refers to a surface with reduced friction due to rain or other impurities on the road, such as leaked oil, leaves or washed-up loam.

1 Introduction

that many pedestrians and moped drivers cannot postpone the planned journey because of the weather and are also limited in selecting alternative means of transport. 27 % of all accidents involving personal injuries and passenger cars occurred on slippery roads. Ice and/or snow was responsible in 4.8 % of all cases. When considering all slightly injured traffic participants, these numbers are slightly lower. An analysis of the traffic accidents in terms of the lighting conditions shows similar tendencies. There is no significant relationship between snowy/icy road condition and injury severity except for severe accidents involving material damage, see Figure 1.2. The percentage of people killed is slightly higher on slippery roads.

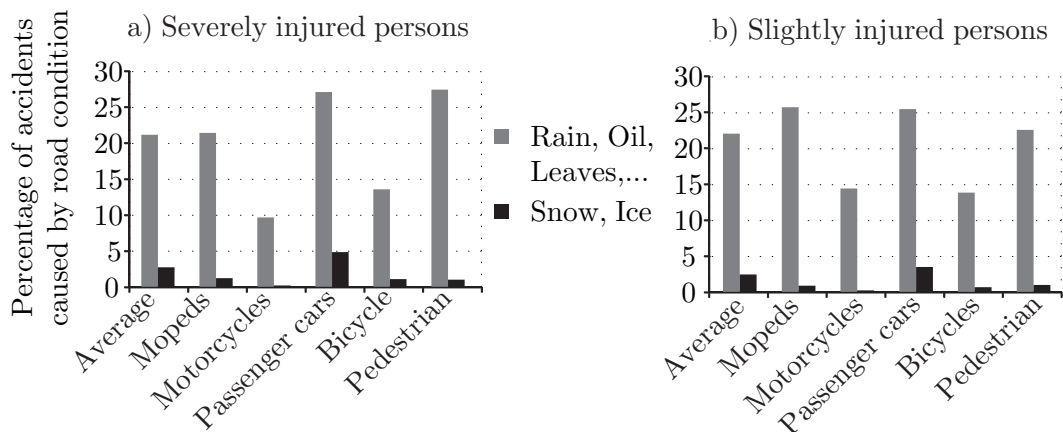


Figure 1.1.: Influence of road condition on accidents in relative numbers by selected categories of road users for a) severely injured people, and b) slightly injured people, based on *Destatis*, [Deu12]. Two of three road condition categories are shown; the remainder of the accidents occurred on dry roads.

The high number of passenger car accidents caused by bad road conditions is partly due to inadequate driver adaptation of the longitudinal speed under such road conditions. Studies show that drivers adapt the speed, but not enough to avoid collisions or unstable vehicle conditions when braking or cornering, e.g. [SS90], [Saa93] and [Roi93] as cited in [WWO97]. The drivers must use optical, acoustic and haptic cues to estimate the friction potential during driving since no direct measure is available. *Heinijoki* showed that non-expert drivers have difficulties gauging the current road conditions, especially for low friction potentials, [Hei94] as cited in [WA01].

These investigations highlight the importance of assisting the driver. A robust and reliable estimate of the friction potential is assumed to be one effective countermeasure

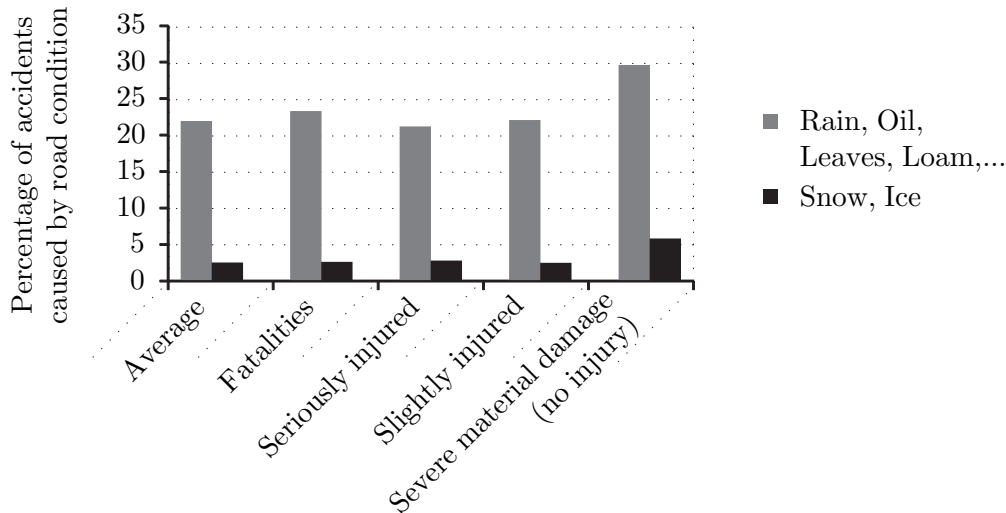


Figure 1.2.: Influence of road condition on injury severity and material damage in relative numbers, based on [Deu12]. Two of the three road condition categories are shown; the remainder of the accidents occurred under dry road conditions.

for reducing the number of accidents.

1.2. Traffic safety measures

One common classification of traffic safety measures distinguishes between primary, secondary and tertiary safety systems. Primary safety includes all safety systems that seek to prevent a collision or, if not possible, reduce the severity of the accident. In contrast, secondary safety includes all measures designed to reduce the injury severity for all road users involved when collision is imminent. Finally, tertiary safety refers to post-crash treatment, including measures such as first-aid education for all drivers, [Kra08, p.3]. Road traffic is determined by the complex interaction of three elements - driver, vehicle and environment. Knowledge of the friction potential can contribute on different levels of safety and road traffic elements, see Fig. 1.3.

In primary safety, all elements are affected by the friction potential. With training, non-expert drivers can learn to estimate the road condition and the stabilisation of the vehicle on slippery roads. Car-to-x communication systems (C2x), see Section 2.2.3, and road signs that adapt to road conditions are examples of ways in which traffic safety can be improved on the environmental level. Concerning the vehicle level, the information can be used to warn the driver when the friction potential is very low (e.g. under icy or

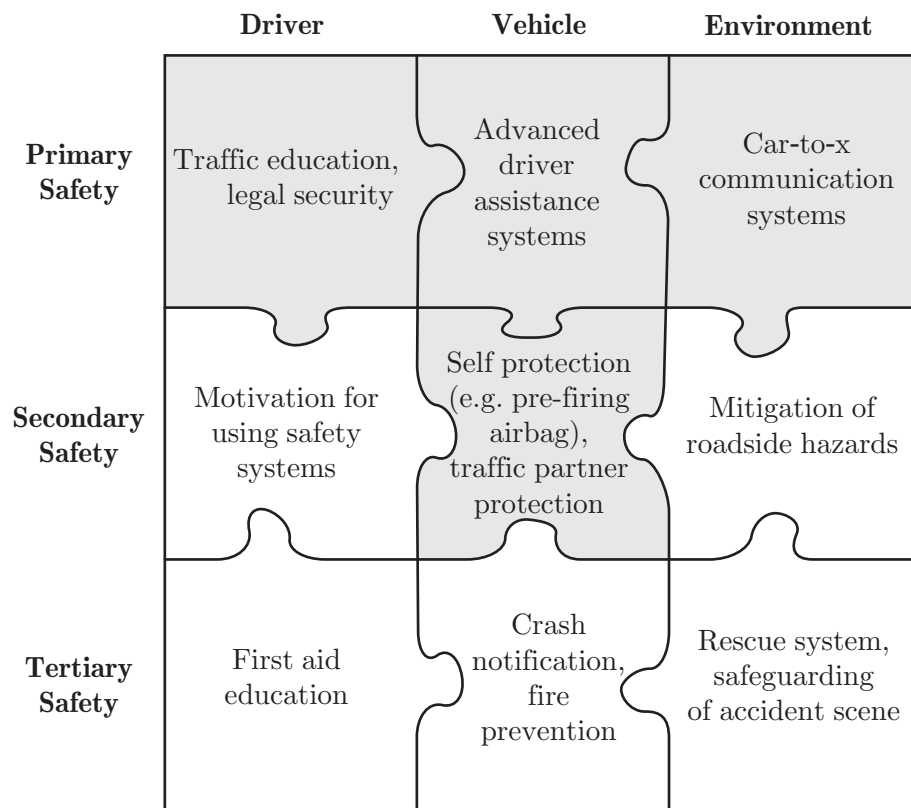


Figure 1.3.: Aspects of traffic safety and examples of safety measures, adapted from [Eic11, p.41] and [Kra08, p.3]. The knowledge of the friction potential can contribute to the areas highlighted in light gray.

snowy conditions). Also, a warning device can be activated when the safety margin between the current driving state and the physically achievable maximum has fallen below a safety threshold, [Hol92, p.65-66]. The friction potential can also be used to improve specific advanced driver assistance systems (ADAS) or vehicle dynamics controls (VDC). In secondary safety, only the vehicle level can be adapted, e.g. with airbag pre-firing. In case of imminent collision, the airbags can be pre-fired before the collision takes place in order to reduce the head injury risk for the occupants, [Eic11, p.162-163]. The friction potential must be known in order to detect an imminent collision accurately and to predict the possible trajectories between time of detection and the detected collision, see Section 1.3.

The accuracy requirements for estimating the friction potential are presumably low for

driver warning. The acceptable accuracy of any estimate to be used for driver warning depends on the type and urgency of the specific warning, [HG09]. For warnings that require the driver to perform an action, the tolerance for a false intervention is very low. This means, for example, that when a collision is imminent and the driver has to react in order to avoid or mitigate the collision, the detection of the collision and the influencing parameters have to be highly accurate. A decrease in the friction potential requires the driver to be more attentive. In this case, false interventions are more tolerable and hence the accuracy requirement is lower. A rough but reliable resolution of three different friction potentials (high, slippery, very low) is already valuable to improve traffic safety. Further investigation on the accuracy requirements for an estimate of the friction potential that is used to adapt interventions on the vehicle level is shown in the following section.

1.3. Advanced driver assistance systems and vehicle dynamics controls

The driving process consists of a complex interaction between driver, vehicle and environment, see Figure 1.4. This interaction has to be considered in the intervention strategies of ADAS and VDC. However, the intervention characteristics of ADAS and VDC are very different, and hence the requirements also differ greatly.

According to *Donges*, the tasks of the driver consist of navigation, course planning and stabilisation, [Don09]. In the navigation task, the driving route is chosen in order to fulfill the purpose of the planned travel. Course planning is necessary in both longitudinal and lateral direction and depend on the traffic conditions and the drivers' preferences. Subtasks include selecting the longitudinal speed, distance to other traffic participants and the vehicle's position in the lane. In the stabilisation task, the driver performs actions in order to adapt the actual vehicle reaction to the desired one. Stabilisation tasks typically lie in the time range of 0.5 to 2 seconds ahead, whereas the navigation task can begin up to several hours in advance and course planning starts when the driver is able to perceive the environment which is in the range of one minute. Typical anticipatory times for steering actions are within 1 second, whereby these times are normally higher for longitudinal manoeuvres, [Don09]. Drivers receive between 80 and 90 % of the driving-relevant information through visual cues, [AB09]. The lack of visual cues also explains the higher risk for accidents at night, [KH09].

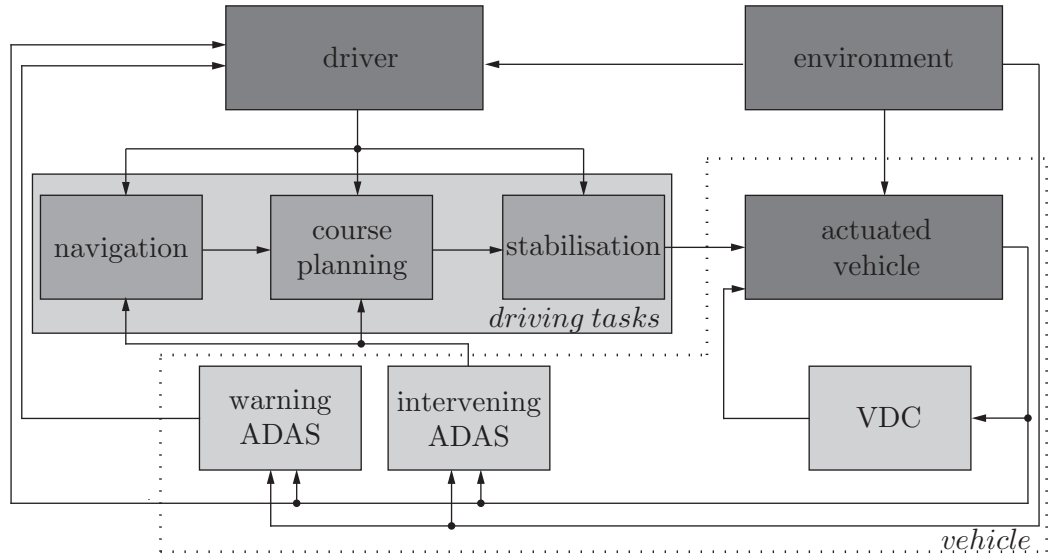


Figure 1.4.: Simplified representation of driving process including the elements driver, vehicle and environment based on *Niederkofter*, [Nie11, p.106]. Warning ADAS target the driver directly. Driver and intervening ADAS both undertake driving tasks, requiring human machine interaction. VDC directly actuate the vehicle on the stabilisation level, but do not necessarily require interaction with the driver. Thus, the connection to this driving task is not shown in this depiction.

In this work, the term VDC denotes all safety systems on the vehicle level that act on the stabilisation level without a direct feedback loop including the driver. Therefore, Figure 1.4 shows VDC as an internal closed loop of the vehicle. Controller outputs for the actuators are calculated using vehicle dynamics state variables, in order to minimize the difference between the nominal and actual values, [Ras09]. Many sources classify VDC as a subgroup of ADAS, e.g. [WHW09a]. In the present thesis, ADAS denotes all systems working on the navigation, course planning and stabilisation level, that directly include the driver in a feedback loop. A strict differentiation in VDC and ADAS on the stabilisation level is difficult. In general, ADAS can be divided into warning and intervening systems. Here, it is assumed that ADAS include only warning systems on the stabilisation level, whereas VDC include all intervening systems. This classification is chosen to emphasise the different requirements on control variables within VDC and ADAS which are discussed in Sections 1.3.2 and 1.3.3. For example, the requirements for the estimates to be used within VDC are very high due to the time characteristics and the safety-critical nature of VDC.

Warning ADAS notify the driver, but do not directly influence the motion of the vehicle like intervening ADAS do. Especially on the course planning level, information about the environment (e.g. other traffic participants, road geometry) is required to identify possible critical situations in advance. This leaves more time for a plausibility check of estimates, if these are subject to control inputs for ADAS. Nevertheless, the requirements for an estimate of the friction potential μ^{\max} depend on the specific application at the vehicle level. In the following section, the potential ADAS and VDC that could be improved by adapting their strategies to the current friction potential are identified first, see Section 1.3.1. The next sections then discuss the specific requirements for an online estimate of the friction potential to be applied in specific ADAS, see Section 1.3.2, and in specific VDC, see Section 1.3.3. The requirements cover the tolerable time delay τ_M before a robust estimate is available and the tolerable deviation $\Delta\mu$. The tolerable time delay is a theoretical value and considers the computational time of the friction potential in general, but also for changing states of either the road condition or the vehicle's state (e.g. from free rolling to accelerating). The relation between an estimate $\hat{\mu}$ and an ideal value μ^{ref} is given by

$$\hat{\mu} = \mu^{\text{ref}} \pm \Delta\mu. \quad (1.1)$$

1.3.1. Significance of friction potential for ADAS and VDC

Eichberger, Tomasch et al. evaluated the potential benefit of specific ADAS and VDC for preventing or mitigating accidents in their RCS-TUG Study, [ETR⁺10]. They performed a case-by-case analysis within database for 514 incidents of all 848 accidents in Austria in 2003 in which people died. The basis of this investigation was ZEDATU², a central database in Austria for in-depth analysis of road accidents with a focus on fatal car accidents, [TS06]. Experts reconstructed the collision phase using the commercial software PC Crash, [SM01]. With the data from the collision phase, numerical reconstruction of the pre-collision phase was possible. Altogether, the effect of 43 warning and intervening systems on the simulated real life scenarios were investigated. The benefit of each system was determined using both the number of accidents prevented and the cases where fatalities were avoided with a high probability, see *Eichberger* for a detailed explanation, [ETR⁺10, p.83-97].

Figure 1.5 shows the top ten systems identified in *Eichberger et al.* for avoiding or

²Abbreviation in German for **Z**entrale **D**atenbank zur **T**iefenanalyse von **V**erkehrsunfällen

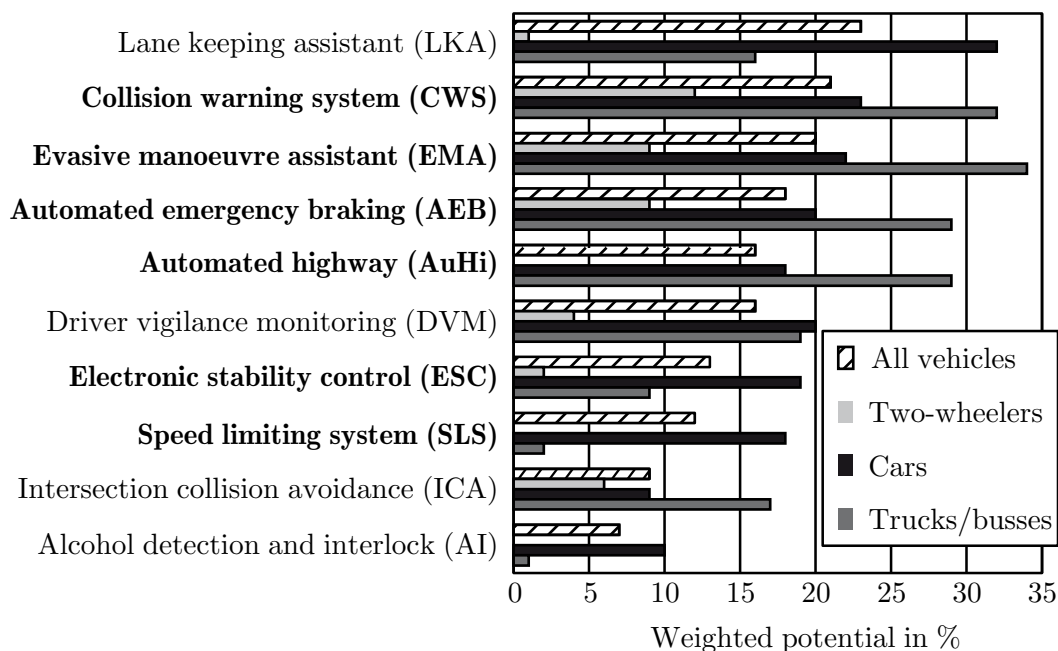


Figure 1.5.: Potential benefit for avoiding fatalities for different road user groups for top ten systems identified by *Eichberger et al.* in TUG-RCS study, [ETR⁺10]

mitigating accidents, [ETR⁺10]. Lane keeping assistant (LKS), automated highway systems (AuHi)³ and speed limiting systems (SLS) that assist the driver in normal driving states show a high benefit for traffic safety. Also, forward collision avoidance and mitigation systems such as collision warning system (CWS), evasive manoeuvre assistant (EMA), automated emergency braking system (AEB) and intersection collision avoidance systems (ICA) have a high potential. Since VDC includes electronic stability control (ESC), one VDC is also in the top ten. Finally, driver-condition-related systems such as driver vigilance monitoring (DVM) and alcohol detection and interlock systems (AI) are among the top ten systems in this study. For a vehicle equipped with all top ten systems, the potential benefit for preventing accidents is 59.2 % and of preventing fatalities is 14.3 %, see Figure 1.6. These potential benefits can only be attained under the assumption that drivers do not compensate for the ADAS support by taking higher risks.

The systems that could be improved by adapting to the friction potential are indicated in bold print in Figure 1.5. This investigation provided the basis for the selection of sys-

³Here, *AuHi* comprise systems for autonomous driving on highways, i.e. longitudinal and lateral vehicle guidance, cf. [ETR⁺10, p.102]

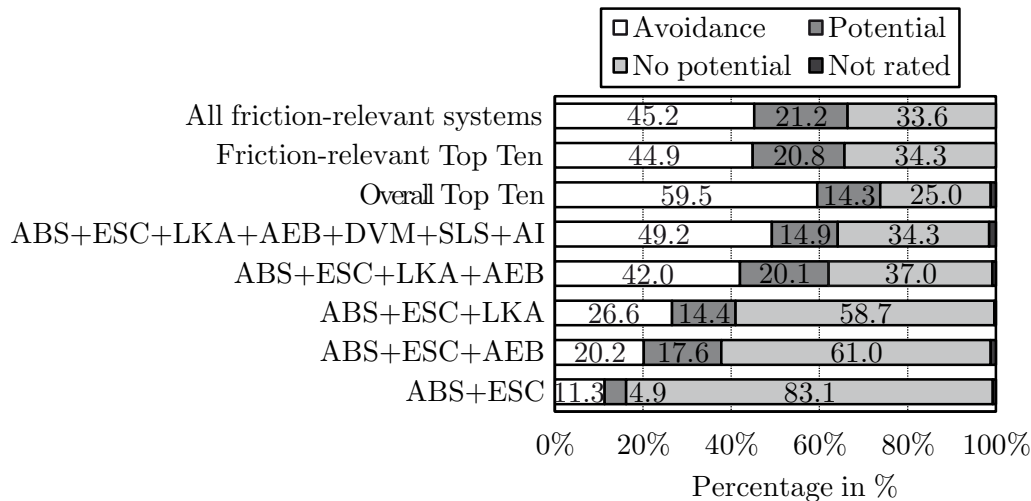


Figure 1.6.: Potential benefit of friction-relevant systems of TUG-RCS study for avoiding fatalities in all investigated cases and vehicle types according to *Lex et al.*, [LE11]

tems described in Sections 1.3.2 and 1.3.3. *Lex and Eichberger* repeated the investigation of the potential benefit to traffic safety for those systems that could be improved by the friction potential, [LE11]. The results show that a vehicle equipped with all friction relevant safety systems could avoid 45.2 % of all accidents and 21.2 % of the fatalities, see Figure 1.6. A vehicle equipped with only the top ten friction-relevant systems could still avoid 44.9 % of the accidents and 20.8 % of the fatalities. Comparing the benefit of 44.9 % to the 59.2 % for all top ten systems indicates that the friction potential influences many of the systems that are relevant for enhancing traffic safety. Although not directly proven, the additional benefit of adapting warning and intervention strategies of the friction-relevant systems to the friction potential is assumed to be quite high, see Sections 1.3.2 and 1.3.3.

1.3.2. Requirements for an estimate of the friction potential for ADAS

Although activation strategies vary considerably, the strategy often includes some of the four phases presented below, see also Figure 1.7. In the *prediction phase*, ADAS detect oncoming collisions that are imminent if the driver does not react. Model-based approaches are used to predict possible collisions with a high probability. The number of missed interventions must be kept low in order to maintain the driver's acceptance of the system, but false interventions must be prevented. When no collision is imminent,

1 Introduction

but one is detected anyway and the system intervenes, this false intervention can result in severe accidents. For this reason, all subsequent phases are activated as late as possible, which leads to the so-called warning dilemma: with the validation time obtained, the probability of the predicted collision parameters in the pre-collision phase can be increased. But on the other hand, the driver warning is more effective the sooner it is initiated, [HG09].

Two factors are crucial for predicting a collision and therefore the activation times for the different phases, [Eic11, p.120-127]. These two factors describe the possible courses of the traffic participants involved in the pre-collision phase which are necessary to predict the collision parameters. The first factor is the drivers' reaction, e.g. whether there is operation of steering wheel, brakes or throttle and, in case of an operation, how strong the driver's input is. The second factor is the friction potential that limits the maximum transmittable horizontal tire forces and therefore the possible motion of the vehicles in the horizontal plane. Depending on the warning strategy, the driver is being alerted to be either attentive or to set an action in the *warning phase* by acoustic, haptic or visual signals. The transition between warning and intervention is herein referred to as *decision phase*, as the course of action is chosen. Depending on the probability of the predicted collision, an intervention has to be omitted (e.g. when the collision probability is low) or activated. Some systems also allow for different intervention strategies, such as braking or steering around an obstacle as shown in Figure 1.7. Whether it is optimal to brake or to steer in order to avoid a collision depends strongly on the friction potential. In addition, a system must take into account both the relative velocity and the possibility of steering around an object, which depends on the road type and other traffic participants. Finally, the *intervention phase* starts, provided that the driver has still not reacted. This phase can consist of several stages, see e.g. for an AEB in Section 1.3.2.

Current systems are developed to fulfill the requirements of collision mitigation and avoidance on dry roads. However, many ADAS show their highest potential for avoiding accidents or reducing the injury severity on low-friction surfaces. Thus, investigations have proven that the activation times of an EMA can be significantly increased on low-friction surfaces when the friction potential is known because interventions can be started earlier, [NLER11] and [LRNE13]. A combined consideration of driver behaviour and vehicle dynamics results in the following thresholds for activation times, [Win09a]. When an imminent collision is detected, the theoretical time until the obstacle is reached,

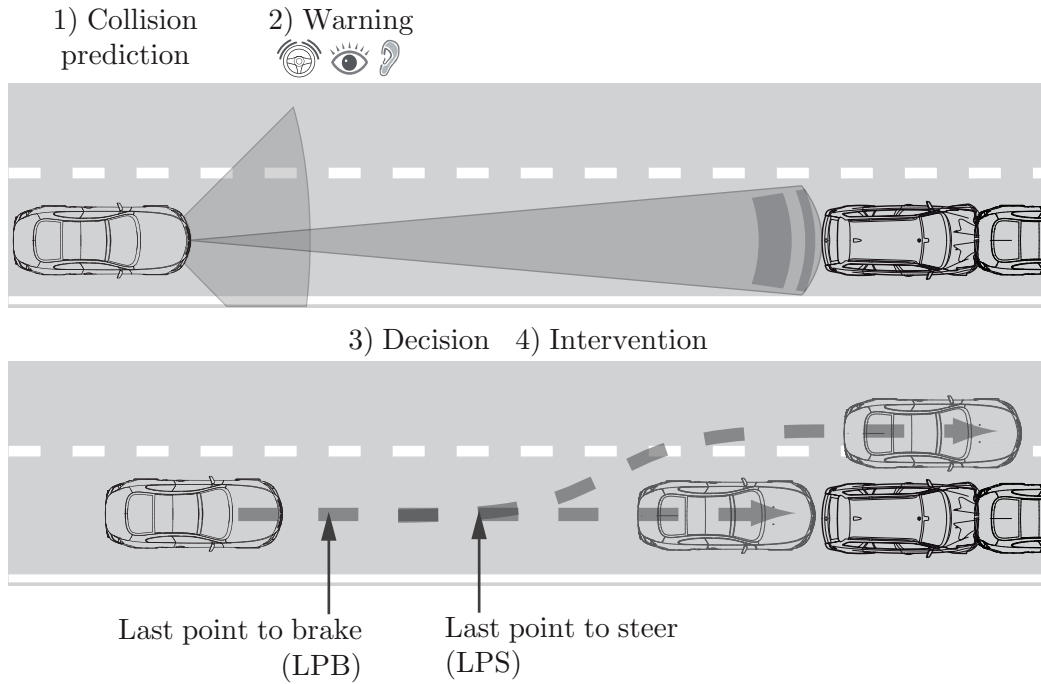


Figure 1.7.: Activation strategy for ADAS shown for a combined evasive and emergency braking assistant consisting of the four phases of *collision detection*, *warning*, *decision* and *intervention*, based on [Nie11, p.110] and [Har11]

known as the time-to-collision (TTC), is given for steady state motion by

$$TTC = \frac{d_W}{\Delta v_x}, \quad (1.2)$$

with the warning distance d_W to the obstacle and the relative velocity Δv_x between vehicle and obstacle, [Eic11, p.127]. In frontal collisions on dry roads, initiating an evasive manoeuvre at TTC 0.6 s is not enough to avoid a collision due to the physical limits. The driver's limit for an intervention is already at a TTC of about 1 s, but this situation is perceived as very risky by non-expert drivers and thus only of theoretical importance. A non-hazardous situation is perceived with a TTC greater than 1.6 s. Depending on the actual friction potential μ , these activation times for braking manoeuvres have to be increased by $\frac{1}{\mu}$, according to Winner, [Win09a]. For $\mu = 0.2$, the activation times have to be 5 times higher than for dry roads of about $\mu = 1$. For an evasive manoeuvre, the activation times have to be adapted by $\frac{1}{\sqrt{\mu}}$, according to Winner, [Win09a]. The following section discusses the requirements for estimating the friction potential for theoretical

1 Introduction

application in an AEB. This system has been proven to have high potential benefit for avoiding and mitigating accidents, see Section 1.3.1. In addition, the requirements for pre-firing airbags are shown as an example for tertiary safety systems.

Requirements for automated emergency braking systems

Investigations have shown that many rear-end crashes happen because drivers do not brake hard enough, react too late or fail to react, [Bre09]. Braking assist systems (BA) assist drivers who do not brake hard enough by increasing the braking pressure when the braking pedal is actuated with a high velocity. In contrast, AEB systems come into play when drivers react too late or fail to react. The AEB intervention phase consists of two stages. In the first stage, a partial braking manoeuvre is initiated. The vehicle speed is reduced while drivers are still offered the chance to provide their own intervention. If the driver fails to react, a full braking manoeuvre is initiated in the second stage.

The required accuracy depends on the relative velocity between the vehicles, the road condition and the braking system conditions. When the activation times of an AEB are adapted by an underestimated friction potential, the calculated braking distance is longer than the actual value and the intervention is started earlier. The collision is avoided, but valuable activation time is lost for collision validation, and driver acceptance of the system may therefore decrease. When the friction potential is overestimated, the collision cannot be avoided which results in an impact. *Lex et al.* determined that an impact speed of 4.2 m/s is tolerable in terms of pedestrian safety and vehicle repairability, [LKE13a]. Figure 1.8 shows the requirements for an estimate of the friction potential to be applied in an AEB when approaching a standstill object. The collision model uses Newton's equation of motion for a single mass point with one single degree of freedom in the longitudinal direction. Such simple models are often used in published AEB warning algorithms, [Eic11, p.120].

Section 6.5 discusses the estimation algorithm for the friction potential developed in this thesis in the context of requirements for an AEB that are described here. For this algorithm, another representation of these requirements is used, which shows the tolerable deviation $\Delta\mu$ versus the real value μ^{ref} ; see Figure 6.16.

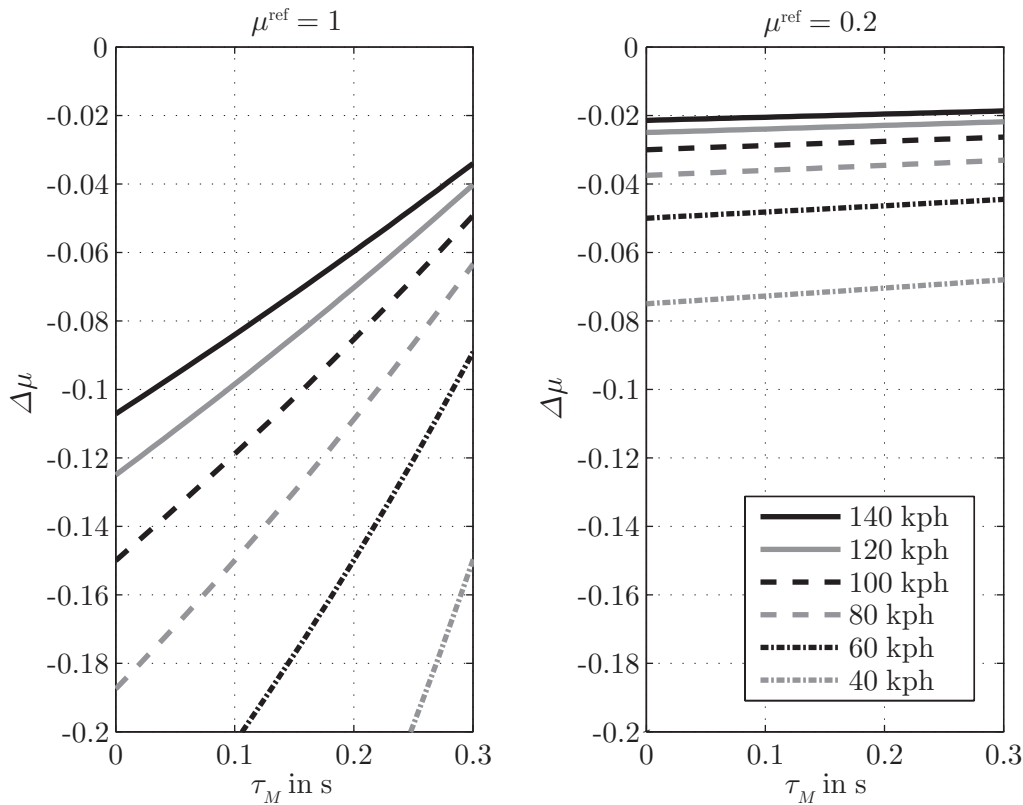


Figure 1.8.: Tolerable deviation $\Delta\mu$ versus tolerable time delay τ_M of the friction potential estimate when applied in an AEB to keep the impact speed below 4.2 m/s when approaching a standstill object and assuming hard braking (near physical limits), based on *Lex et al.*, [LKE13a]. These requirements depend on the initial velocity and the actual value μ^{ref} of the friction potential, shown here for $\mu^{\text{ref}} = 1$ (left) and $\mu^{\text{ref}} = 0.2$ (right).

Requirements for pre-firing airbag

With this system, the airbag is deployed before the collision occurs. This allows less aggressive deployment and couples the occupants' heads to the decelerating vehicle already in the pre-collision phase. These measures can decrease the probability of head injuries, according to *Eichberger*, [Eic11, p.162-163]. Nevertheless, it has to be assured that the predicted collision is imminent in order to avoid false firing. Also, the two parameters stopping distance and impact speed must be calculated accurately in order to derive the necessary pre-fire times. Without information on the friction potential and the driver input, these two parameters cannot be predicted accurately and the pre-fire time cannot be calculated. For a friction potential of 0.8, the theoretically required accuracy of

1 Introduction

the velocity prediction for a suggested pre-fire time of 80 ms is $\pm 0.94 \text{ m/s}^2$, according to *Eichberger*, [Eic11, p.115-120]. As the pre-collision scenario is the same for airbag pre-firing and AEB, the requirements for the accuracy $\Delta\mu$ and time delay τ_M for an estimate of the friction potential are the same as in Figure 1.8.

1.3.3. Requirements for an estimate of the friction potential for VDC

The requirements for an estimate of the friction potential to be applied in the systems ABS, ESC and active front steering (AFS) were thoroughly investigated and presented in the work of *Weber*, [Web04]. Straight braking, lane change and curve braking manoeuvres were evaluated on even road surface. It was assumed that the mounted tires and the corresponding tire model parameters were known (not including the current road condition). Table 1.1 shows the requirements determined by *Weber*, [Web05]. This in-

Table 1.1.: Requirements on friction potential estimate for different manoeuvres concerning tolerable deviation $\Delta\mu$ and maximum time delay τ_M , according to *Weber*, [Web05].

Manoeuvre	Tolerable Deviation $\Delta\mu$	Tolerable Time Delay τ_M
Full braking straight	-0.03 - 0.08	26 ms
Lane change	-0.08 - 0.03	-
Full braking in a curve	-0.02 - 0.02	10 ms

vestigation also showed that the highest benefit of an adaptation to the friction potential was achieved at high longitudinal speeds and low friction potentials.

1.4. Thesis contribution and outline

The functionality of today's vehicles is limited because the current friction potential between road and tires during driving is not known. With increasing automation of driving tasks, information on the current friction potential gets more important. The aim of this thesis is to present an algorithm to estimate the friction potential between tire and road. Within this work, only vehicle-based solutions are considered (e.g. no C2x systems), and, among these, only those methods that consider measurements of the vehicle's dynamic reaction (e.g. no optical sensors). Although application for other vehicle types is not excluded, the focus is the applicability for passenger cars. An automated emergency braking system (AEB) is chosen as an application case for the developed algorithm.

In particular, the aim of this thesis is to answer the following research questions:

- Which state variables are sensitive to the friction potential in different driving states?
- Based on the identified set of sensitive variables, is it possible to develop an estimation algorithm for the friction potential to meet the accuracy and time delay requirements for adapting the intervention strategies of an AEB (as an exemplary ADAS)?

In order to answer these research questions, the present thesis is structured as follows:

Chapter 1 provides an overview on the significance of the friction potential for traffic safety and discusses the adaptation of ADAS and VDC activation strategies to the current road conditions. Finally, AEB systems are selected as a test case, and the requirements concerning the tolerable deviation of an estimate of the friction potential to be used within this system are presented.

Chapter 2 begins with a definition of the friction potential and then discusses the relevant mechanisms, including rubber physics and the tire/road contact. An overview on the state of the art on friction estimation is also provided.

Chapter 3 shows the derivation of the necessary complexity of the vehicle and tire model to describe the tire/road contact. These models are then described in detail, as they are used for the sensitivity analysis in Chapter 4 and parts of the models are also used within the observer in Chapter 5.

Chapter 4 presents the sensitivity analysis used to answer the first research question. After a description of the method used, the results are presented which answer the question about which variables are affected the most by the friction potential. This part of the thesis contributes to the systematic understanding of the influence of the friction potential on a vehicle's dynamics states. Thus, variables are identified that are potentially suitable for use in identifying the friction potential in an observer model.

Chapter 5 describes a non-linear observer which is used to estimate the friction potential based on the sensor signals of an ESC-equipped vehicle. After a short description of particle filtering, the relevant observer model is presented, which was developed based

1 Introduction

on the results from the sensitivity analysis in Chapter 4. This part of the thesis contributes a novel method for estimating the friction potential using almost exclusively ESC sensors.

Chapter 6 then compares the results of friction estimation using the non-linear observer proposed in Chapter 5 with real vehicle measurements. The conditions investigated include high and low-friction surfaces, driving and braking conditions and different longitudinal accelerations, as well as μ *split* and μ *step* conditions. Different strategies for re-initialising the particles used in the particle filter after convergence are also discussed.

Finally, **Chapter 7** provides an overview of the main findings and a summary of the sections in this thesis.

2. Estimation of the friction potential

The first part of this chapter describes the physical effects in the contact patch between tire and road that mainly influence the friction-based force transmission and the friction potential. The friction potential is described on different levels of scale (e.g. in the contact patch or globally for the vehicle) and factors that influence the friction potential are discussed. The second part of this chapter presents the state of the art for estimating the road condition. This includes a short overview of cause-based and effect-based methods, as well as infrastructural systems and sensorfusion. Finally, the requirements for an estimation algorithm are presented.

2.1. Definition of the friction potential

The force transmission between tire and road depends on the frictional behaviour in the contact patch. The coefficient of friction between rubber and asphalt results from complex mechanisms, which themselves depend on several parameters and variables. Most of these influences show non-linear behaviour on the coefficient of friction, [WHW02]. The relation with the two main influences, namely the normal force and the sliding velocity, are described within this section. The coefficient of friction μ can be used to characterise the grip when it is treated as a direction-dependent variable with different values for μ for the longitudinal and lateral direction. Generally, the coefficient of friction μ is defined as

$$\mu = \frac{F_F}{F_N} \quad (2.1)$$

with the friction force F_F acting in the contact plane and the normal force F_N acting on the contact plane, [Bac96, p.8]. The maximum achievable coefficients of friction μ^{\max} between tire and road limit the maximum transferable horizontal tire forces. In this work, μ^{\max} is referred to as friction potential. Introducing F_F^{\max} as the maximum transferable force in the contact plane, the friction potential reads

$$\mu^{\max} = \frac{F_F^{\max}}{F_N}. \quad (2.2)$$

2 Estimation of the friction potential

Concerning tire rubber physics, the conditions of both rolling and sliding of the tire contact patch on the road surface have to be taken into account simultaneously. The friction effects for pure sliding of rubber provide a basis for understanding the complex friction characteristics, see Section 2.1.2. For a rolling tire, geometric and kinematic effects also have to be considered, see Section 2.1.2.

2.1.1. Rubber physics

Rubber friction, which depends on the internal friction in the rubber material, shows viscous and elastic behaviour, [Pop09]. Pure elastic behaviour is described by Hooke's Law, which gives a linear relation between stress and strain. Ideal elastic materials accumulate deformation energy and deliver it completely when unloaded, while ideal viscous materials transform all deformation energy into thermal energy. For materials with ideal viscous behaviour, the complex shear modulus for Newtonian fluids describes the relation between shear stress and shear velocity. For visco-elastic materials such as rubber, the deformation energy is partially stored and partially dissipated, [Bac96, p.13]. Effects such as the temperature dependence on rubber friction as well as its dependence of the velocity in the contact surface correlate with the complex shear modulus, [Pop09].

Friction components of sliding rubber

The friction force for sliding rubber is composed of the force components caused by adhesion, hysteresis, viscosity and cohesion; as summarized in *Bachmann*, [Bac96, p.16-24]. All components do not necessarily have to be present at the same time.

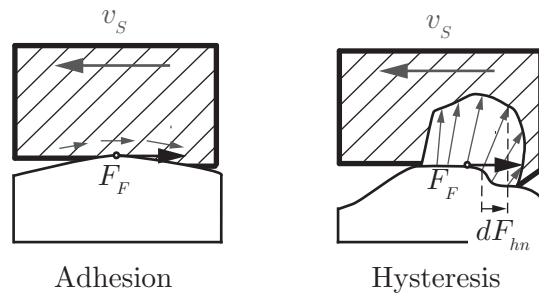


Figure 2.1.: Main friction mechanisms *adhesion* (left) and *hysteresis* (right) based on *Schramm* with the resulting friction force F_F , which is pointed in the opposite direction of the sliding velocity v_S , and the element dF_{hn} of the hysteresis force projected to the plane of motion, [SHB10].

On a smooth, even, dry road, the *adhesion component* has the main influence on the friction force, see Figure 2.1 (left). It is caused by molecular bonds between the friction partners and strongly depends on intermediary layers such as water or snow, [Bac98, p.4]. The pressure distribution of rubber material sliding over irregularities caused by the roughness of the road is symmetrical for low sliding speeds v_S . With higher sliding speeds, the relaxation of the rubber is not fast enough due to internal damping. Small areas lift from the road surface, which results in an uneven pressure distribution, see Figure 2.1, right. The component of the internal friction force F_F projected to the plane of motion, which is called the *hysteresis component* (see example of element dF_{hn} in Figure 2.1), superposes the friction force in the contact surface. In addition to the sliding speed, it also depends on the geometry of the road and the visco-elastic properties of the rubber. Unlike adhesion, this component is insensitive to the presence of intermediary layers, [Bac96, p.22]. The last two components only occur under certain circumstances. *Viscosity components*, which are only relevant when thick intermediary liquid layers are present, occur due to shear effects. *Cohesion forces* appear in cases of abrasion and tire wear. The surface of the rubber material increases, leading to friction loss, [Bac96, p.4].

2.1.2. Friction potential of the rotating tire

Friction-based force transmission requires a relative motion, or the tendency to motion, between the friction partners. In the case of tire road friction, the relevant relative motion is the sliding velocity v_S in the contact patch. In the longitudinal direction, it is given by $\omega \cdot r_e - v_{W,x}$ with the effective tire radius r_e , the wheel's rotational speed ω and the longitudinal velocity component $v_{W,x}$ in the contact patch. One frequently used value of the longitudinal sliding speed is described by the longitudinal slip s_x and reads

$$s_x = \begin{cases} \frac{\omega \cdot r_e - v_{W,x}}{|v_{W,x}|} & v_{W,x} > r_e \cdot \omega \\ \frac{\omega \cdot r_e - v_{W,x}}{|\omega| \cdot r_e} & v_{W,x} < r_e \cdot \omega \\ 0 & v_{W,x} = r_e \cdot \omega. \end{cases} \quad (2.3)$$

In the lateral direction, the relevant sliding velocity is given by the lateral slip angle

$$\alpha = \arctan \left(\frac{v_{W,y}}{v_{W,x}} \right) \quad (2.4)$$

which also includes the lateral component $v_{W,y}$ of the velocity in the contact patch. Figure 2.2 shows a graphical explanation of r_e , ω , $v_{W,x}$ and $v_{W,y}$ and the velocity v_C in the wheel centre C .

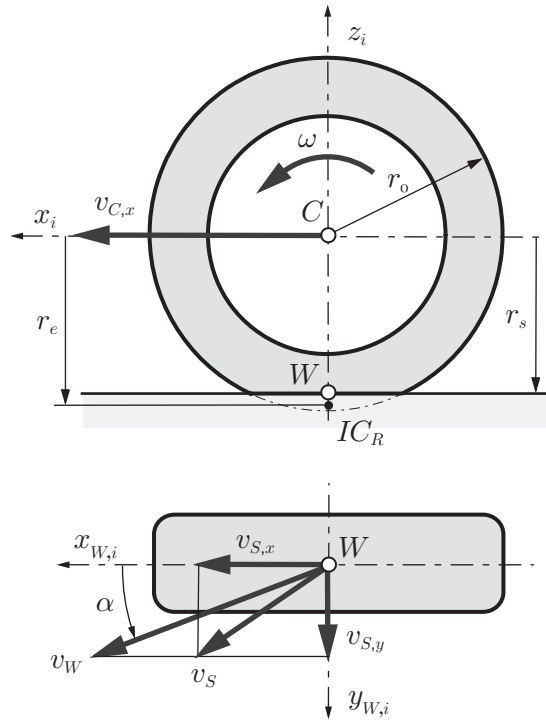


Figure 2.2.: Kinematic wheel quantities of the i -th wheel coordinate system $\{\mathcal{O}_i, x_i, y_i, z_i\}$ with its origin in the wheel centre C according to *ISO 8855*, [fSI11]; the graphic depiction is based on *Hirschberg*, [HW12, p.16]. The velocity in the contact point W between tire and road is described by its components $v_{W,x}$ and $v_{W,y}$. The components $v_{S,x}$ and $v_{S,y}$ of the sliding velocity v_S differ from v_W by $\omega \cdot r_e$. The effective tire radius r_e is the distance between the wheel centre C and the instantaneous centre of rotation IC_R . In addition, the unloaded tire radius r_0 , the static tire radius r_s , the wheel speed ω and the lateral slip angle α are shown.

As shown in Equation 2.3, for forward driving the conditions braking ($-1 < s_x < 0$) and accelerating ($0 < s_x < 1$) have to be distinguished for a slipping tire. As previously mentioned, slip is necessary to transfer friction forces. Longitudinal slip can be divided into two effects: slip created by sliding of the rubber on the road surface and slip that occurs due to the deformation of the tire profile elements when entering the contact patch. For small slip values, deformation slip dominates, whereas with increasing slip, sliding slip outweighs deformation slip. At pure rolling ($s_x \approx 0$), deformation slip is present when tire profile elements enter or exit the contact patch, see next section. For pure sliding ($s_x \sim \pm 1$), the effects discussed in Section 2.1.1 dominate. In this condition, the

sliding speed is the same for the whole contact patch.

Typical longitudinal and lateral characteristics of the coefficient of friction μ between tire and road are shown in Figure 2.3. For small slip variables s_x and α , μ increases linearly. With increasing slip, μ increases degressively up to the maximum μ^{\max} which is defined in Equation 2.2, until it slightly decreases and reaches saturation. In non-critical driving states, vehicles travel in the lower slip regions of Figure 2.3. The difference between the instantaneous or demanded coefficient of friction μ_D in the current driving states and the available μ^{\max} can be defined as the safety margin μ_S .

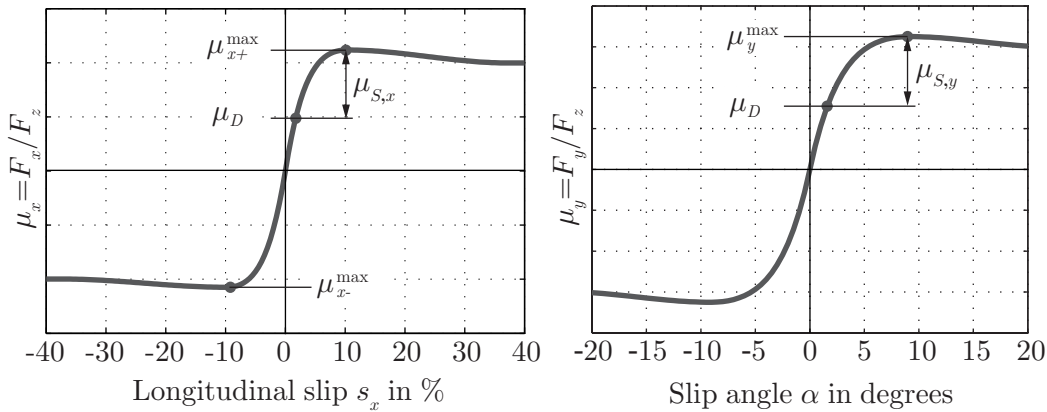


Figure 2.3.: Characteristics of utilised longitudinal and lateral coefficients of friction μ_x (**left**) and μ_y (**right**) for a constant normal force, longitudinal velocity $v_{C,x}$, temperature and inflation pressure. The difference between a currently demanded μ_D and the friction potential μ^{\max} is the safety margin μ_S .

Superposition of shear stresses and rolling resistance

The values of the friction potentials for braking and accelerating may differ. In standstill, the tire's toroid form is flattened under a load, introducing shear stresses in the contact patch. They superpose the longitudinal shear stresses caused by acceleration and braking forces in the contact patch, see Figure 2.4. Considering the vertical pressure distribution in the contact patch when the resulting force is before the centre plane of the tire, the friction potential for accelerating is generally higher than that for braking, [Mun12, H2 p.34]. On a rolling tire, the asymmetric pressure distribution in the contact patch also causes a resistance torque, [MW04, p.18], which has to be compensated.

2 Estimation of the friction potential

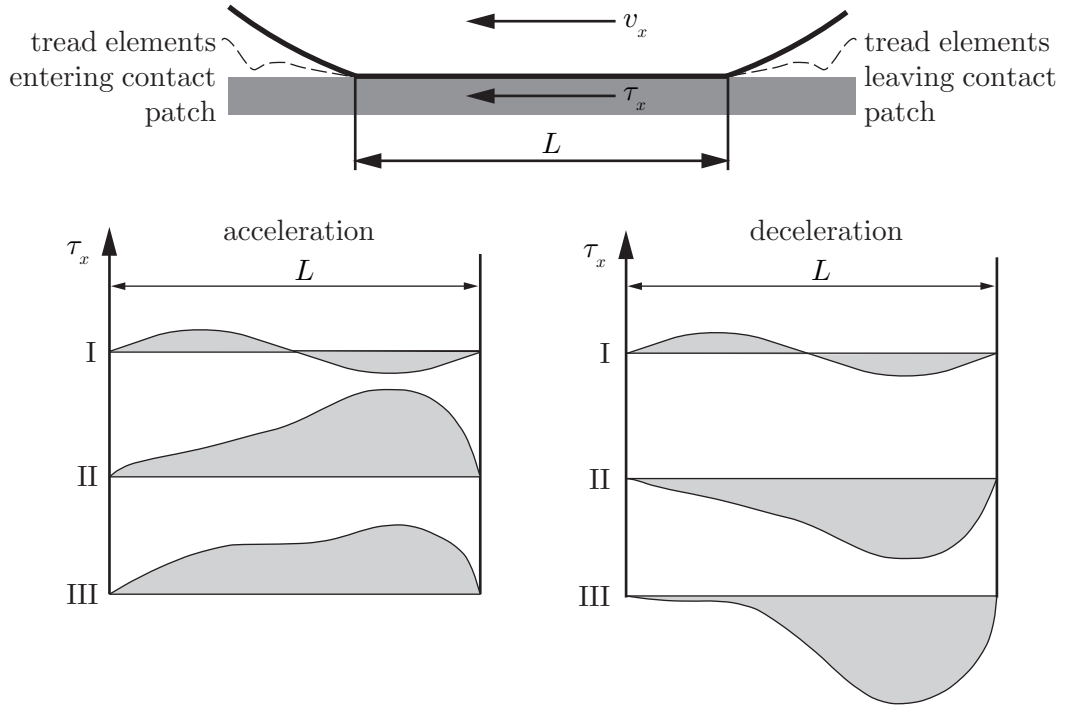


Figure 2.4.: Longitudinal shear stress τ_x in the contact patch between tire and road with length L due to: I. toroid flattening, II. acceleration/deceleration and III. superposition of both conditions, based on *Mundl*, [Mun12, H2 p.34]

Combined friction potential

Figure 2.5 shows a representation of the friction potential for combined slip based on the Krempel diagram. In the Krempel diagram, the lateral tire forces are shown with respect to the longitudinal tire forces for a constant normal force, [HE11, p.62]. The combined friction potential consists of the maximum combined tire forces (i.e. the outer limits of the Krempel diagram) divided by the normal force. This representation is connected to Kamm's circle for $\mu_x^{\max} = \mu_y^{\max}$, but also considers different friction potentials for braking, accelerating and cornering. Figure 2.5 shows that in the case of combined horizontal tire forces acting on the contact patch, the available friction potential only decreases in either the longitudinal or the lateral direction.

Friction potential on wheel level

The effects mentioned for sliding and slipping rubber are local effects in the contact patch. According to *Roth*, [Rot92, p.8-10,13], the behaviour of the overall system can be described as the sum of these local effects, i.e. the integral of the local effects over the

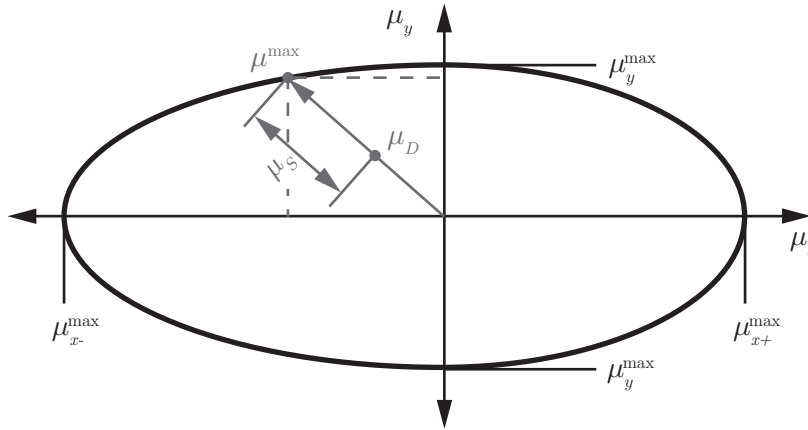


Figure 2.5.: Schematic representation of the combined friction potential based on the outer limits of a Krempel diagram, based on *Heißing et al.*, [HE11, p.62]. The absolute value of μ_{x-}^{\max} is higher than that of μ_{x+}^{\max} when considering the vehicle's different braking, acceleration and cornering capabilities.

effective surface. This consideration applies to local views of the contact patch as well as to global views of one wheel, one axle or a vehicle. The smallest level of scale concerning friction-based force transmission within this thesis are local effects in the contact patch, which are related to the local shear stresses τ_x and τ_y and the normal stress σ_z acting in vertical direction by

$$\mu_{L,x} = \frac{\tau_x}{\sigma_z} \quad \text{and} \quad \mu_{L,y} = \frac{\tau_y}{\sigma_z}, \quad (2.5)$$

cf. [Rot92, p.13]. These local coefficients of friction $\mu_{L,x}$ and $\mu_{L,y}$ are related to a friction coefficient μ_x measurable for a whole wheel by the effective friction area A_e . The friction coefficient μ and the friction potential μ^{\max} for one whole wheel are given by

$$\mu_x = \frac{F_x}{F_z}, \quad (2.6)$$

$$\mu_x^{\max} = \frac{F_x^{\max}}{F_z} \quad (2.7)$$

with the longitudinal tire force F_x and the vertical tire force F_z . Accordingly, the coefficient of friction μ_y in the lateral direction and its friction potential μ_y^{\max} are calculated with the lateral tire force F_y . Nevertheless, even on a free rolling wheel, there are local friction forces due to the shear stresses resulting from the effect shown in Figure 2.4. Thus, although the whole wheel is not yet transmitting forces, the local coefficient of friction is partially utilized ($\mu_L > 0$ at $\mu = 0$), [Rot92, p.13].

2 Estimation of the friction potential

Friction potential on vehicle level

According to *Weber*, [Web04, p.18-19], the relation of the local friction potentials and the global friction potentials for a vehicle with $i = 1, \dots, 4$ wheels in longitudinal and lateral direction is given by

$$\mu_{G,x}^{\max} = \frac{1}{\sum_{i=1}^4 F_{z,i}} \cdot \sum_{i=1}^4 \mu_{x,i}^{\max} \cdot F_{z,i}, \quad (2.8)$$

$$\mu_{G,y}^{\max} = \frac{1}{\sum_{i=1}^4 F_{z,i}} \cdot \sum_{i=1}^4 \mu_{y,i}^{\max} \cdot F_{z,i}. \quad (2.9)$$

Analogously to Equation 2.8, axle-wise values of the friction potential could be defined. One alternative way to calculate the global friction potential μ_G^{\max} can also be derived from the vehicle reaction rather than the wheel's friction potentials $\mu_{x,i}^{\max}$. Excluding air, rolling and climbing resistance, the global friction potentials can be described by the maximum achievable accelerations ba_x^{\max} and ba_y^{\max} . Using the example of the longitudinal direction, the friction potential then reads

$$\mu_{G,x}^{\max} = \frac{ba_x^{\max}}{g}, \quad (2.10)$$

[Web04, p.28]. This representation directly shows the characteristics also given by the Krempel ellipse in Figure 2.5. Without subscripts L or G , μ^{\max} is used for the friction potential on wheel level.

2.1.3. Overview of relevant influencing factors

Several factors influence the friction potential. *Bachmann* conducted a comprehensive literature review and found the relevant factors shown in Table 2.1, [Bac98, p.7-8]. Most of these parameters are thoroughly discussed within the works of *Bachmann*, see [Bac96] and [Bac98]. The parameters can be divided into *tire*, *road*, *intermediary layer* and *vehicle*-dependent parameters.

2 Estimation of the friction potential

Table 2.1.: Systematic overview of influences (parameters and variables) on the friction potential for solid ground based on a literature review by *Bachmann*, [Bac98, p.7-8].

Group of Influences	Influence	Sub-influence
Tire	Type	Tire carcass Tire section Width Tire inflation pressure Dimension
	Tire tread	Tread pattern design Tread arc radius Tread temperature Tread pattern depth Lamellation
	Tread Material	Filling rate Filler Glass temperature Shore hardness Adhesion- / hysteresis char.
Road	Geometry	Micro texture Macro texture Drainage capability Road composition Lane grooves Banking
	Surface	Mineral supplements Material mix Temperature Start condition Stiffness Traffic load (mech.)

2 Estimation of the friction potential

Intermediary layers	Type Depth of water film Temperature Density	Dry friction Water Ice Snow Mud Oil Dirt
Vehicle	Speed Tire forces & moments Wheel inclination Operating point of wheel Superposition	Vertical tire load Camber Slip angle Toe-In Tire deflection Combined slip (long. + lat.) Long. and lateral tire forces

According to *Roth*, the road condition has by far the largest influence on the friction potential, which thus can be used as a measure of the road condition, [Rot92, p.50], Similarly, *Bachmann* mentions the road texture and the presence of water as the parameters with the highest influence on the friction potential, [Bac98, p.13]. Figure 2.6 shows the range of the friction potential for different road conditions shown in a literature research by *Barace*, [Urd12, p.50-51].

In critical driving states, it is not only the road condition that is of interest, but also the ability of a vehicle to accelerate, decelerate and/or corner. Important vehicle-dependent parameters that influence the friction potential are the vertical tire load and the vehicle's longitudinal speed. For a given slip, the horizontal tire force increases in a degressive way with the vertical tire load. This means that doubling the vertical tire load results in a lower horizontal force than twice the horizontal tire force at $F_{z,i}$. As the

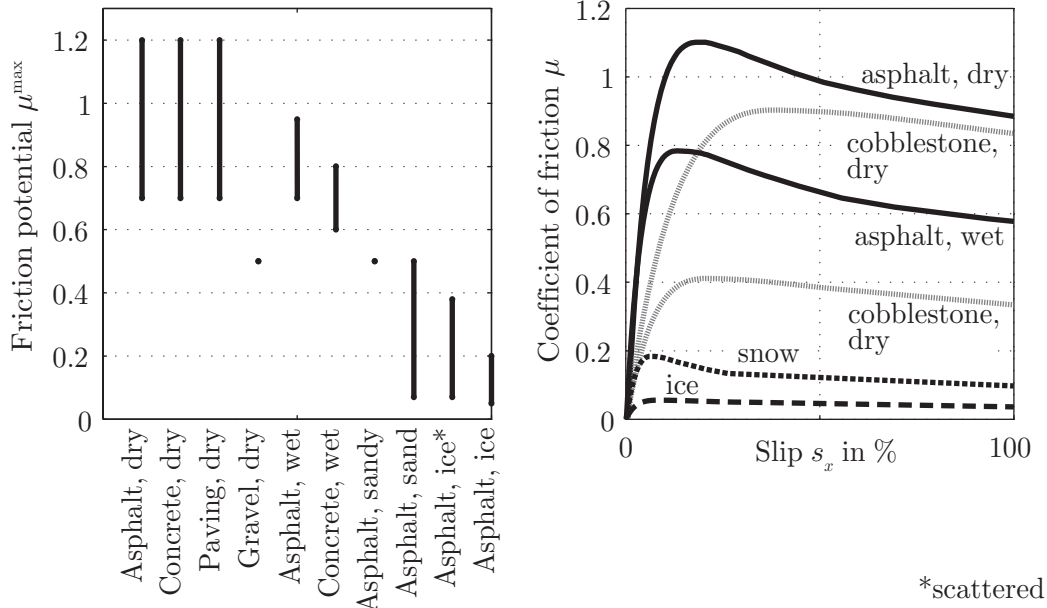


Figure 2.6.: **Left:** Range for the longitudinal friction potentials μ_x^{\max} for different road condition categories used in ZEDATU, [Urd12, p.51]. The representation is based on a literature review by Barace, [Urd12, p.50-51]; see Appendix A for additional information. **Right:** Qualitative representation of the coefficient of friction μ_x displayed versus the longitudinal slip s_x for different road conditions based on Bachmann, [Bac98, p.60].

friction potential μ_x^{\max} is the quotient of the maximum horizontal force and the tire load (see also Equation 2.2), μ_x^{\max} decreases with increasing tire load F_z due to its behaviour, as described in Section 2.1.3. Figure 2.7 shows the declining dependence of the friction potential on the tire load F_z . The influence of the longitudinal speed v_x is shown in Figure 2.8. On dry asphalt, the influence on the friction potential μ_x^{\max} may be excluded within a certain velocity range $v_x \leq 40$ m/s². However, for increasing longitudinal slip values s_x , the coefficient of friction μ_x decreases significantly with v_x . On wet roads, the friction potential shows dependence on v_x . Other than on wet roads, μ_x decreases evenly for all v_x for increasing values of s_x . Also, it has to be considered that the friction potential decreases when both longitudinal and lateral tire forces are acting on the tire, see Section 2.1.2.

Most of the tire-dependent parameters are influenced by the tire design and do not change during driving. The exceptions are ageing and abrasion effects on a long-term scale, and inflation pressure and tire tread temperature on a shorter time scale. The

2 Estimation of the friction potential

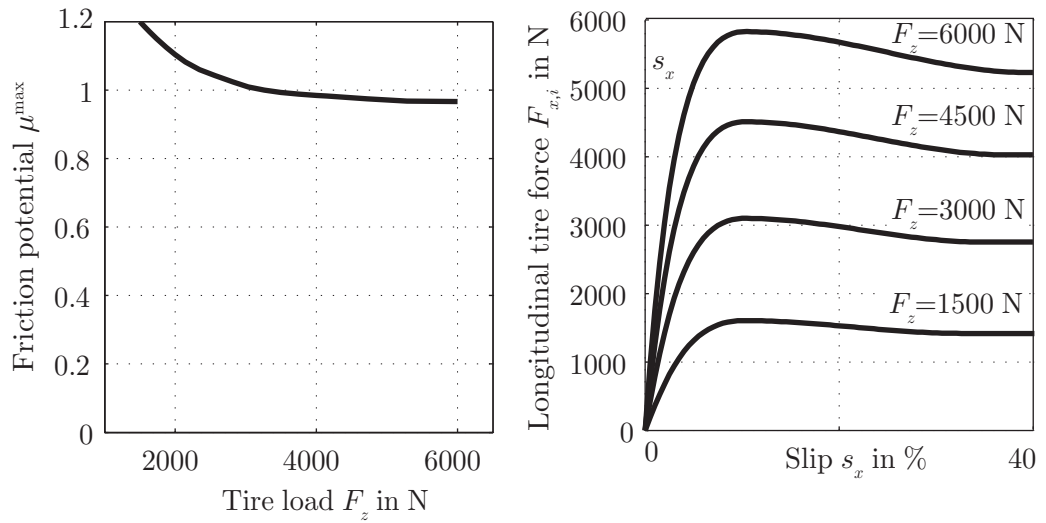


Figure 2.7.: Dependence of the friction potential μ_x^{\max} (left) and the coefficient of friction μ_x (right) on the tire load F_z based on *Hirschberg*, [HW12, p.23].

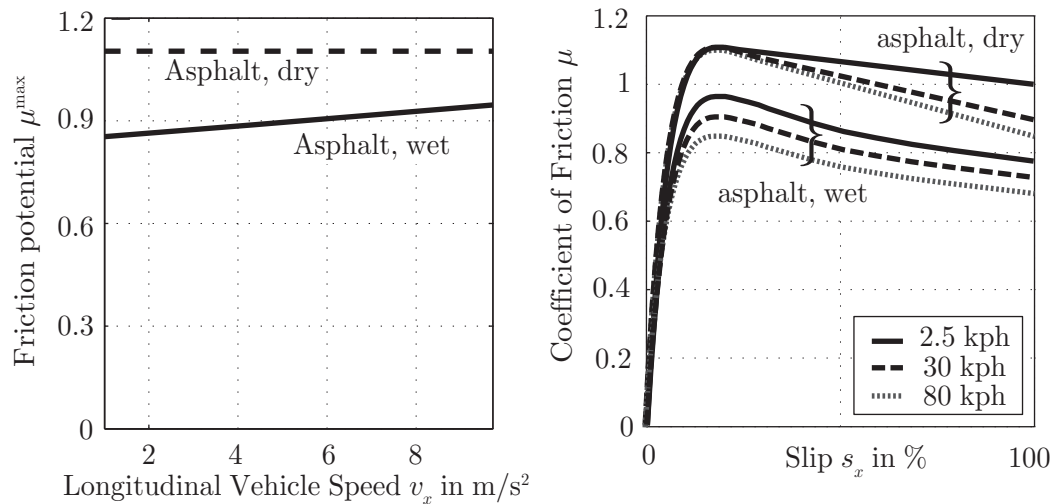


Figure 2.8.: Dependence of the friction potential μ_x^{\max} (left) and the coefficient of friction μ_x (right) on the vehicle's longitudinal speed v_x for dry and wet asphalt, based on *Bachmann*, [Bac98, p.95-96].

latter factors are influenced by the driver's inputs. Decreasing inflation pressure has similar effects on the friction potential as increasing tire load. Many estimation approaches assume the tire characteristics to be known, e.g. [Web04, p.41, 49, 58], and further investigations have shown that knowledge of the tire characteristics increase the estimation

accuracy of the friction potential significantly, [LKE13a]. When the tire characteristics are not known *a priori* (e.g. from measurements on a tire test bench), the tire characteristics have to be identified using defined driving manoeuvres, as for example shown by *Kollreider*, [Kol09, p.83-105], and *Kerschbaumer et al.*, [KKP⁺10] or by e.g. using wheel torque measurements as shown by *Albinsson et al.*, [AFBJ14]. One disadvantage of tire characteristics measured on different test benches is that the results vary significantly, as shown by *Zamow*, [Zam95], and have to be adapted, e.g. [HPRS09]. Nevertheless, *a priori* knowledge of the tire properties is assumed in the present work.

2.2. State of the art

In the last 30 years, extensive research has been conducted on the topic of determining friction potential. In addition to the efforts of individual institutions, Europe-wide projects such as PROMETHEUS¹ and FRICTI@N have made contributions to the identification of the friction potential to increase traffic safety. PROMETHEUS' long-term aim was to enable autonomous driving, wherein sensor-based adaptation to the current road conditions was one sub-project. Environmental sensors and vehicle-reaction-based approaches were developed within this project, see Sections 2.2.1 and 2.2.2. In the FRICTI@N project, information about different existing sensors was used in a novel sensorfusion system, see Section 2.2.4. Within the Intelligent Vehicle and Safety Systems programme, different algorithms to estimate the friction potential were developed using optical sensors, force measurements and measurements of the vehicle's dynamic state, [ABC⁺07].

The existing approaches can be divided into methods that focus on causes that influence the value of the friction potential (i.e. cause-based approaches) and methods that observe variables that are affected by the friction potential (i.e. effect-based approaches). Both kinds of methods can utilize either signals from sensors that are mounted on the vehicle or sensors that are part of road-side infrastructure, see Figure 2.9. Car-to-x communication systems (C2x) are infrastructural systems, see Section 2.2.3. The current road conditions are measured in-situ and sent wirelessly to the vehicle. Since information about the road conditions is available before the vehicle travels on the road, identification of the friction potential ahead of the vehicle is possible. However, since the current tire conditions and driving states are not taken into account, it is not possible to calculate the safety margin. The performance of vehicle-fixed environmental sensors

¹PROgraMme for a European Traffic of Highest Efficiency and Unprecedented Safety

2 Estimation of the friction potential

depends on the vehicle's longitudinal speed v_x and the measurement range d_M , see Figure 2.9. Often, extra sensors are necessary, which cause additional cost and maintenance efforts. Sensors that measure the vehicle reactions incorporate the current vehicle condition and thus enable the calculation of the safety margin. They cannot deliver predictive estimates, as they require a vehicle reaction, and they may or may not cause additional costs, depending on the kind of sensor and the accuracy needed. A trade-off between robustness, accuracy and time delay has to be negotiated for all vehicle-fixed methods.

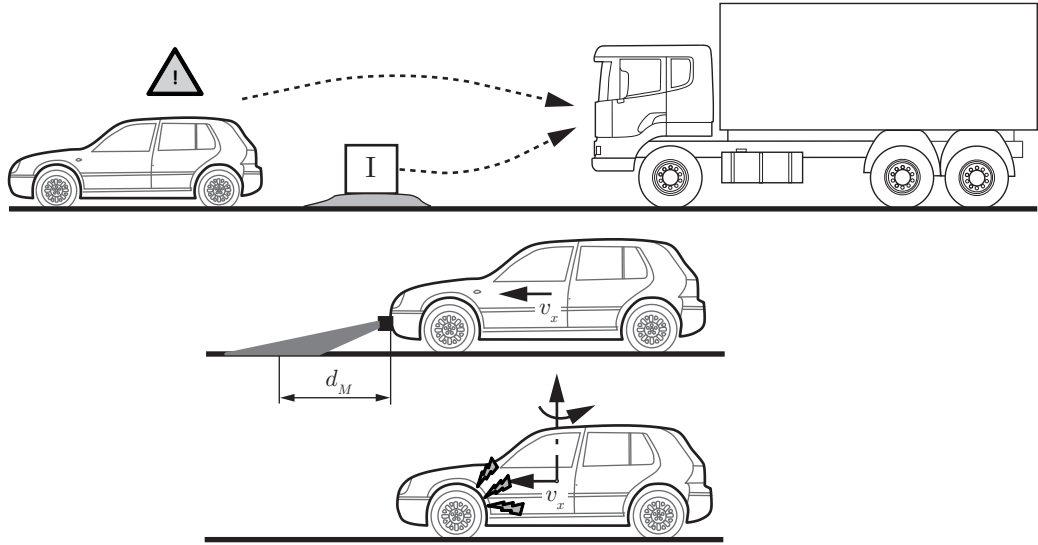


Figure 2.9.: Identification of the friction potential using (**top**) car-to-x (C2x) communication systems such as car-to-car (C2C) and car-to-infrastructure (C2I) communication, (**centre**) on-board environmental sensors that scan the road surface ahead or (**bottom**) on-board sensors that estimate the friction potential based on the measured vehicle reaction

Figure 2.10 shows a classification of vehicle-fixed methods, which will be discussed in the Sections 2.2.1 and 2.2.2. Thereafter, infrastructural systems and sensorfusion-based systems are discussed in Sections 2.2.3 and 2.2.4.

2.2.1. Cause-based approaches

The friction potential μ^{\max} is determined by the influencing parameters shown in Table 2.1. For cause-based approaches, the conditions that have the highest influence on μ^{\max} (e.g. the presence and condition of intermediary layers, road roughness) are observed, see Figure 2.10. Efforts have been made to detect the following conditions:

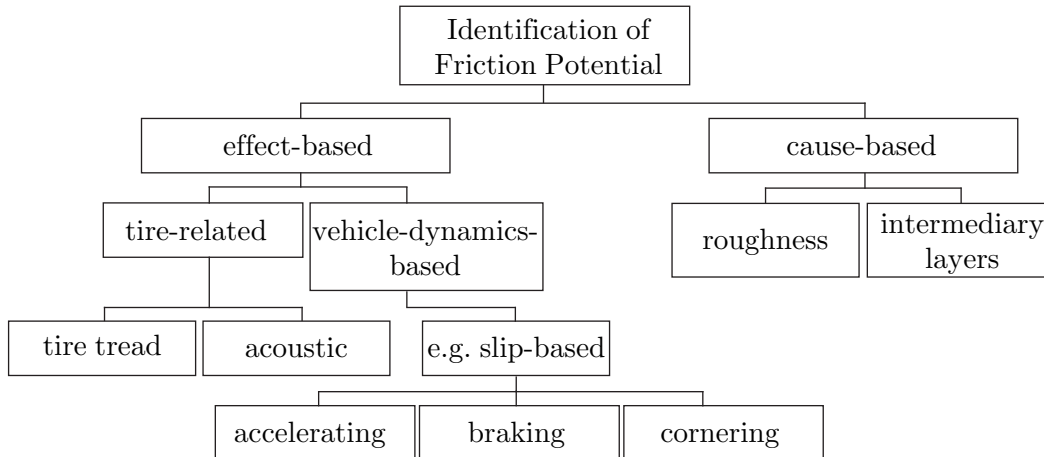


Figure 2.10.: Classification of the vehicle-fixed methods for determining friction potential, based on *Uchanski*, [Uch01, p.18].

- Presence of water, snow and ice on the road
- Water depth
- Precipitation and precipitation density
- Road roughness and texture

Based on the sensor information, the corresponding friction potential has to be derived using additional relations or models. Among other methods, artificial neural networks (ANN) are used to relate sensor information and friction potentials, e.g. [ISAA10]. ANN, which need to be trained with measurement data, are not able to extrapolate conditions that are not within their training data. Past European research projects that have worked extensively with these methods include the aforementioned programmes PROMETHEUS, e.g. [BBES94], and FRICTI@N, [KP09, p.10-11]. To this point, there has been no single sensor available that can estimate the friction potential continuously in a moving vehicle, [KP09, p.12]. In addition, robustness over the whole life-cycle as well as additional costs and maintenance have to be taken into account when considering the use of additional sensors to identify the friction potential.

2.2.2. Effect-based approaches

Rather than measuring causes, effect-based approaches observe parameters that are affected by the friction potential. These methods can be classified as methods that observe

2 Estimation of the friction potential

the dynamic reaction of either the tire or the whole vehicle, see Figure 2.10. Due to their importance for this work, vehicle-dynamics-based approaches will be discussed in greater detail. Tire-related methods comprise direct measurement methods with sensors implemented directly in the tire tread or the wheel rim, e.g. [GH04], [BBB⁺02], as well as [TSH⁺08], and also indirect methods that use effects such as the dependence between the friction potential and the rolling sound of the tire, e.g. [ER92] and [BER92]. Tire-sound-dependent methods are very sensitive to factors other than from the friction potential.

Vehicle-dynamics-based approaches

Lex et al. have proposed a classification system for categorising the large number of published vehicle-dynamics-based approaches for determining the friction potential based on mathematical and physical characteristics, [LEH11]. In the proposed classification system, the mathematical methods for estimating the friction potentials are divided into algebraic, statistical, observer-based and optimization-based methods, see examples in Table 2.2. Algebraic approaches, such as *Holzinger*, [Hol92, p.18-46], have disadvantages when dealing with measurement uncertainties, because they do not integrate any observer or optimization. In this classification system, statistical approaches are also considered observer-based approaches, but they are situated within a Bayesian framework and thus comprise methods such as Kalman and particle filtering. Due to their significance for this work, some of these statistical methods are described below. Most of the methods can be classified as either algebraic approaches or non-statistical observer-based approaches. Table 2.2 shows two examples, *Ahn et al.*, [APT09] and *Hsu et al.*, [HLGG06]. For other observer-based approaches, see *Lex et al.*, [LEH11]. Optimization methods include recursive least square approaches and Fuzzy Logic as proposed by *Ivanov et al.*, [ISAA10], or artificial neural networks (ANN) as proposed in *Lex et al.*, [LKE13a]. The physical classification considers whether μ^{\max} is estimated by using a direct relation with the longitudinal slip or the side slip angle, or by using another physical quantity that is related to μ^{\max} , such as the lateral acceleration and the yaw rate, as shown by *Ding et al.*, [DT10] or the aligning torque, as shown by *Hsu et al.*, [HLGG06]. For further examples and literature references, see also Table 2.2 and *Lex et al.*, [LEH11]. Since many methods have been published, some exemplary methods will be mentioned that are relevant for the method proposed in this work. These mainly include methods that are directly related to slip quantities, as well as methods within the Bayesian framework, see Section 5 for a definition.

Table 2.2.: Mathematical and physical classification of vehicle dynamics based methods to estimate the friction potential with selected examples based on *Lex et al.*, [LEH11]

	Slip based (long., lat.)	Other physical quantities
Algebraic	<i>Holzinger</i> , [Hol92, p.18-34] <i>Rajamani et al.</i> , [RPLG06] <i>Villagra et al.</i> , [VdFM11]	<i>Holzinger</i> , [Hol92, p.35-46]
Statistical (Bayesfilter)	<i>Ray</i> , [Ray97] <i>Gustafsson</i> , [Gus97] <i>Boßdorf-Zimmer et al.</i> , [BZFHK07]	
Observer		<i>Ahn et al.</i> , [APT09] <i>Hsu et al.</i> , [HLGG06]
Optimization	<i>Uchanski</i> , [Uch01] <i>Lee et al.</i> , [LHY04] <i>Svendenius</i> , [Sve07]	<i>Ivanov et al.</i> , [ISAA10] <i>Ding et al.</i> , [DT10] <i>Lex et al.</i> , [LKE13a]

Dieckmann showed that for small values of s_x , the slip needed in order to transmit the same longitudinal tire force F_x is higher for lower μ^{\max} , [Die92, p.32-45]. This means that he empirically proved a correlation between the initial slip slope $k|_{s_x=0}$ and the friction potential μ^{\max} , which can be exploited to estimate μ^{\max} for small values of the longitudinal slip s_x . *Dieckmann* also proposed an approach for calculating so-called micro-slip values of $s_x < 0.1$ % using only wheel speed sensors by summing-up the calculated slip over several wheel revolutions, [Die92, p.19-22, 110]. For a reference value of v_x , the wheel speed sensors of non-driven wheels are used. This can only be done when there is no wheel torque (e.g. no wheel slip), on one axle, which is only true for vehicles with one driven axle and when no braking torque is applied. In addition, the state of the velocity should not change quickly to make it possible to observe the wheel speed differences on the front and rear axles for several revolutions, [Uch01, p.132]. Additionally, the implementation in practice is difficult due to measurement noise and uncertainty, since this effect is very small. *Gustafsson* addressed this problem by implementing a Kalman filter, [Gus97]. He used a linear relation between the initial slip slope $k|_{s_x=0}$ and the demanded coefficient of friction μ_D in the form of $\mu_D = k|_{s_x=0} \cdot (s_x + \delta)$. This relation includes the longitudinal slip s_x and a measurement offset δ that is estimated at the same time as $k|_{s_x=0}$. Applying *Dieckmann's* findings that the friction potential is a function of the estimated $k|_{s_x=0}$, the relevant μ^{\max} can be assigned when additional *a priori* knowledge (e.g. a look-up table) is available for $\mu^{\max}(k|_{s_x=0})$. Unfortunately,

2 Estimation of the friction potential

the variance between different initial slip slopes and corresponding friction potentials μ^{\max} is very high, as shown by *Uchanski*, [Uch01, p.122-124].

Uchanski proposed an approach to detect low-friction surfaces during braking manoeuvres based on the wheel rotational speeds ω_i from the ABS sensors and a measurement of the longitudinal velocity v_x , [Uch01, p.111-122]. The results also show a dependence of lower slip values with μ^{\max} . One crucial factor is accurate and reliable slip calculation. During braking, it is difficult to calculate a reference velocity v_x using only wheel speed sensors as the velocity state changes too quickly. Thus another method for estimating v_x is necessary, [Uch01, p.114]. In addition, the longitudinal tire forces during braking are estimated using wheel speeds and v_x in a filtering technique called optimal FIR derivative, [Uch01, p.76-98].

Ray proposed a model-based approach where the most probable friction potential μ^{\max} is estimated using an adapted form of a particle filter, [Ray97], which is described in Section 5.2. The main element to estimate the friction potential is a tire model that calculates the expected longitudinal and lateral tire forces F_x and F_y for different hypotheses of μ^{\max} . The inputs for the tire model are the tire load $F_{z,i}$, the longitudinal slip s_x , the side slip angle α and the longitudinal velocity v_x . These model-based hypothetical $F_{x,i}$ are then compared to longitudinal tire forces that have been estimated separately using an extended Kalman filter and a vehicle model with the vehicle's state measurements. In a state observer model such as the particle filter, there is a measurement function \mathbf{z} (cf. Equation 5.2) that contains the internal state \mathbf{x} to be observed, which is not directly measured. In the approach mentioned, \mathbf{z} is an estimate from another state observer, i.e. the extended Kalman filter. Thus, this method requires much knowledge about vehicle and tire parameters, as well as signal characteristics in order to obtain the necessary vehicle states with sufficient accuracy (e.g. the longitudinal slip s_x or the slip angle α), in order to have an acceptable estimate of the horizontal tire forces.

Boßdorf-Zimmer also used a Bayesian filter, namely an extended Kalman filter, to estimate μ^{\max} for lateral driving states. He estimated both the slip angle α and μ^{\max} simultaneously using a two-track vehicle and a non-linear tire model. The combined estimation is possible because the influence of α and μ^{\max} affects the lateral tire forces in different ranges of influence, [BZ07, p.75-95], see also Figure 5.2 for the similar relation of the longitudinal tire force $F_{x,i}$ and the longitudinal slip s_x and μ^{\max} .

Both the high amount of required knowledge of vehicle and tire parameter and the signal processing effort can be partially circumvented by using ANN that identify temporal patterns within input and output structures, which requires training the networks before application. *Lex et al.* showed that friction estimation using recurrent neural networks (RNN) was accurate enough to adapt the intervention strategy of an automated emergency brake assist, [LKE13a], [LKE13b]. Nevertheless, the results were not always replicable. Thus, even for similar driving states, different estimates were found. In addition, neural networks are not suitable for extrapolating to conditions they have not been trained for. This means that it would be necessary to conduct extensive training that considers all relevant driving and road conditions with a realistic probability distribution.

Rajamani et al. showed three different approaches for estimating μ^{\max} based on three different sensor configurations, [RPPL12]. In addition, different models were used depending on the sensor configuration, which focused either more on the vehicle or the wheel level. An algorithm based on the wheel motion showed better convergence and estimation accuracy than an algorithm based on a vehicle model. These results are consistent with the results of the sensitivity analysis presented in Section 4.

2.2.3. Car-to-x communication systems (C2x)

In contrast to pure on-board solutions, the idea of C2x approaches is to combine traffic and road-related information about other traffic participants (C2C) and roadside infrastructure systems (C2I). A variety of information (e.g. on traffic density, accidents ahead, road conditions of specific road sections) can be transmitted wirelessly to the vehicle. Currently, the standardisation of data transfer, including data format and content, is being addressed. In 2010, the European Commission issued a mandate to the standardisation organisations CEN², CENELEC³ and ETSI⁴ to develop standards for cooperative systems in intelligent traffic systems, [EotEC09]. The data will be transferred via the standard IEEE802.11, which has been especially developed for wireless ad hoc networks, [Ins10]. One example of a pure infrastructure-based system is the *Weather Data Management System* (WDWS), where information from local sensors on the street (e.g. humidity, road surface temperature, precipitation) is used in combination with large-area weather data (e.g. from weather radar) to determine the actual road condition and to calculate a prognosis. This system is already being used to support road

²European Committee for Standardization

³European Committee for Electrotechnical Standardization

⁴European Telecommunications Standards Institute

2 Estimation of the friction potential

Table 2.3.: Criteria and weighting factors used and described in detail in *Lex et al.*, [LEH11]

Criterion	Weighting Factor
Friction potential (in contrast to demanded coeff. of friction)	8
Online capability of algorithm	7
No additional sensors needed	6
Active intervention not necessary for robust estimate	5
Applicability in ADAS	4
Availability of estimate (longitudinal / lateral / combined tire forces)	3
Ability to predict ahead of vehicle (Yes / Possibly / No)	2
Detection of Gravel (Evaluation of system limits)	1
Availability of estimate (individual tire / per axle / global)	0

and highway maintenance facilities in large areas of Austria and Bavaria, especially in winter, [Ran13].

2.2.4. Sensorfusion

The idea of this application is to use as many different sensor signals as possible to calculate the most probable friction potential. One advantage is that the plausibility of individual signals can be checked by using the combination of other sensors, e.g. [KP09, p.77-80]. In the FRICTI@N programme, for example, information from different existing sensors that measure the vehicle reaction, tire reaction and environmental characteristics were combined using sensorfusion and learning techniques, [KP09, p.10-11]. Ambient temperatures, infrared laser spectroscopy, laser scanner and different cameras were used for this purpose. These methods are expected to become even more important in the future. The involvement of vehicle-dynamics-based approaches in a sensorfusion system will provide a very valuable contribution to a robust and reliable estimate of the friction potential. Nevertheless, this work does not investigate sensorfusion approaches.

2.3. Requirements for a friction potential estimation method

Lex et al. investigated the requirements for an estimation method using vehicle dynamics states to be applied in FCW, AEB and airbag pre-firing, [LEH11]. Nine criteria were presented, which were weighted based on their applicability to the aforementioned systems, see Table 2.3. *Lex et al.* used this criteria to preselect suitable methods out

of 32 published vehicle-dynamic-based approaches, [LEH11]. In a second step, the pre-selected methods were compared using simulation data. This second step also took into account two additional evaluation criteria response time and response threshold of the estimates. Since the application is similar to the one in the present work, these criteria apply here as well. However, some criteria conflict with each other, such as not using additional sensors and enabling detection ahead of the vehicle. In addition, low-rated criteria such as gravel detection and availability for either tire, axle or a global vehicle as well as in the longitudinal, lateral or combined direction are not investigated in detail. However, combined estimation per tire, although not mandatory, is favoured. The investigation in *Lex et al.* also showed that there was no proposed method that worked under all driving states, [LEH11]. Most of the investigated methods were optimized for a particular driving manoeuvre, such as pure braking or pure cornering. Since it is a prerequisite that the algorithm proposed in this work functions for all driving manoeuvres, this criterion has been added. Since the criteria for estimation accuracy and time delay depend on the application (see Section 1.3), they are considered in the criterion *applicability to ADAS*. As one important condition, robustness is a prerequisite for all automotive applications. These requirements lead to the method presented in Chapter 5.

An alternative method to evaluate the performance of estimators for the friction potential was presented by *Bruzelius et al.*, [BSY⁺10]. This approach can be used to evaluate ready algorithms and sensors using vehicle measurements on different road surfaces.

3. Vehicle model

This chapter derives a model for vehicle and environment that is suitable for both the sensitivity analysis (see Section 4) and the tire road friction observer (see Section 5). The focus of this work is solely limited to variables that are related to the vehicle dynamics and are available in a vehicle equipped with ESC, see Section 2.3. This limitation excludes any kind of optical sensors, such as radar, laser or camera-based systems. In addition, all variables need to be measured or estimated on board a vehicle, which excludes C2x applications.

To ensure the transferability of the results of the sensitivity analysis in Section 4 to the observer presented in Section 5, the same model considerations apply. The sensitivity analysis presented in Section 4, which is used to derive the necessary parameters for the tire/road friction observer, does not need to be real-time capable, as it is only used for parameter design. Nevertheless, the model has to be suitable for the proposed procedure, and the computational effort depends on the model complexity. In comparison, the model used for the tire/road friction observer must be designed with real-time ability and robustness, see Section 5. The two applications share the requirement that the tire/road contact has to be represented with sufficient accuracy, see Section 3.1.

Section 3.1 investigates the necessary model complexity in terms of a trade-off between computational effort and accuracy, within the limitations on available variables, and Section 3.2 then presents the vehicle model derived from these outcomes.

3.1. Assessment of required model accuracy

The same model considerations for both the sensitivity analysis (cf. Section 4) and the tire/road friction observer (see Section 5) are chosen in order to ensure transferability of the results of the sensitivity analysis to the observer development. This may seem limiting for the sensitivity analysis. However, this investigation is already limited in terms of mathematical model complexity that can be processed with the proposed method.

3 Vehicle model

Thus, as both the sensitivity analysis and the observer design share the same requirements on the tire/road contact, the some model considerations apply for reduction of model complexity.

To investigate the sensitivity of vehicle dynamic variables to the friction potential, the vehicle model needs to accurately represent the horizontal tire forces, the slip quantities and the wheel speeds for each wheel. The model is supposed to cover a wide variety of driving states, including situations near the physical limits. To keep computational effort manageable, model complexity must be kept low, while keeping model accuracy in mind. To validate whether a simplification of the vehicle model maintains an acceptable accuracy, an analysis based on a simulation with a model with higher model complexity was performed with different parameter settings and sub-model complexities. This assessment of required model accuracy is not to be confused with the main assessment of model sensitivity in Section 4.

In order to quantify the influence of different model parameters, a reference simulation with a model containing all modelled physical phenomena is compared to simulations where these phenomena are successively deactivated. For this investigation, a vehicle model consisting of sprung and unsprung bodies with a total of 14 degrees of freedom (DOF) was used, see Figure 3.1. The model was validated with measured data obtained with an Opel Combo 1.6 CNG, [Roj12, p.13-15].

3.1.1. Evaluation criteria

The main evaluation criterion is the mean relative deviation of the vehicle state variables between a reference simulation and a parameter or sub-model variation. Based on *Weber*, the mean relative deviation $\overline{\Delta w}$ for an exemplary variable w can be calculated by comparing the time signal of the state variable w^{ref} from the reference simulation and w^{var} from the variation simulation by

$$\overline{\Delta w} = \frac{\int |w^{\text{ref}} - w^{\text{var}}| \cdot dt}{\int |w^{\text{ref}}| \cdot dt}, \quad (3.1)$$

see also Figure 3.2 for a graphic depiction, [Web04, p.70-79]. It is important to mention that the time integrals used in Equation 3.1 do not consider kinematic couplings of the state variables. For example, the relation $\int b\omega_z dt = \psi$ is only valid without considering roll and pitch motion of the chassis on an even road. The considerations shown in Equation 3.1 are only used to evaluate the relative change of a variable w between

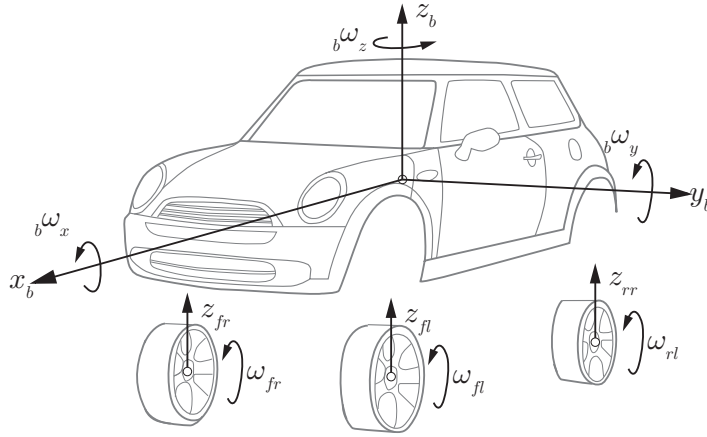


Figure 3.1.: Degrees of freedom (DOF) of vehicle model used for model complexity evaluation. The DOF include the vehicle's body translational $\{x_b, y_b, z_b\}$ and rotational $\{{}^b\omega_x, {}^b\omega_y, {}^b\omega_z\}$ degrees of freedom, as well as the wheels' vertical displacements $\{z_{fl}, z_{fr}, z_{rl}, z_{rr}\}$ and the wheel rotational speeds $\{\omega_{fl}, \omega_{fr}, \omega_{rl}, \omega_{rr}\}$, with the rear right wheel ($i = rr$) not displayed here. The model is based on *Rojas Rojas*, [Roj12, p.13-15], the graphic depiction is modified from *Hirschberg*, [HW12, p.160].

different driving manoeuvres, cf. Figure 3.2. Normalising the mean deviation with the reference curve for each time step enables the comparison of manoeuvres at different longitudinal speeds and friction potentials. With an $\overline{\Delta w}$ of 0 %, the variation of model parameters does not have any effect on the variable investigated. With increasing $\overline{\Delta w}$, the influence of the model parameter increases for the manoeuvre evaluated. With this definition, $\overline{\Delta w}$ is not limited to 100 %.

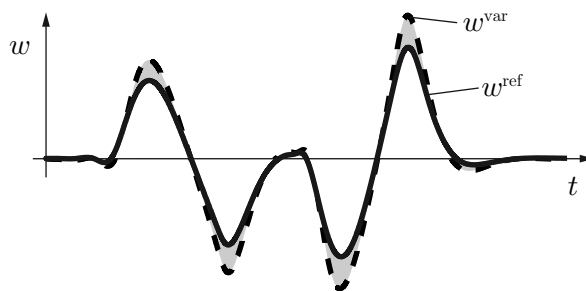


Figure 3.2.: Time signal of an exemplary variable w for both reference setup (w^{ref}) and varied model setup (w^{var}). The area between the two curves is the basis for the mean relative deviation $\overline{\Delta w}$ based on *Weber*, [Web04, p.75]

3 Vehicle model

For all manoeuvres and all model parameters, both the friction potential μ^{\max} and the vehicle's speed v_x are varied. The mean relative deviation for each state variable and each manoeuvre is then displayed as a function of both μ^{\max} and v_x , see Figure 3.3 as an example. The state variables investigated for longitudinal and lateral manoeuvres are not necessarily the same, see Section 3.1.2. It has to be noted that the criterion of mean relative deviation works very well when a variation of the model setup results in a change of amplitude of the investigated variable, but it fails in the rare cases when the variation of the model setup results in a phase shift, such as for quantifying the influence of dynamic tire forces, e.g. Table 3.2 and Table 3.3. Thus, for high mean relative deviation values, the time signals of the respective variable is also examined regarding phase shift. In these cases, the phase shift $\Delta\phi_w$ of a variable w is a second evaluation criterion. The limits for the mean relative deviation was set at 5 % for all variables and 0.05 s for maximum phase shift in a signal.

3.1.2. Investigated manoeuvres

Three manoeuvres are investigated, including either dynamic longitudinal or dynamic lateral excitation. To assess lateral dynamics, the double lane change manoeuvre (DLC) according to *ISO 3888-1* was chosen, [fSI99]. In this manoeuvre, the vehicle model follows a trajectory based on the track dimensions in *ISO 3888-1* using a lateral control. However, only the difference in the vehicle reaction for the different model parameters was evaluated. It has not been studied whether the course defined in *ISO 3888-1* could be followed by the vehicle in every condition, as this was not an assessment of the modelled vehicle.

The investigated variables include the vehicle's rotational speed ${}_b\omega_z$, which characterises the course of the vehicle. The mean relative deviation $\overline{\Delta\omega_z}$ between the reference model and the simplified model has to be small, in order to ensure a high accuracy of the simplified model. As a measure of the accuracy of modelled driving stability, the side slip angle β is used. Additionally, the mean deviation $\overline{\Delta a_y}$ of the lateral acceleration is evaluated. The lateral acceleration depends on both the yaw rate and the side slip rate $\dot{\beta}$ as another measure of driving stability, cf. Weber, [Web04, p.73]. Since the vehicle model has to be suitable for the analysis of different friction potentials, the tire load $F_{z,i}$ and the lateral tire force $F_{y,i}$ are also examined for each tire i . To ensure that the lateral control to follow the given trajectory is working properly in the model setups compared, the steering wheel angles are compared using its mean relative deviation $\overline{\Delta\delta_S}$. It is a prerequisite for the comparison of the other state variables for every simulation that this

Table 3.1.: Overview of simulated manoeuvres and varied model parameters

	DLC	Acceleration	Deceleration
Reference (all listed phenomena modelled)	x	x	x
No ARB	x	x	x
No wheel kinematics and compliance	x	x	x
Damper & spring linear	x	x	x
Steering ratio constant	x		
Roll centre constant	x		
Pitch centre constant		x	x
No tire dynamics	x	x	x
Effective tire radius constant	x	x	x
Constant tire load	x	x	x
Wheel moment of inertia	x	x	x

deviation remains small in general.

For longitudinal dynamics, both acceleration and deceleration manoeuvres were investigated. Again, the friction potential μ^{\max} and the vehicle's speed v_x are varied. Reference speed profiles for each acceleration and deceleration are defined so that a certain acceleration is kept constant. The vehicle's speed at the beginning of the manoeuvre was not varied. To vary v_x , the reference profiles were multiplied with integer factors. In case an acceleration or deceleration could not be reached because of μ^{\max} being too low, the simulation was stopped and not evaluated. For propulsion, the reference profile started just above $v_x = 0$ with a constant ${}_b a_x = 0.5 \text{ m/s}^2$ up to $\approx 5 \text{ m/s}^2$. For braking, the acceleration was varied between about 1 and 10 m/s^2 . A longitudinal control was used to follow the given speed profiles for these simulations.

The investigated variables for the longitudinal manoeuvres include the longitudinal acceleration ${}_b a_x$ and the longitudinal velocity v_x . Relative mean deviations for these two variables need to be small, in order to ensure small impact of the model variations. When focussing on investigations of the friction potential, accurate modelling of the horizontal tire forces is important. In total, v_x , the wheel speeds ω_i , the tire load $F_{z,i}$ and the longitudinal tire force $F_{x,i}$ are examined for each tire i . Thus, the longitudinal slips $s_{x,i}$ at each tire are implicitly evaluated.

3.1.3. Model parameters

Table 3.1 shows the model parameters that were varied for certain manoeuvres, which are described below. Within the reference simulation, the highest model complexity and standard parameters were used. During variation simulations, only one model or parameter is varied. The specific values used for the vehicle parameters are described in Appendix D.

- **Anti-roll bars (ARB)**

Anti-roll bars (ARB) with linear behaviour were simulated at the front and rear axles in the reference setup, and the stiffness of the ARB for front and rear axle was modelled as zero in the variation setup.

- **Wheel kinematics and compliance**

In the reference setup, the three-dimensional wheel movement during bound, rebound and steering is considered (e.g. camber, toe and caster angle), as well as elastic deformations in the steering system. For the variation setup, the wheels' motions were limited to vertical translation relative to the body and, for the front wheels, a steering motion around the vertical axes. Fixed values of 0 degrees have been used for camber angles, toe and caster angles. In this setup, no compliance was considered, neither for suspension components nor for the steering system.

- **Spring and damper**

The reference setup considers spring and damper characteristics that are based on measured and identified curves, [Roj12, p.205]. The variation setup only considers linear characteristics for both spring and damper.

- **Steering model**

As reference, a steering ratio measured between steering wheel angle and wheel steering angle based on a characteristic measured by *Kollreider* is used, [Kol09, p.69]. It is compared to a constant steering ratio.

- **Roll and pitch centre**

In the reference setup, the roll and pitch axes used were identified using an optimization routine that includes a kinematic model and measurements. For the variation setup, constant points $h_{IC,\phi}$ for roll and $h_{IC,\theta}$ for pitch centre with respect to the ground are modelled.

- **Transient tire dynamics**

The reference model includes tire dynamics for both longitudinal and lateral tire

forces, as described in Section 3.3.2. This setup is compared to pure static tire forces, as derived in Section 3.3.1.

- **Effective tire radius**

In the reference setup, the effective tire radii are calculated as a function of the tire load. The variation setup uses constant tire radii that correspond to the static tire radius r_S in nominal vehicle position.

- **Dynamic vertical tire load**

In the reference setup, the input for the horizontal tire contact force model is the dynamic tire load calculated considering the vehicle's DOF pitch and roll as well as springs and dampers. In the variation setup, the static tire load is used as input for the model of the horizontal tire contact forces.

- **Wheel moment of inertia**

The wheel moment of inertia depends on the mass distribution of the wheel, brake disk, and driveline, as well as the engaged gear. Two setups of constant wheel moments of inertias are compared. As a reference, the decoupled wheel moment of inertia as shown in Table D.2 is used. For the second setup, the value of the wheel moment of inertia when the first gear is engaged is used, which represents the highest moment of inertia.

3.1.4. Results for double lane change manoeuvre

Figure 3.3a) shows the mean relative deviation $\overline{\Delta a_y}$ of the lateral acceleration for the DLC manoeuvre with ARB variation at the front and rear axles. With increasing longitudinal velocity v_x , the lateral acceleration ${}_b a_y$ increases, as does the mean relative deviation $\overline{\Delta a_y}$ between the two model settings compared. Nevertheless, $\overline{\Delta a_y}$ is within the specified limit of 5 %. For example, the mean relative deviation $\overline{\Delta F_{y,rl}}$ of the lateral tire force $F_{y,rl}$ shows a similar tendency, see Figure 3.3b), but exceeds the specified limits and is thus listed in Table 3.2. Both state variables do not show a dependence on the friction potential μ^{\max} .

Table 3.2 shows the maximum mean relative deviations exceeding the limits of 5 % and a phase shift of 0.05 s. The model setups with the highest maximum mean relative deviations are presented in decreasing order. The maximum deviations in Table 3.2 show that lateral tire dynamics, a dynamic tire load distribution, a non-linear steering ratio and anti-roll bars at the front and rear axle have to be considered in the vehicle

3 Vehicle model

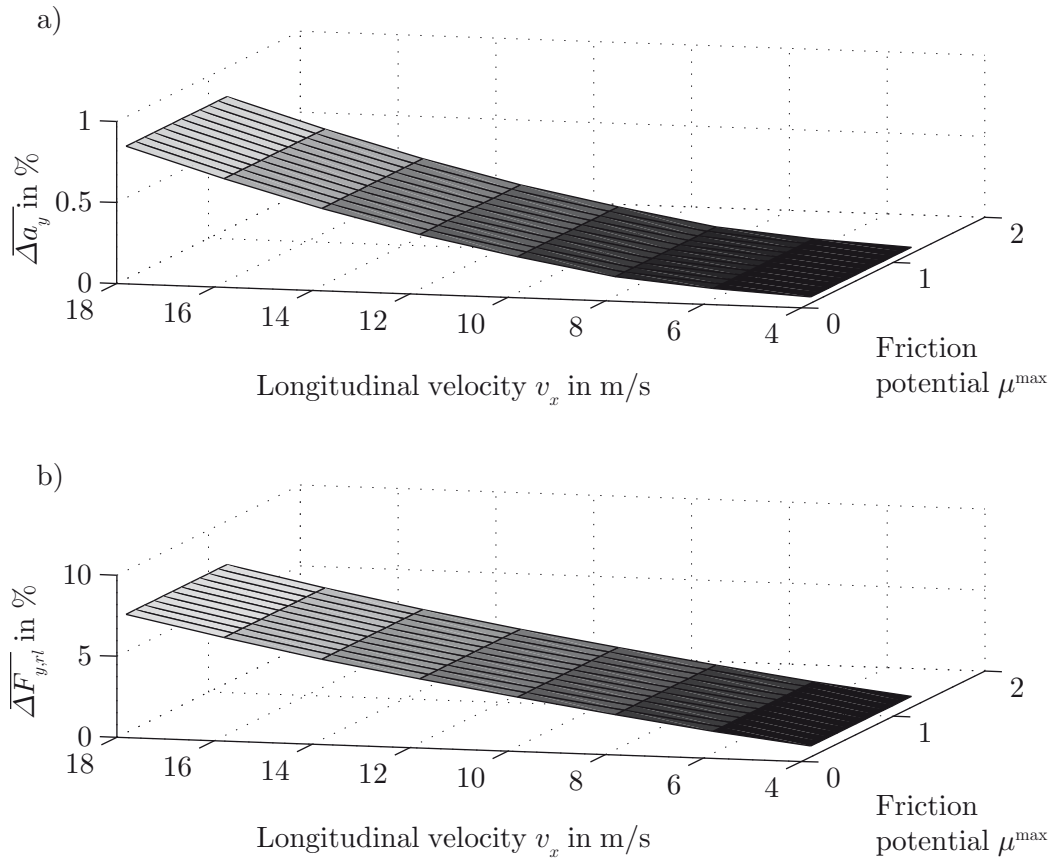


Figure 3.3.: Mean relative deviations as a function of the vehicle's speed v_x and the friction potential μ^{\max} for an ARB model variation in a double lane change (DLC) manoeuvre for a) $\overline{\Delta a_y}$ of the lateral acceleration a_y and b) $\overline{\Delta F_{y,rl}}$ of the lateral tire force $F_{y,rl}$

model. Whereas the effort to include varying tire load, steering ratio and the anti-roll bars is relatively low, the implementation of the tire dynamics require the inclusion of four additional differential equations for the lateral tire forces, see Section 3.3.

3.1.5. Results for longitudinal manoeuvres

Tables 3.3 and 3.4 show the maximum mean relative deviations for the acceleration and braking manoeuvres, respectively. For both manoeuvres, the model setups with the highest influence are presented in decreasing order from left to right. As the investigated vehicle is front-wheel driven, the longitudinal tire forces at the rear axle do not exceed the 5 % limit for the acceleration manoeuvre. For the acceleration manoeuvres, the

Table 3.2.: Mean relative deviations of the state values of DLC manoeuvre for model setups with a deviation higher than 5 % and a phase shift equal or higher than 0.05 s (last row) in decreasing order

Variable	Highest influence	Second highest	Third highest
Lat. acceleration	steering ratio 9.42 %	-	-
Side slip angle	steering ratio >100 %	tire dynamics 70.36 %	ARB 14.13 %
Lat. tire forces	steering ratio 26.07 %	tire load 14.21 %	ARB 7.34 %
Maximum phase shift	tire dynamics 0.35 s	steering ratio 0.2 s	tire load 0.05 s

Table 3.3.: Mean relative deviations of acceleration manoeuvre for model setups with a deviation higher than 5 % and phase shifts higher than 0.05 s in decreasing order for the investigated variables

Variable	Highest influence	Second highest	Third highest
Longitudinal acceleration	tire load 28.46 %	tire dynamics 5.49 %	-
Longitudinal velocity	tire load 28.17 %	-	-
Wheel speeds (front)	tire load 97.78 %	wheel moment of inertia 11.19 %	effective tire radius 10.93 %
Wheel speeds (rear)	tire load 28.2 %	effective tire radius 6.02 %	-
Tire loads	tire load 10.17 %	-	-
Long. tire force (front)	tire load 28.5 %	wheel moment of inertia 12.57 %	-
Maximum phase shift	tire dynamics 0.3 s	-	-

3 Vehicle model

Table 3.4.: Mean relative deviations of braking manoeuvre for model setups with a deviation higher than 5 % and phase shifts higher than 0.05 s in decreasing order for the investigated variables

Variable	Highest influence	Second highest influence
Wheel speeds (front)	effective tire radius 15.71 %	wheel moment of inertia 11.46 %
Wheel speeds (rear)	effective tire radius 15.57 %	wheel moment of inertia 11.45 %
Tire loads	tire load 15.6 %	-
Longitudinal tire forces	tire load 16.07 %	-

longitudinal control cannot follow the speed profile properly at high μ^{\max} when not considering tire force dynamics. A similar effect occurred in the braking manoeuvre, where some combinations of μ^{\max} and the longitudinal vehicle speed could not be reached without tire-force dynamics. This is a controller-specific problem and is not related to the evaluation problem. Therefore, these combinations were not considered in Table 3.4. It is possible that the maximum mean relative deviations of the few cases of simulation without tire force dynamics and near the physical limits are slightly higher than those presented in Table 3.4. Nevertheless, it is unlikely that it exceeded the 5 %, as all model variations not listed have mean relative deviations below 1 %.

According to the results presented in Table 3.3 and Table 3.4, the dynamic tire load distribution, effective tire radii dependent on the dynamic tire loads, varying wheel moment of inertia for the driven axles, and the longitudinal tire dynamics have to be considered. The effort to include varying tire loads and an effective tire radii depending on the dynamic load is relatively low. It is also necessary to include a varying tire load for accurate simulation of lateral manoeuvres, see Section 3.1.4. Since the maximum deviation is slightly above the limit of 5 %, longitudinal tire dynamics are not considered, despite causing a phase shift on longitudinal velocity and wheel rotational speeds. This is acceptable because the tire's longitudinal stiffness $c_{T,x} > c_{T,y}$, and thus the influence of the longitudinal tire dynamics is smaller than that of the lateral tire dynamics, as shown in Section 3.2, [Hir09b]. The variation of the wheel moment of inertia impacts the wheel rotational speeds, see Table 3.3 and Table 3.4. During braking, the gear box is simulated as fully decoupled, and only the wheel's moment of inertia is relevant. During

acceleration manoeuvres, the mean relative deviation $\overline{\Delta\omega_{fl}}$ exceeds the 5 % limit in some regions, as can be seen in Figure 3.4. At lower friction potentials, the wheels

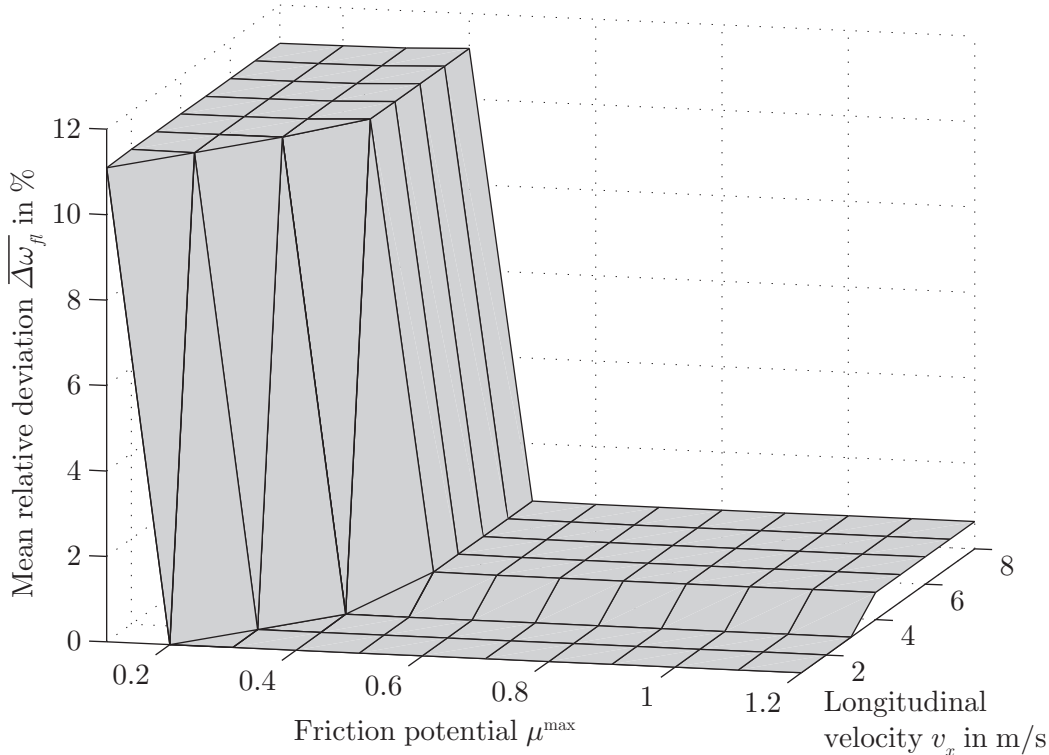


Figure 3.4.: Mean relative deviation $\overline{\Delta\omega_{fl}}$ of the front left wheel’s rotational speed during an accelerating manoeuvre with varied wheel moment of inertia. It can be seen that for low $\mu^{\max} \leq 0.5$, there is an abrupt change in the characteristics. This occurs as the front wheels start to spin in order to be able to follow the given speed profile. The variation of the moment of inertia results in different wheel rotational accelerations that influence $\overline{\Delta\omega_{fl}}$ as shown.

are more likely to spin. This high wheel rotational acceleration is responsible for the high influence of the wheel’s moment of inertia on $\overline{\Delta\omega_{fl}}$. By monitoring the wheel rotational speeds $\Delta\omega_i$ and the wheel rotational speeds ω_i of the driven wheels during the sensitivity analysis, it can be assured that the deviation of the wheel speeds of the driven wheels remain within acceptable limits. This does not restrict the analysis, as situations with high wheel rotational speeds rarely occur and are prevented in vehicles with traction control systems (TCS). The influence on non-driven wheels can be entirely omitted due to low wheel rotational acceleration during acceleration manoeuvres, which is also confirmed by the results of this investigation.

3.2. Selected vehicle model

The investigation in Section 3.1 showed that damper and spring excitation caused by forces that act in the centre of gravity have little impact. As vertical movement caused by road induced excitation is eliminated, the degree of freedom in vertical direction for the chassis and each wheel can be omitted. In addition, since the influence of wheel kinematics and compliance proved to have little impact for this investigation, suspension and wheel kinematics do not need to be considered. As the movement of the chassis relative to the tire is also not of interest, the rotational DOF of the chassis around x_b and y_b axis are omitted, cf. Figure 3.1. In summary, the assessment of the required model accuracy in Section 3.1 showed that the following investigated phenomena have to be considered in the selected vehicle model:

- a non-linear steering ratio,
- front and rear ARB stiffness (not zero),
- vertical tire load variation,
- transient lateral tire dynamics and
- effective tire radii depending on the vertical tire load.

In addition to a standard single-track model, such as the one proposed in [RS40], and the aforementioned phenomena, the wheel rotation of all four wheels and non-linear horizontal tire characteristics are considered. The model equations are now explained in the following sections.

In the global coordinate system $\{\mathcal{O}_g, x_g, y_g, z_g\}$, three degrees of freedom remain for the global position vector ${}_g\mathbf{y}$, which reads

$${}_g\mathbf{y}(t) = \begin{bmatrix} x_g \\ y_g \\ \psi \end{bmatrix}. \quad (3.2)$$

In the vehicle-fixed coordinate system $\{\mathcal{O}_b, x_b, y_b, z_b\}$, 7 degrees of freedom remain for the generalised velocity vector ${}_b\mathbf{z}$,

$${}_b\mathbf{z}(t) = \left[v_x \quad v_y \quad {}_b\omega_z \quad \omega_{fl} \quad \omega_{fr} \quad \omega_{rl} \quad \omega_{rr} \right]^T. \quad (3.3)$$

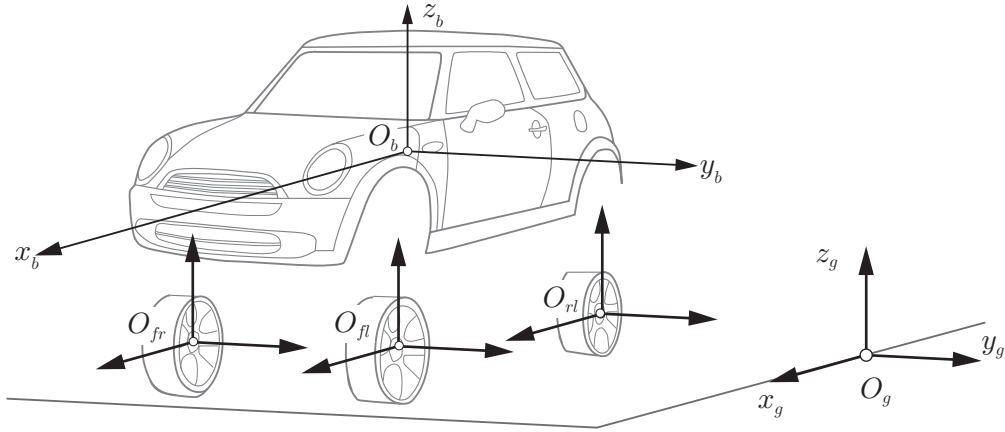


Figure 3.5.: Global coordinate system $\{\mathcal{O}_g, x_g, y_g, z_g\}$ (inertial), vehicle-fixed coordinate system $\{\mathcal{O}_b, x_b, y_b, z_b\}$ and wheel-fixed horizontal coordinate systems $\{\mathcal{O}_i, x_i, y_i, z_i\}$ for wheel index $i = \{fl, fr, rl, rr\}$ (with wheel $i = rr$ not displayed) based on *ISO 8855*, [fSI11]; graphic representation modified from *Hirschberg*, [HW12, p.160].

Figure 3.5 shows all coordinate systems used, which are based on *ISO 8855*, [fSI11]. The position of the vehicle with respect to the global coordinate system \mathcal{O}_g is described with the coordinates x_g and y_g , and the orientation of the vehicle's longitudinal axis with respect to the x_g axis with the yaw angle ψ . The relationship between ${}_g\dot{\mathbf{y}}$ and ${}_b\mathbf{z}$ reads

$${}_g\dot{\mathbf{y}} = \mathbf{T}_b^g({}_g\mathbf{y}) \cdot {}_b\mathbf{z}, \quad (3.4)$$

with the rotation matrix

$$\mathbf{T}_b^g = \begin{bmatrix} \cos \psi & -\sin \psi & 0 & 0 & 0 & 0 \\ \sin \psi & \cos \psi & 0 & 0 & 0 & 0 \\ 0 & 0 & 1 & 0 & 0 & 0 \end{bmatrix}. \quad (3.5)$$

The resulting equation of motion reads

$$\mathbf{M} \cdot \dot{\mathbf{z}} + \mathbf{k} = \mathbf{q} \quad (3.6)$$

and includes the mass matrix \mathbf{M} , gyroscopic and centrifugal forces \mathbf{k} and the vector of applied forces \mathbf{q} . The equation of motion applies in the moving coordinate system \mathcal{O}_b which is located in the vehicle's centre of gravity, cf. *ISO 8855*, [fSI11]. The mass matrix \mathbf{M} in Equation 3.6, which includes the vehicle mass m_b and the moments of inertia of

3 Vehicle model

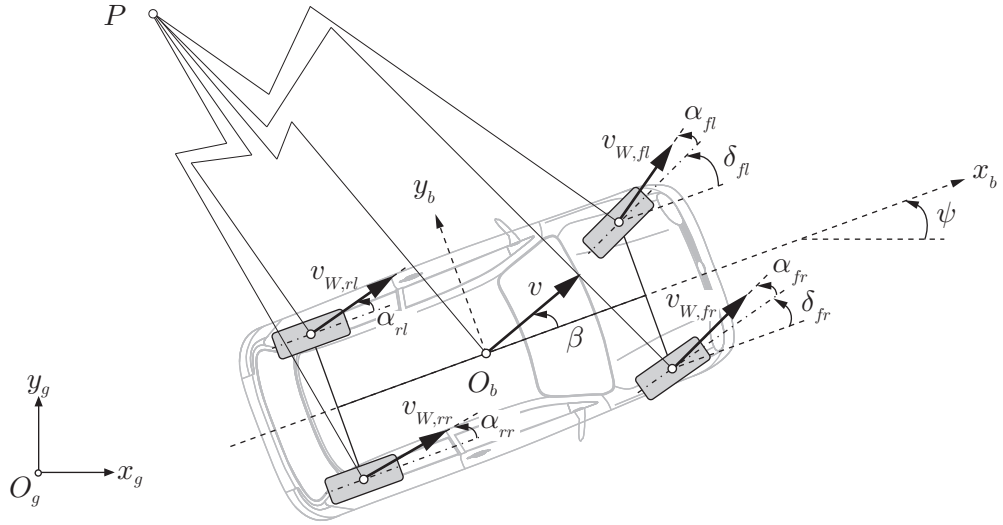


Figure 3.6.: Kinematic quantities of two-track vehicle model including the four wheels' lateral slip angles α_i , wheel steering angle δ_i , and velocities $\mathbf{v}_{C,i}$, as well as the vehicle's velocity \mathbf{v} and the side slip angle β , based on *Eichberger*, [Eic11, p.147]; graphic depiction modified from *Hirschberg*, [Hir13, p.69].

the vehicle I_z and the wheels I_i , reads

$$\mathbf{M} = \begin{bmatrix} m_b & 0 & 0 & 0 & 0 & 0 & 0 \\ 0 & m_b & 0 & 0 & 0 & 0 & 0 \\ 0 & 0 & I_z & 0 & 0 & 0 & 0 \\ 0 & 0 & 0 & I_{fl} & 0 & 0 & 0 \\ 0 & 0 & 0 & 0 & I_{fr} & 0 & 0 \\ 0 & 0 & 0 & 0 & 0 & I_{rl} & 0 \\ 0 & 0 & 0 & 0 & 0 & 0 & I_{rr} \end{bmatrix}. \quad (3.7)$$

The gyroscopic and centrifugal forces are given by $\mathbf{k} = m_b \cdot \begin{bmatrix} -b\omega_z \cdot v_y & b\omega_z \cdot v_x & 0 & 0 & 0 & 0 & 0 \end{bmatrix}^T$, and the applied forces \mathbf{q} , which read

$$\mathbf{q} = \begin{bmatrix} b \sum F_x \\ b \sum F_y \\ \mathcal{O}_b \sum M_z \\ \mathcal{O}_{fl} \sum M_{C,fl} \\ \mathcal{O}_{fr} \sum M_{C,fr} \\ \mathcal{O}_{rl} \sum M_{C,rl} \\ \mathcal{O}_{rr} \sum M_{C,rr} \end{bmatrix}, \quad (3.8)$$

with the sum of all applied forces $b \sum F_x$ and $b \sum F_y$ acting on the vehicle in the longitudinal and lateral directions, the sum of the moments $\mathcal{O}_b \sum M_z$ on the vehicle's chassis around the z_b axis and the sums of the wheel moments $\mathcal{O}_i \sum M_{C,i}$ around the y_i axis.

3.2.1. Applied forces

The vector of applied forces \mathbf{q} in Equation 3.6 contains different forces, which are shown in Figure 3.7 and explained in this section. The first two rows of \mathbf{q} contain the applied forces for the linear momentum in longitudinal and lateral direction, which read

$$b \sum F_x = \sum_i b F_{x,i} - F_A - F_{W,x} - m_b \cdot g \cdot \sin \beta_r, \quad (3.9)$$

$$b \sum F_y = \sum_i b F_{y,i} - F_{W,y}. \quad (3.10)$$

The applied forces include the horizontal tire forces $bF_{i,x}$ and $bF_{i,y}$ for each tire i in the body coordinate system \mathcal{O}_b , as shown in Figure 3.7, the aerodynamic force F_A , additional wind forces $F_{W,x}$ and $F_{W,y}$ and the climbing resistance $m_g \cdot g \cdot \sin \beta_r$, which contains the slope β_r . With the tire model in Section 3.3, the horizontal tire forces $F_{x,i}$ and $F_{y,i}$ are calculated in the i -th wheel's coordinate system \mathcal{O}_i and, for the front wheels, have to be transformed by

$$\begin{bmatrix} bF_{i,x} \\ bF_{i,y} \\ 0 \end{bmatrix} = \mathbf{T}_i^b \cdot \begin{bmatrix} iF_{i,x} \\ iF_{i,y} \\ 0 \end{bmatrix}. \quad (3.11)$$

3 Vehicle model

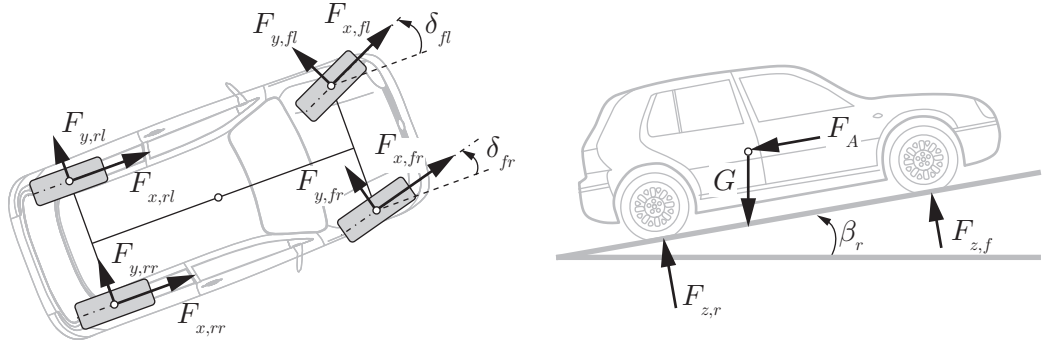


Figure 3.7.: Kinetic quantities of the two-track vehicle model including the horizontal tire forces $F_{x,i}$ and $F_{y,i}$, the aerodynamic force F_A , the weight force $G = m_b \cdot g$ and the vertical forces $F_{z,j}$, based on *Eichberger*, [Eic11, p.148]; graphic depiction modified from *Hirschberg*, [Hir13, p.43, 69].

The rotation matrix \mathbf{T}_i^b reads

$$\mathbf{T}_i^b = \begin{bmatrix} \cos \delta_i & -\sin \delta_i & 0 \\ \sin \delta_i & \cos \delta_i & 0 \\ 0 & 0 & 1 \end{bmatrix} \quad (3.12)$$

and contains the wheel's steering angles δ_i , see Section 3.2.4. The linear momentum in the longitudinal direction of the vehicle also involves the aerodynamic resistance force F_A , which reads

$$F_A = \frac{1}{2} \cdot c_D \cdot A_p \cdot \rho_a \cdot v_x \cdot |v_x|. \quad (3.13)$$

The aerodynamic force shows a quadratic dependence on the vehicle's longitudinal speed v_x and considers the air drag coefficient c_D , the projected frontal area A_p of the vehicle and the air density ρ_a which is a function of air temperature and air pressure. Additional wind forces $F_{W,x}$ and $F_{W,y}$ acting on the vehicle body can also be considered. The weight force G , which is given by $G = m_b \cdot g$ with the vehicle's mass m_b and the gravitational acceleration g , contributes to the linear momentum in the longitudinal direction and is directly proportional to the sine of the road slope β_r . The third row of \mathbf{q} contains the angular momentum of the vehicle body, which reads

$$\mathcal{O}_e \sum M_z = \sum_i \begin{bmatrix} r_{x,i} \\ r_{y,i} \\ 0 \end{bmatrix} \times \begin{bmatrix} {}^b F_{x,i} \\ {}^b F_{y,i} \\ 0 \end{bmatrix} \quad (3.14)$$

with $r_{x,i}$ and $r_{y,i}$ being the lateral and longitudinal distances from the vehicle-fixed origin \mathcal{O}_b to the i -th wheel's centre C . The last four rows of \mathbf{q} describe the angular momentums of the four wheels. The applied forces are shown in Figure 3.8. For the wheel i , the applied forces read

$$\mathcal{O}_i \sum M_{c,i} = M_{D,i} - F_{i,x} \cdot r_{S,i} - M_{R,i}. \quad (3.15)$$

The angular momentums of the wheels include the driving or braking torque $M_{D,i}$, which is an input for the simulation, and the longitudinal tire force $F_{x,i}$ with its leverarm, the static tire radius $r_{S,i}$. The rolling resistance $M_{R,i}$ reads

$$M_{R,i} = F_{z,i} \cdot f_{r,i} \cdot r_{S,i} \quad (3.16)$$

with the rolling resistance coefficient $f_{r,i}$ and the tire load $F_{z,i}$. The tire-dependent parameter $f_{r,i}$ is given in Appendix D.

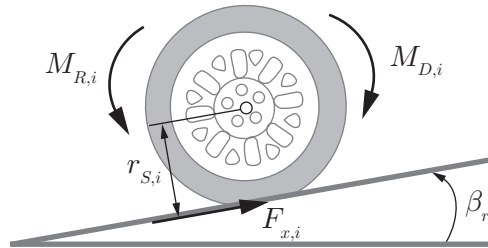


Figure 3.8.: Kinetic quantities for wheel i showing the driving and braking torque $M_{D,i}$, the rolling resistance torque $M_{R,i}$ and the longitudinal tire force $F_{x,i}$, based on *Eichberger*, [Eic11, p.149]; graphic depiction modified from *Hirschberg*, [HW12, p.33].

3.2.2. Vertical tire load variation

Horizontal accelerations in the chassis' centre of gravity produce forces that are supported by the suspension (e.g. the tires, the springs, the anti-roll bars and the dampers). When considering static effects only, the influences of the damper and damping effects of the tires are omitted. Additionally, the following considerations apply only on even roads. The static tire load due to the weight distribution is superposed by the forces necessary to support the longitudinal body accelerations ${}_b a_x$ during braking and accelerating. Thus, the tire loads for the front and the rear axles including tire load variation

3 Vehicle model

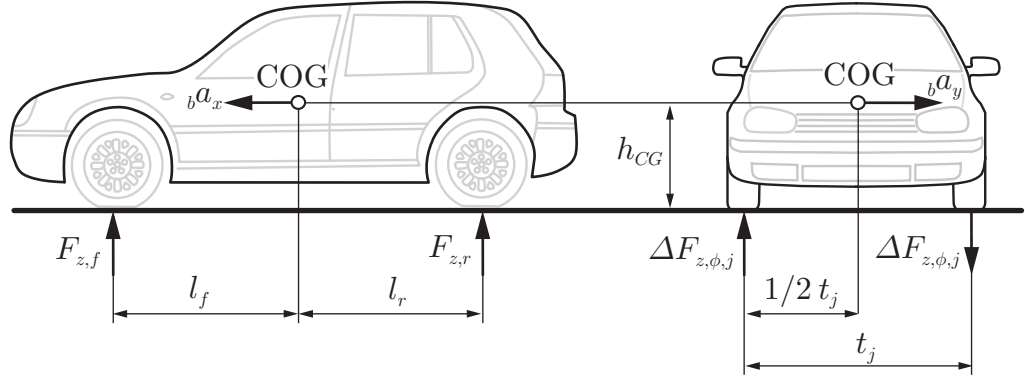


Figure 3.9.: Simplified model for the dynamic tire load variation valid for small pitch and roll angles considering the forces induced by horizontal accelerations in the vehicle's COG: a) longitudinal movement (braking, accelerating), b) lateral movement (cornering); graphic representation based on *Hirschberg*, [HW12, p.7].

due to ${}_b a_x$ read

$$\begin{aligned} F_{z,f} &= m_b \cdot \frac{l_r \cdot g - h_{CG} \cdot {}_b a_x}{l_r + l_f} \quad \text{and} \\ F_{z,r} &= m_b \cdot \frac{l_f \cdot g + h_{CG} \cdot {}_b a_x}{l_r + l_f}, \end{aligned} \quad (3.17)$$

see also Figure 3.9. Equation 3.17 includes the vehicle's mass m_b , the gravitational acceleration g and the position of the centre of gravity, i.e. its height h_{CG} , the distances to the front and the rear axle l_f and l_r and the track width t_j of the j -th axle. In order to apportion the tire load to the four wheels, additional assumptions are necessary, since the vehicle is statically undetermined in the vertical direction with four wheels supporting the load. In the lateral direction, this can be done by considering the rolling torque induced by the lateral body acceleration ${}_b a_y$, which is not equally supported by the front and rear suspension. The amounts supported by each of the j axles depends on the stiffnesses of the tires $c_{T,z}$ in the vertical direction, the anti-roll bars $c_{ARB,j}$ and the springs $c_{S,j}$. The tire and the body spring are connected in series, as shown in Figure 3.10.

During cornering, the wheels on one axle travel in opposite directions, which leads to an increased rolling movement of the chassis. This movement is reduced with the ARB, which act as torsion springs between the right and left side of an axle. The ARB and

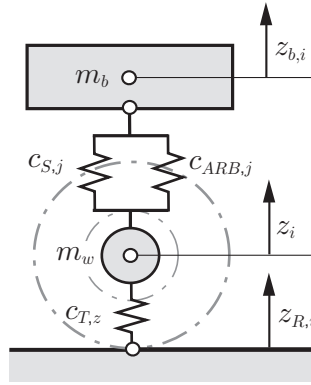


Figure 3.10.: Coordinates $z_{R,i}$, z_i and $z_{b,i}$ of quarter vehicle including the body spring S , the anti-roll bar ARB and the tire R with its corresponding stiffnesses of axle j and wheel i ; based on Hirschberg, [HW12, p.51].

the body springs are connected in parallel. However, unlike the body springs, where the applied forces depend on the spring deflections $\Delta z_{S,i} = z_{b,i} - z_i$, the total force of the ARB depends on the difference of the spring deflections between the left and right sides. In order not to have included the wheel's vertical motion as additional degrees of freedom, a substitution for the roll motion of the chassis is assumed for the vertical tire load transfer, and $c_{ARB,j}$ can be simplified treated as a scalar.

The total stiffnesses of the axles $c_{tot,j}$ are then given by

$$\frac{1}{c_{tot,j}} = \frac{1}{c_{T,z}} + \frac{1}{c_{S,j} + c_{ARB,j}}. \quad (3.18)$$

The percentage of the roll moment supported by each axle is given by

$$p_j = \frac{c_{tot,j}}{\sum_j c_{tot,j}} \cdot 100. \quad (3.19)$$

Thus, the tire load variation $\Delta F_{z,\phi,j}$ due to lateral body accelerations ${}_b a_y$ is given by

$$\Delta F_{z,\phi,j} = m_b \cdot {}_b a_y \cdot p_j \cdot \frac{h_{CG}}{t_j} \quad (3.20)$$

including the tracks t_j of the front and the rear axles. Finally, the tire loads for the four

wheels read

$$\begin{aligned}
 F_{z,fl} &= \frac{F_{z,f}}{2} - \Delta F_{z,\phi,f}, \\
 F_{z,fr} &= \frac{F_{z,f}}{2} + \Delta F_{z,\phi,f}, \\
 F_{z,rl} &= \frac{F_{z,r}}{2} - \Delta F_{z,\phi,r} \quad \text{and} \\
 F_{z,rr} &= \frac{F_{z,r}}{2} + \Delta F_{z,\phi,r}.
 \end{aligned} \tag{3.21}$$

3.2.3. Effective tire radius

The position of the instantaneous centre of rotation IC_R of the free rolling wheel is characterised by the effective tire radius r_e . It is derived from the effective rolling circumference U_e and given by

$$r_e = \frac{U_e}{2\pi}. \tag{3.22}$$

Both r_e and U_e depend on the tire load F_z and the wheel's rotational speed ω_r , as shown in Figure 3.11. According to *Hirschberg*, the effective tire radius r_e , which is located

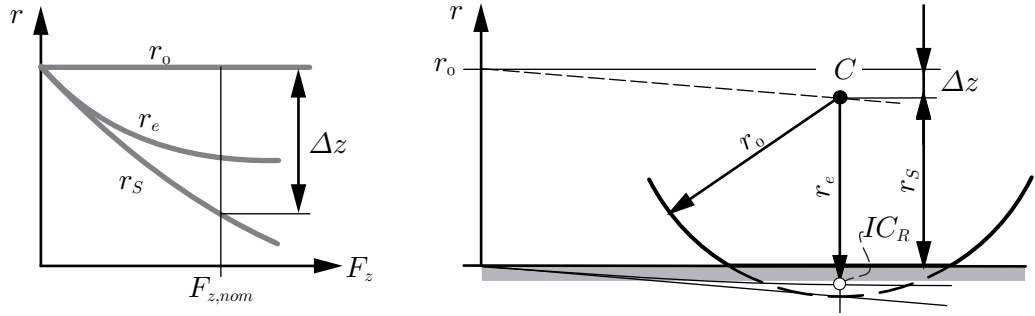


Figure 3.11.: Relation between effective tire radius r_e , static tire radius r_s radius and unloaded tire radius r_0 , according to *Hirschberg*, [HW12, p.17].

between the unloaded tire radius r_0 and the static tire radius r_s , can be approximated based on physical considerations, [Hir09b]. The result of these considerations is given by Equation 3.23. The influence of F_z is considered in the tire's vertical deflection $\Delta z = F_z/c_{T,z}$, where $c_{T,z}$ denotes the linear global tire stiffness at the operating point $F_{z,nom}$. Thus, the effective tire radius may be approximated by

$$r_e \approx \frac{1}{3}r_0 + \frac{2}{3}r_s = r_0 - \frac{2}{3}\Delta z = r_0 - \frac{2}{3} \frac{F_z}{c_{T,z}}. \tag{3.23}$$

3.2.4. Steering model

The relation between the steering wheel angle δ_S and the wheel steering angles δ_i on the four wheels is implemented using measured characteristics. As only the front wheels are steered, the steering angle on the rear wheels remains at zero.

3.3. Tire model

The semi-physical tire model *TMsimple*, developed by *Hirschberg*, is used to calculate the longitudinal, lateral and combined tire forces under steady state conditions on even road and omitting wheel camber, [Hir09a]. The either pure longitudinal or pure lateral force Y acting on the tire at the wheel bottom point W (see also Figure 2.2) is described by

$$Y = K \sin \left(B \cdot \left(1 - \exp \frac{-|X|}{A} \right) \cdot \text{sgn}(X) \right). \quad (3.24)$$

The slip quantity X is either the longitudinal slip s_x calculated with Equation 2.3 or the lateral slip angle α calculated with Equation 2.4. The coefficients K , B and A are not just mathematical parameters, but are related to physical quantities. They depend on the peak value Y_{\max} , the saturation value Y_{∞} and the initial stiffness dY_0 , as shown in Appendix B.1.

3.3.1. Combined tire forces

With longitudinal and lateral slip occurring simultaneously on the tire, the transmittable forces cannot exceed those for pure longitudinal or lateral slip. A model for combined tire forces based on physical similar slip quantities proposed by *Hirschberg* is used, [Hir09a]. In a first step, the tire slip angle α is transformed into an equivalent lateral tire slip s_y , which is given by

$$s_y = \frac{\alpha}{G_s(F_z)}. \quad (3.25)$$

In order to achieve the same initial stiffness for longitudinal and lateral tire characteristics, the weighting factor is defined as

$$G_s(F_z) = \frac{dF_{x0}(F_z)}{dF_{y0}(F_z)} = \frac{A_y \cdot K_x \cdot B_x}{A_x \cdot K_y \cdot B_y}. \quad (3.26)$$

The combined slip vector reads $\mathbf{s} = \begin{bmatrix} s_x & s_y \end{bmatrix}^T$ with its absolute value $|\mathbf{s}| = \sqrt{s_x^2 + s_y^2}$. The basis value F_x^b for the longitudinal tire force is calculated using Equation 3.24 with $|\mathbf{s}|$ being the respective slip quantity, see Figure 3.12, right, for a graphical interpreta-

3 Vehicle model

tion. Accordingly, the basis value F_y^b is calculated using the transformed slip quantity $|\mathbf{s}| \cdot G_s$.

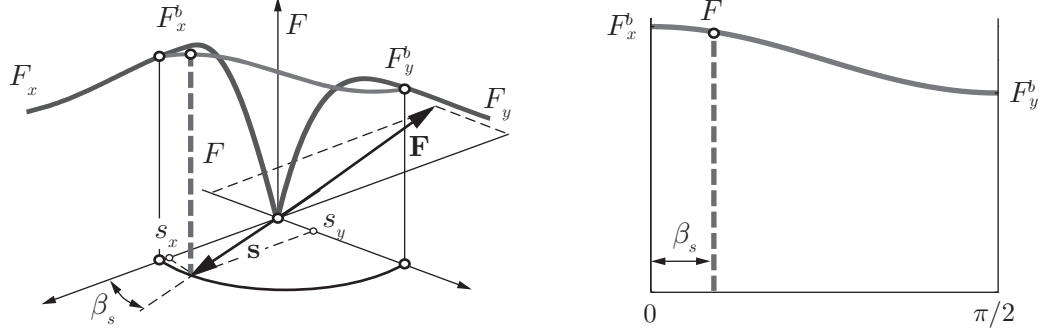


Figure 3.12.: Combined tire force interpolation according to *Hirschberg*, with characteristics F_x and F_y for either pure longitudinal or lateral tire forces. The resulting combined tire contact force \mathbf{F} is assumed to act in the opposite direction as the slip vector \mathbf{s} and is thus defined by β_s . The magnitude of the combined force $F = |\mathbf{F}|$ depends on the basis values F_x^b and F_y^b , [HRW07].

The angle β_s describes the ratio between the longitudinal and the lateral combined slip and is given by $\beta_s = \arctan\left(\frac{s_y}{s_x}\right)$. With the basis values of the tire forces, the combined value of the tire force is interpolated using the cosine function

$$F = |\mathbf{F}| = \frac{1}{2} \left[F_x^b + F_y^b + (F_x^b - F_y^b) \cdot \cos(2 \cdot \beta_s) \right], \quad (3.27)$$

which is dependent on β_s . It has to be noted that the resulting combined tire contact force \mathbf{F} is assumed to act in the opposite direction as the slip vector \mathbf{s} (see Figure 3.12, left). A graphical interpretation of the interpolation based on β_s is shown in Figure 3.12, right. Finally, the resulting tire force vector is given by

$$\mathbf{F} = \begin{bmatrix} F_x \\ F_y \end{bmatrix} = F \cdot \begin{bmatrix} \cos \beta_s \\ \sin \beta_s \end{bmatrix}. \quad (3.28)$$

3.3.2. Lateral tire dynamics

The tire model presented to this point is valid for steady-state conditions. However, the horizontal tire forces react to a change in the slip quantities with a time delay. As the longitudinal stiffness $c_{T,x}$ of the tire is typically about twice as large as the lateral stiffness

$c_{T,y}$, [Hir09b], the longitudinal tire dynamics are omitted within this work. This is also consistent with the investigations made concerning the model complexity, see Section 3.1.

In vehicle dynamics, transient tire dynamics are commonly described by first order filters. For example, the transient tire contact forces F_y^D according to *Rill* depend on the steady-state value of the lateral force F_y by

$$\tau \cdot \dot{F}_y^D + F_y^D = F_y, \quad (3.29)$$

[Ril06], including the time function τ , which reads

$$\tau = \frac{1}{c_{T,y}} \cdot \left(\frac{F_y}{s_\alpha r_e \cdot |\omega_r|} \right) \quad (3.30)$$

with $s_\alpha = \tan \alpha$ and the transport velocity $r_e \cdot |\omega_r|$, with which the particles in the tire tread are moving through the contact patch, [Ril06]. See Appendix B.2 for a more detailed description.

3.4. Environment model

Other than aerodynamic drag, additional wind forces and aerodynamic downforces acting on the chassis are not considered. Vertical excitation of the wheels induced by the road geometry is omitted as roll and pitch are also not considered in the simplified vehicle model, cf. Section 3.1. Thus, only the friction potential and road slope and banking are necessary to describe the environment. These inputs are forwarded to the vehicle model.

4. Sensitivity Analysis

No published record was found on an unprejudiced mathematical analysis that indicated which vehicle state variables are most affected by the friction potential for different driving states, see first research question in Section 1.4. Unlike published approaches, which are heuristic to some degree, the present concept aims at a more mathematical solution to the problem of identifying relevant variables for friction estimation in the first place. In order to find the optimum variables affected by the friction potential for each driving state, a sensitivity analysis was performed based on the vehicle and tire model derived in Section 3. The vehicle's state variables describe the time-varying vehicle reaction and are assumed to contain information on the tire-road contact which can be exploited by an observer. This chapter includes a short introduction to sensitivity analysis, a detailed explanation of the chosen approach and a presentation of the results.

4.1. Sensitivity analysis of ordinary differential equation systems

Sensitivity analyses are often used when the parameters and initial conditions of models are not accurately known and the influence of variations of these parameters is of interest. A parameter is considered sensitive when small changes in the parameter cause large changes in the solution. In the present work, sensitivity analysis is used for another purpose, namely to identify the variables that change with respect to the friction potential depending on the current driving states, see first research question in Section 1.4.

According to *Campolongo et al.*, sensitivity analyses can be categorized as *factor screening*, *global methods* and *local methods*, [CSST00]. Factor screening is useful for finding influential factors in a system with many factors and is thus often used as a preliminary step to reduce factors prior to a local or global method. Global methods apportion the influence of the uncertainty of the input factors on the output factors. This method is helpful when investigating the parameterisation of a model, but distributions

4 Sensitivity Analysis

for each input factor have to be known. For the proposed problem, local methods are suitable, as they are typically modelled as initial-value ordinary differential equations (ODE). Usually, these methods require the calculation of partial derivatives, see Section 4.1.1. Local methods have shortcomings when dealing with the influence of the uncertainty of model parameters, which does not limit the proposed application. The goal is to calculate the (linear) *first-order local sensitivity coefficients* of the non-linear model derived in Section 3 with respect to the parameter μ^{\max} . This work focuses on a *quasi-direct approach*, which means that a direct method based on Equation 4.2 is used, but with the Jacobian \mathbf{J} to be calculated with *automatic differentiation* (AD) rather than using the derivative of analytical functions, [CSST00], see also Section 4.1.1. Although it would be possible to calculate higher order sensitivities with this approach, it is assumed that this would not increase the accuracy considerably, [DG76].

4.1.1. Basic theory of direct sensitivity analysis

It is assumed that the investigated model is given by a non-linear, time-dependent ODE in the form of $\dot{\mathbf{z}} = \mathbf{f}(z_1, \dots, z_n, t, \mathbf{c})$ with $l = 1, \dots, n$ elements in state variable vector \mathbf{z} and $m = 1, \dots, o$ elements in parameter vector \mathbf{c} . The linear sensitivities of the given model with respect to a parameter c_m then read $\mathbf{p} = \frac{\partial \mathbf{z}}{\partial c_m}$. For each of the o parameters, n ODE have to be solved for \mathbf{z} . The sensitivity p_l for the l -th state variable z_l can be found as the time integral of $\dot{p}_l = \frac{\partial}{\partial t}(p_l)$. Applying both the chain rule of differentiation and the rule for interchanging the order of differentiation for mixed partials,

$$\dot{p}_l = \frac{\partial}{\partial t} \left(\frac{\partial z_l}{\partial c_m} \right) = \frac{\partial}{\partial c_m} \left(\frac{\partial z_l}{\partial t} \right), \quad (4.1)$$

and the sensitivity system is thus given by

$$\dot{p}_l = \frac{\partial f_l}{\partial c_m} + \sum_{d=1}^n \frac{\partial f_l}{\partial z_d} \cdot \frac{\partial z_d}{\partial c_m} \quad (4.2)$$

with f_l being the right-hand side of z_l , [DG76]. Using the Jacobian \mathbf{J} , whose (l, d) -th element is $\frac{\partial f_l}{\partial z_d}$, and \mathbf{f}_c being the sensitivity of right-hand side \mathbf{f} with respect to parameter c_m , Equation 4.2 reads

$$\dot{\mathbf{p}} = \mathbf{f}_c + \mathbf{J} \cdot \mathbf{p}. \quad (4.3)$$

4.1.2. Initial values of sensitivities

According to *Dickinson and Gelinas*, the value for the initial sensitivity $p_l(0)$ is defined by its limit

$$p_l(0) = \lim_{\Delta c_m \rightarrow 0} \frac{z_l(c_m + \Delta c_m, 0) - z_l(c_m, 0)}{\Delta c_m}, \quad (4.4)$$

[DG76]. Depending on whether a parameter is an explicit initial condition of any of the state variables z_l or not, two cases can be distinguished. If parameter c_m is not an initial condition of any of the state variables z_l , the term $z_l(c_m + \Delta c_m, 0) - z_l(c_m, 0)$ in Equation 4.4 is zero, and all l initial sensitivities are therefore given by

$$p_l(0) = 0. \quad (4.5)$$

For the second case, it is assumed that parameter c_m is an explicit initial condition of the n -th state variable z_n . Thus, the term $z_n(c_m + \Delta c_m, 0) - z_n(c_m, 0) = \Delta c_m$ in Equation 4.4 results in $p_l(0) = 1$. Thus, the initial sensitivities read

$$p_{l=n}(0) = 1, \quad (4.6)$$

$$p_{l \neq n}(0) = 0. \quad (4.7)$$

4.1.3. Sensitivities of functions related to state variables

In addition to the sensitivity of the state variables, the sensitivity of other variables that depend on these state variables can be of interest. As mentioned in Section 2.2.2, there are existing methods that focus on the vehicle's side slip angle β . In addition, the self-aligning torques at the tires have proven to be a good measure for μ^{\max} in previous investigations, e.g. *Hsu et al.*, [HLGG06]. As with the propagation of error, the sensitivity p_e of $e = f[u(c_m), w(c_m)]$ with respect to the parameter c_m can be written by its first order Taylor series

$$p_e = \frac{\partial e}{\partial c_m} = \frac{\partial e}{\partial u} \cdot \frac{\partial u}{\partial c_m} + \frac{\partial e}{\partial w} \cdot \frac{\partial w}{\partial c_m}. \quad (4.8)$$

Within Equation 4.8, the terms $\partial e / \partial u$ and $\partial e / \partial w$ can be interpreted as weighting factors. So, by knowing the sensitivity of state variables, the sensitivity of other variables that are related to state variables can be expressed. Applied to the side-slip angle

$$\beta = \arctan \frac{v_y}{v_x} \approx \frac{v_y}{v_x} \quad \text{for } \beta \ll 1 \text{ rad}, \quad (4.9)$$

4 Sensitivity Analysis

its sensitivity based on the relation in Equation 4.8 is given by

$$p_\beta = \frac{\partial\beta}{\partial\mu} = \frac{\partial\beta}{\partial v_y} \cdot \frac{\partial v_y}{\partial\mu} + \frac{\partial\beta}{\partial v_x} \cdot \frac{\partial v_x}{\partial\mu}. \quad (4.10)$$

With $\partial\beta/\partial v_y = 1/v_x$ and $\partial\beta/\partial v_x = v_y/v_x^2$, the sensitivity of β to μ^{\max} reads

$$p_\beta = \frac{1}{v_x} \cdot p_{v_y} + \frac{v_y}{v_x^2} \cdot p_{v_x}, \quad (4.11)$$

including $\partial v_y/\partial\mu = p_{v_y}$ and $\partial v_x/\partial\mu = p_{v_x}$.

4.2. Numerical implementation

Dickinson and Gelinas propose an approach in which the model and the sensitivity equations are solved simultaneously, [DG76]. This procedure is only possible when the Jacobian \mathbf{J} is calculated as the partial derivative of an analytical function. Although possible, the many dependencies within the model equations (as shown in Section 4.3) complicate the calculation of an analytical derivative. An alternative method for calculating both the Jacobian \mathbf{J} and \mathbf{f}_c is given by automatic differentiation (AD). AD is neither symbolic nor numerical approximation. It enables the calculation of derivatives accurate to working precision at arbitrary points. Theoretically, it can be applied to every function described in a computable program that can execute elementary arithmetic operations (e.g. additions) and elementary functions (e.g. sine functions). An automated procedure based on the chain rule for derivatives is then applied to this function, and it calculates the desired derivatives, [BH00]. In this work, the automatic differentiation toolbox *Adimat* developed for the computer language Matlab was used, [BBL⁺02]. The calculation of the Jacobian \mathbf{J} and \mathbf{f}_c using AD requires the n model equations to be at least one time differentiable. This does not account for the calculation of the longitudinal slip s_x , see Equation 2.3, where both absolute value and a distinction of cases (e.g. finding the maximum out of two values) have to be considered. It is also necessary to calculate an absolute value for the calculation of combined tire forces, see Section 3.3.1. Thus, these mathematical functions are numerically approximated by the functions shown in Appendix C.1.

Finally, the steps to calculate the sensitivities \mathbf{p} are summarized. In a first step, the differential equation $\dot{\mathbf{z}}$ of the non-linear vehicle model is solved for \mathbf{z} . In a second step, the Jacobian \mathbf{J} and the derivative \mathbf{f}_c are calculated using automatic differentiation.

Table 4.1.: Maximum longitudinal and lateral accelerations based on measurements

Acceleration	Measured value (approx.)
${}_b a_x^{\max}$ (acceleration)	5 m/s ²
${}_b a_x^{\min}$ (braking)	10 m/s ²
${}_b a_y^{\max}$	10 m/s ²

Finally, in a third step, the linear sensitivity model $\dot{\mathbf{p}}$ is solved for \mathbf{p} .

4.3. Sensitivity analysis using vehicle model

The sensitivity analysis is performed on the vehicle model described in Section 3.2. The differential equation system consists of the three equations of motion that describe the movement of the chassis, the four equations that describe the rotational movement of the wheels, and four equations for the lateral tire dynamics. The structure of the vehicle model adapted for the sensitivity analysis is shown in detail in Appendix C. This structure describes the inter-dependencies between the state variables, the inputs to the equations and the investigated parameter μ^{\max} . These inter-dependencies influence not only $\dot{\mathbf{z}}$, but also the Jacobian \mathbf{J} and \mathbf{f}_c and thus the differential equation $\dot{\mathbf{p}}$ of the sensitivities. A simplification is necessary to calculate the tire load variation, as given by Equation 3.22, and the effective tire radius that depends on the tire load variation, as given in Equation 3.23. They depend on the horizontal accelerations and thus on $\dot{\mathbf{z}}$, which is not known before the differential equation system is solved for \mathbf{z} . Since it is assumed that the horizontal accelerations change sufficiently slowly with time, both tire load variation and effective tire radius are calculated with the accelerations of the last time step $k - 1$.

4.3.1. Driving manoeuvres to cover parameter space

Different driving states have to be defined in order to investigate the sensitivity of the state variables with respect to μ^{\max} . The parameter space of driving states is defined by different areas of ${}_b a_x$ and ${}_b a_y$ in the Krempel diagram, as shown in Figure 2.5 and described in Section 2.1.2. It is assumed that for different horizontal accelerations at the vehicle's COG, different state variables are sensitive to a change of μ^{\max} . Thus, the parameter space of possible and realistic horizontal accelerations at the vehicle's COG is to be investigated. The outer boundaries are defined by the maximum accelerations, as shown in Table 4.1. Time-dependent acceleration profiles are used to control the inputs

4 Sensitivity Analysis

of the vehicle model, i.e. the four wheel torques and the front wheels' steering angles, to reach different combinations of longitudinal and lateral accelerations within the parameter space. For the longitudinal and the lateral desired acceleration profile, separate proportional-integral-derivative controllers (PID) was used. This enabled reproducible results of driving states for different friction potentials μ^{\max} within the physical limits as well. A wide range of possible accelerations are covered in the analyses. Thus, manoeuvres are defined that start with either pure longitudinal or lateral acceleration and then traverse the parameter space of combined accelerations in ellipses. Figure 4.1 shows the manoeuvre to cover positive ${}_b a_x$ and ${}_b a_y$ by starting with a pure longitudinal acceleration until a predefined value is reached. Then, the wheels' torques and the front wheels' steering angles are controlled such that an elliptic acceleration characteristics is achieved, as shown in Figure 4.1 (left). Both the predefined value after pure longitudinal or lateral acceleration and the ellipses are varied by a factor f_S in order to reach many conditions in the parameter space, see gray lines in Figure 4.1 as two examples. With a scaling factor $f_S = 1$, the maximum accelerations are simulated as defined by the Krempel diagram, as shown in Figure 2.5 with the maximum values presented in Table 4.1. The temporal representation of the desired values of ${}_b a_x$ and ${}_b a_y$ for the controller are shown in Figure 4.1 (right). These manoeuvres are simulated for both positive and negative ${}_b a_x$. To include manoeuvres with values of ${}_b a_y$ while ${}_b a_x \approx 0$, a manoeuvre similar to the proposed one was added, whereby ${}_b a_y$ is first increased while ${}_b a_x$ remains at zero, and then elliptic behaviour towards positive or negative ${}_b a_x$ is reached.

4.3.2. Validity and limitations

Both the validity and the limitations of the results of the sensitivity analysis depend on the proposed procedure, including the simulated manoeuvres. To find variable sets sensitive to μ^{\max} that only depend on the current driving states, first of all the sensitivity of the state variable must not depend on the time when the driving states are reached (no time-dependence). In addition, the influence of the initial longitudinal velocity $v_{x,0}$ at which the simulation is started has to be known. Finally, it has to be assured that the tendencies of the sensitivities of the manoeuvres that start with longitudinal excitation deliver comparable results to those that start with lateral excitation, in order to be able to compare the results.

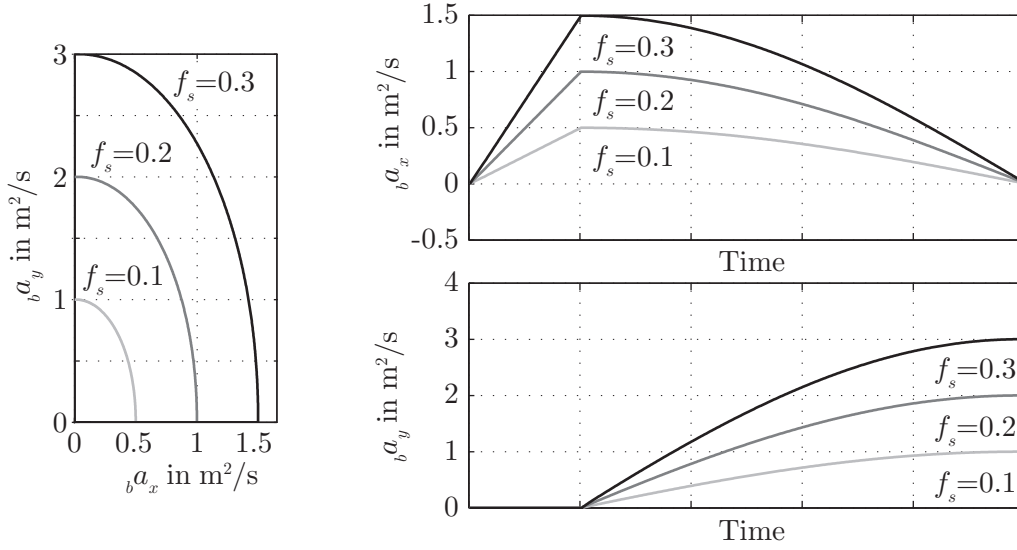


Figure 4.1.: **Left:** Representation of the longitudinal versus the lateral acceleration in the vehicle's COG with elliptic characteristic. The simulated manoeuvre starts with pure positive longitudinal acceleration, followed by a combined longitudinal and lateral acceleration state. The scaling factor f_s is used to scale the desired acceleration profiles. **Top right:** Longitudinal acceleration versus time to achieve the driving states shown on the left. **Bottom right:** Lateral acceleration versus time.

Time dependence of sensitivity

Simulations with different acceleration profiles versus time have to be compared in order to be able to evaluate many states within the parameter space. The higher the desired acceleration is set, the faster a certain state is reached, as shown in Figure 4.2. As mentioned before, the time at which a certain state (in this case a certain longitudinal and lateral acceleration) is reached must not influence the calculated sensitivities \mathbf{p} . Thus, the sensitivity $\mathbf{p} = \partial \mathbf{z} / \partial \mu$ calculated for a certain ${}_b a$ scaled with $f_s = 1$ at t_1 has to be the same as the one for $f_s = 0.5$ at t_2 . For example, Figure 4.3 shows the driving state with pure ${}_b a_x$ of 0.45 m/s^2 and ${}_b a_y = 0$. It is evident that the selected sensitivities $\partial v_x / \partial \mu$ and $\partial \omega_{fl} / \partial \mu$ have congruent characteristics in dependence of μ^{\max} at the investigated longitudinal acceleration of 0.45 m/s^2 , no matter which scaling factor f_s is used for the desired acceleration profile during the simulation manoeuvre. Both the tendency and the absolute values at a certain μ^{\max} are similar for all simulations. This behaviour is the same for the all sensitivities p_i and for all acceleration points not displayed. Thus, time-dependence can be excluded.

4 Sensitivity Analysis

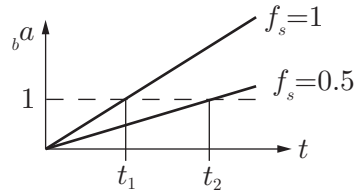


Figure 4.2.: Instants of time t_1 and t_2 at which the driving state of $b a = 1 \text{ m/s}^2$ (pure longitudinal acceleration, no lateral acceleration) is reached for two simulations with different scaling factors f_s for the desired acceleration profile

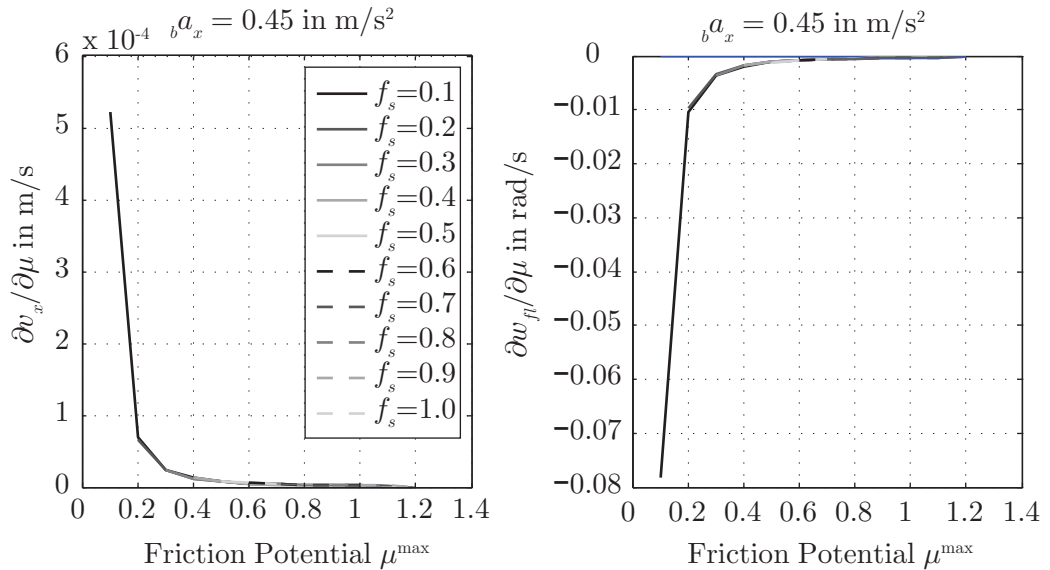


Figure 4.3.: A comparison of the selected sensitivities $\partial v_x / \partial \mu$ (**left**) and $\partial \omega_{fl} / \partial \mu$ (**right**) versus μ^{\max} shows similar behaviour for different scaling factors f_s used to calculate the desired acceleration profile during the simulation manoeuvre. Since the curves are congruent for its simulated μ^{\max} , the sensitivities displayed show no time-dependence, i.e. a dependence on the time it takes to reach the acceleration of 0.45 m/s^2 , for example.

Influence of initial longitudinal velocity

There are two methods with which the influence of the longitudinal velocity on the outcome of the sensitivities can be investigated. Although only one of the methods was performed, both will be described in this section. The influence of the initial longitudinal speed $v_{x,0}$ on the outcome of the analysis can be treated as the investigation of the sensitivity of the model's state variables with regard to the initial value of the longitudinal speed. Then, the same procedure of direct sensitivity analysis can be used

as presented earlier in this chapter. Instead of μ^{\max} , the investigated parameter is then the initial longitudinal speed $v_{x,0}$.

The initial longitudinal speed $v_{x,0}$ can be written as $z_1(0)$, as it is the initial state of the first state variable z_1 . Then, it does not explicitly appear in the right-hand side f_l of the differential equation system \dot{z}_l , [DG76], and \mathbf{f}_c in Equation 4.3 is a zero vector. Thus, $\dot{\mathbf{p}}$ is then given by

$$\dot{\mathbf{p}} = \mathbf{J} \cdot \mathbf{p}. \quad (4.12)$$

According to Section 4.4 (cf. Equation 4.7), the initial values of \mathbf{p} with regard to the initial longitudinal velocity read

$$p_1(0) = 1, \quad (4.13)$$

$$p_{l \neq 1}(0) = 0. \quad (4.14)$$

When calculating the sensitivities with respect to $v_{x,0}$, n equations for \mathbf{p} have to be solved for all simulations. Since the sensitivities with respect to μ^{\max} were already available, another approach was chosen. Like the investigation of the influence of time-dependency in Section 4.3.2, the influence of different initial longitudinal velocities on the outcome of the sensitivities with respect to μ^{\max} was investigated with simulations that start at different v_x .

Figure 4.4 shows that the selected sensitivities depend on the initial longitudinal velocity $v_{x,0}$. With increasing initial speed, the sensitivity $\partial v_x / \partial \mu$ also increases for both pure longitudinal accelerations of 0.45 and 2.45 m/s². With a higher dynamic excitation (e.g. longitudinal acceleration), the sensitivities also increase. The absolute value of the sensitivity $\partial \omega_{fl} / \partial \mu$ shows similar behaviour. It has to be mentioned that the vehicle model does not consider maximum longitudinal velocity of the vehicle or limitations of engine torque. It is obvious that there is a dependency on the initial longitudinal speed $v_{x,0}$. Although the absolute value of the sensitivities changes with the longitudinal speed, it can be assumed that the influence of the velocity affects all state variables to a comparable extent. It seems that the influence could be compensated with a quadratic dependence of the longitudinal speed, for example. In any event, for the observer proposed in Section 5, it is not necessary to know the exact values of the sensitivities. It is more important to know their influence in comparison to the other state variable's sensitivities in a certain region in the parameter space. The results of the sensitivity analysis are only used to select the state variables to be observed in the estimation al-

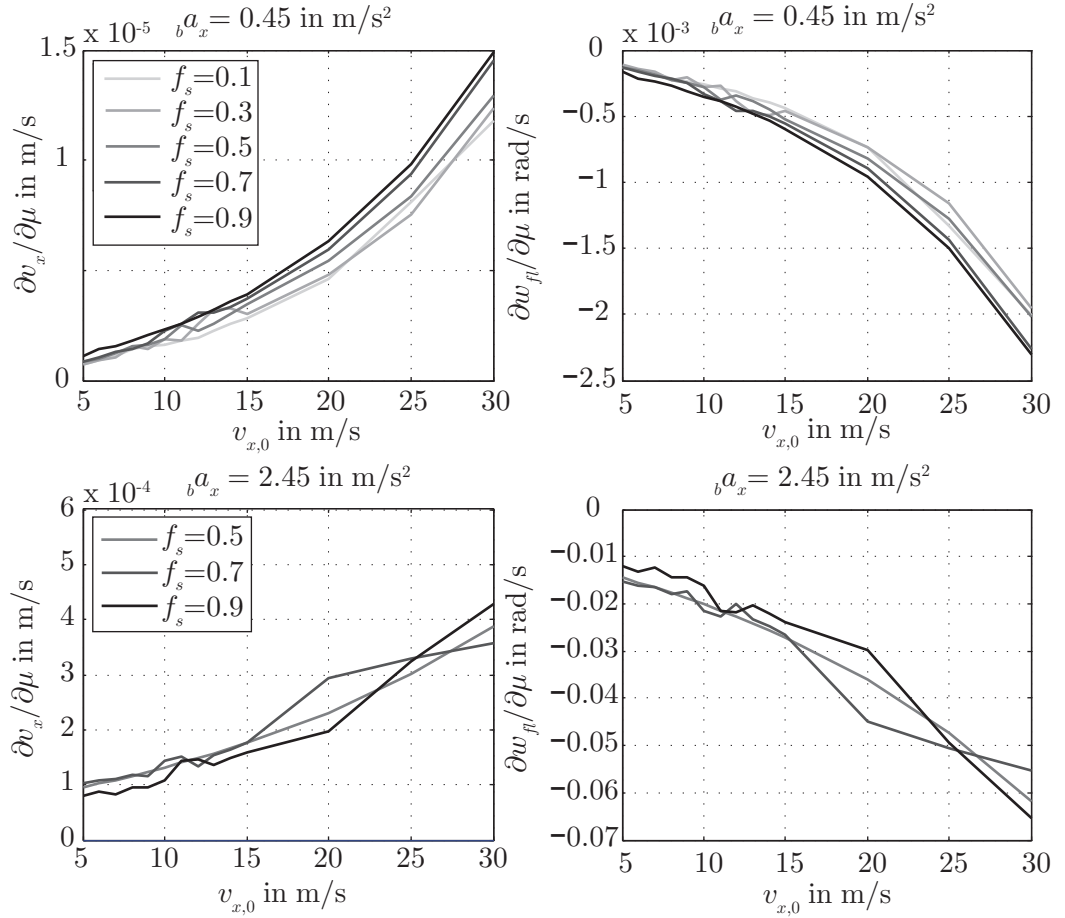


Figure 4.4.: Dependence of selected sensitivities $\partial v_x / \partial \mu$ (**left**) and $\partial \omega_{fl} / \partial \mu$ (**right**) versus the initial longitudinal velocity $v_{x,0}$ for $\mu^{\max} = 1$ for pure longitudinal acceleration of 0.45 m/s^2 (**above**) and 2.45 m/s^2 (**below**) and different scaling factors f_s within the simulation.

gorithm. Thus, it is not necessary to compensate for the influence of the longitudinal speed. However, it has to be mentioned that within each driving state region as defined in Figure 4.10, the initial longitudinal velocity $v_{x,0}$ for the manoeuvres is the same.

Comparison of sensitivities for longitudinal and lateral manoeuvres

To ensure comparable results, simulations that start with longitudinal excitation and then add lateral excitation (LQ) are compared to simulations that start the other way around (QL) at the same μ^{\max} and acceleration profiles. Both simulations are compared at specific acceleration points.

As an example, Figure 4.5 shows the comparison of two simulations at the data point where each reaches the driving state with a longitudinal acceleration of 1.2 m/s^2 and a lateral acceleration of 1.9 m/s^2 . The absolute value of the sensitivities is higher for LQ manoeuvres. This is true for all simulations. This difference between the absolute values of the sensitivities for LQ and QL manoeuvres increases with higher acceleration conditions. This indicates that the influence of the longitudinal velocity is mainly responsible for this effect. Nevertheless, the tendencies are similar, and it leads to the same conclusion that was drawn for the influence of the longitudinal speed, cf. Section 4.3.2. Thus, this does not limit the comparability of the tendencies, as the absolute value of the sensitivities is not of interest.

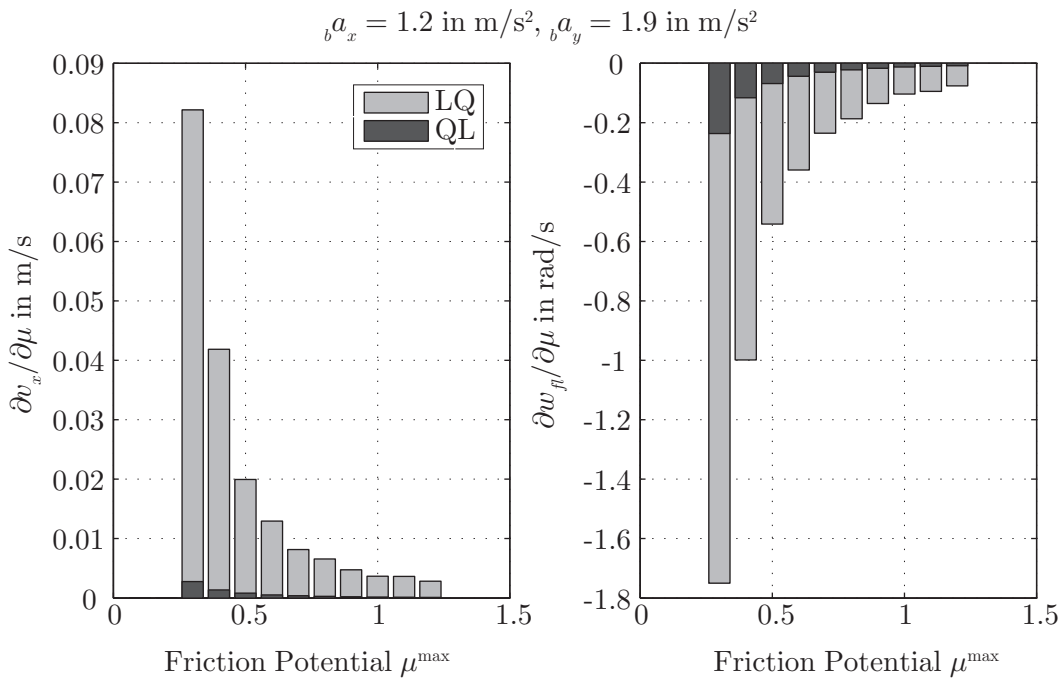


Figure 4.5.: Comparison of the selected sensitivities $\partial v_x / \partial \mu$ (left) and $\partial \omega_{fl} / \partial \mu$ (right) versus μ^{\max} shows similar behaviour for LQ and QL manoeuvres at a longitudinal acceleration of 1.2 m/s^2 and a lateral acceleration of 1.9 m/s^2 .

4.4. Normalisation of sensitivities

The state variables and their sensitivities with respect to μ^{\max} do not all have the same units and also vary in their orders of magnitude. To be able to choose the variables that

4 Sensitivity Analysis

are the most sensitive for the driving state, the influences of the different state variables within one investigated region have to be made comparable. Thus, it is necessary to normalise the resulting sensitivities in order to achieve physical equivalence. One possibility is to normalise the sensitivities $p_l(t)$ to the value of the respective state variable $z_l(t)$. As μ^{\max} itself is dimensionless, the unit of the sensitivity $\partial z_l / \partial \mu$ corresponds to the unit of the respective state variable z_l . The aforementioned sensitivity normalised to $z_l(t)$ is then dimensionless, but it does not provide the same orders of magnitude within the sensitivities of the different state variables. Thus, this method of normalisation is suitable when assessing the change in sensitivity of a state variable over different driving states, but it is not useful when comparing the sensitivity of different state variables for a specific driving state. Normalising the sensitivities to the maximum state variables (e.g. the maximum speed of the investigated vehicle) or the maximum sensitivities during the simulations would result in sensitivities within the same order of magnitude (especially the latter normalisation). Nevertheless, small sensitivities of small state variables (e.g. the vehicle's yaw rate) would appear larger than can be physically explained. This also applies for the first normalisation method mentioned above. Thus, the following approach based on kinematic relations is used in this work to ensure physical equivalence of the different state variables and their sensitivities.

4.4.1. Kinematic relation for normalisation

The longitudinal velocity v_x is used as the reference value for the other state variables in order to achieve physical equivalence within their sensitivities. As the sole variable, it is normalised to its maximum value¹ v_x^{\max} . With v_x^{\max} not depending on μ^{\max} , as every velocity can be reached within enough time even on low-friction surfaces, the normalisation of the state variable $y_1 = v_x$ is directly applicable to p_1 , as shown in Equation 4.15.

$$\bar{v}_x = \frac{v_x}{v_x^{\max}} \rightarrow \frac{\partial \bar{v}_x}{\partial \mu} = \frac{1}{v_x^{\max}} \cdot \frac{\partial v_x}{\partial \mu} \quad (4.15)$$

To make the lateral velocity v_y physical equivalent to the reference value v_x , the side slip angle characteristics for a single-track model and for small values of the side slip angle given by

$$\beta = \beta_0 + \Delta\beta = \arctan \frac{v_y}{v_x} \approx \frac{v_y}{v_x} \quad (4.16)$$

¹Reference value v_x^{\max} was taken from the technical data sheet, [AG08].

are used. The side slip angle consists of the side slip angle at small lateral accelerations close to zero (e.g. occurring when entering a curve), which follows the geometric relation

$$\beta_0 = \beta|_{b a_y \rightarrow 0} = \frac{l_r}{R} \quad (4.17)$$

with the distance l_r of the vehicle's COG to the rear axle and the curve radius R of the trajectory, [HE11, p.110]. With higher accelerations, the additional angle $\Delta\beta$ adds to β_0 . It is not a function of R , but of $b a_y$. Both the characteristic and its maximum value can be seen in Figure 4.6, which shows a characteristic measured during steady-state cornering, [fSI04]. For the maximum of β_0 , the minimum radius, i.e. the turning circle R^{\min} of the vehicle, [AG08], is used in Equation 4.17. By rearranging Equation 4.16 for

$$v_x = v_y \cdot \frac{1}{\beta_0 + \Delta\beta}, \quad (4.18)$$

and substituting the components of β with its maximum values, the normalised lateral velocity \bar{v}_y reads

$$\bar{v}_y = \frac{v_y}{\beta_0^{\max} + \Delta\beta^{\max}} \cdot \frac{1}{v_x^{\max}}. \quad (4.19)$$

Since it is assumed that $\Delta\beta^{\max}$ does not depend on μ^{\max} when not at the physical limits, the sensitivity of \bar{v}_y reads

$$\frac{\partial \bar{v}_y}{\partial \mu} = \frac{1}{\beta_0^{\max} + \Delta\beta^{\max}} \cdot \frac{1}{v_x^{\max}} \cdot \frac{\partial v_y}{\partial \mu}. \quad (4.20)$$

Physical equivalence between v_x and $b\omega_z$ is gained by normalising $b\omega_z$ and its sensitiv-

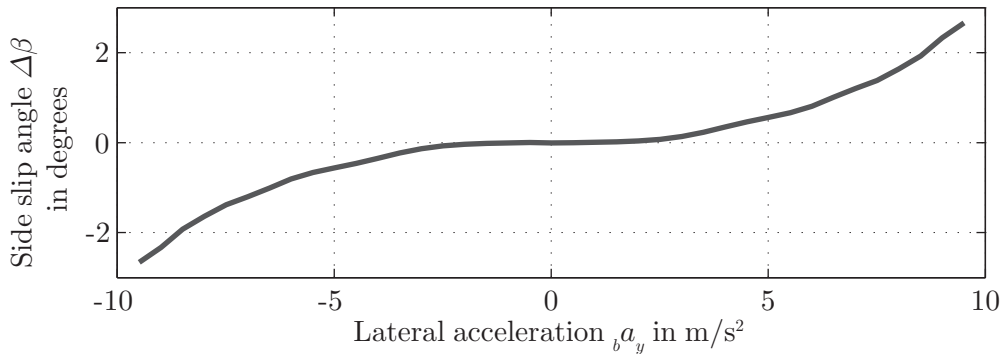


Figure 4.6.: Characteristic of side slip angle $\Delta\beta$ (not including the geometric part β_0 at $b a_y \approx 0$ compared to β) measured at steady-state circular driving with an *Audi A4 Avant 1.8 Tfsi*

4 Sensitivity Analysis

ities with the minimum turning circle R^{\min} such that

$$\bar{\omega}_z = \frac{R^{\min}}{v_x^{\max}} \cdot {}_b\omega_z \quad \text{and} \quad (4.21)$$

$$\frac{\partial \bar{\omega}_z}{\partial \mu} = \frac{R^{\min}}{v_x^{\max}} \cdot \frac{\partial {}_b\omega_z}{\partial \mu}. \quad (4.22)$$

Accordingly, the values of the four wheel angular speeds ω_i are normalised by the reference effective tire radius $r_{e,i}$. For zero longitudinal slip at the wheel, the longitudinal velocity of the wheel hub is proportional to the effective tire radius and the wheel's angular speed. Thus, the normalised $\bar{\omega}_i$ is physically equivalent to v_x , and its sensitivity reads

$$\bar{\omega}_i = \frac{\omega_i \cdot r_{r,i}}{v_x^{\max}} \quad \text{and} \quad (4.23)$$

$$\frac{\partial \bar{\omega}_i}{\partial \mu} = \frac{r_{r,i}}{v_x^{\max}} \cdot \frac{\partial \omega_i}{\partial \mu}. \quad (4.24)$$

The reference effective tire radius $r_{r,i}$ is calculated for static tire loads based on Equation 3.23. Finally, the normalised state variables and their normalised sensitivities read

$$\bar{\mathbf{z}} = \mathbf{N} \cdot \mathbf{z} \quad \text{and} \quad (4.25)$$

$$\frac{\partial \bar{\mathbf{z}}}{\partial \mu} = \mathbf{N} \cdot \frac{\partial \mathbf{z}}{\partial \mu}, \quad (4.26)$$

where the normalisation matrix \mathbf{N} is a diagonal matrix whose principal diagonal consists of the elements $\frac{1}{v_x^{\max}} \cdot \left[1 \quad \frac{1}{\left(\frac{l_r}{R^{\min}} + \Delta\beta^{\max}\right)} \quad R^{\min} \quad r_{r,fl} \quad r_{r,fr} \quad r_{r,rl} \quad r_{r,rr} \right]$.

4.5. Results and discussion of sensitivity analysis

As discussed in Section 4.1.1, the sensitivity \mathbf{p} shows the relation between the change of the state variable \mathbf{z} with respect to the change of the investigated parameter in the investigated case μ^{\max} . This means that the sign of the resulting sensitivity takes into account the relation of the changes in both \mathbf{z} and μ^{\max} for the investigated data point.

Figure 4.7 shows how the non-normalised sensitivities of all state variables change with μ^{\max} for two different longitudinal accelerations during a manoeuvre with pure longitudinal acceleration. With increasing longitudinal acceleration, the absolute value of the sensitivity increases. This is true for all of the state variables \mathbf{z} and for all simulated

μ^{\max} . It has to be mentioned that high values of ${}_b a_x$ and ${}_b a_y$ cannot be reached at low μ^{\max} . For this reason, these conditions cannot be displayed.

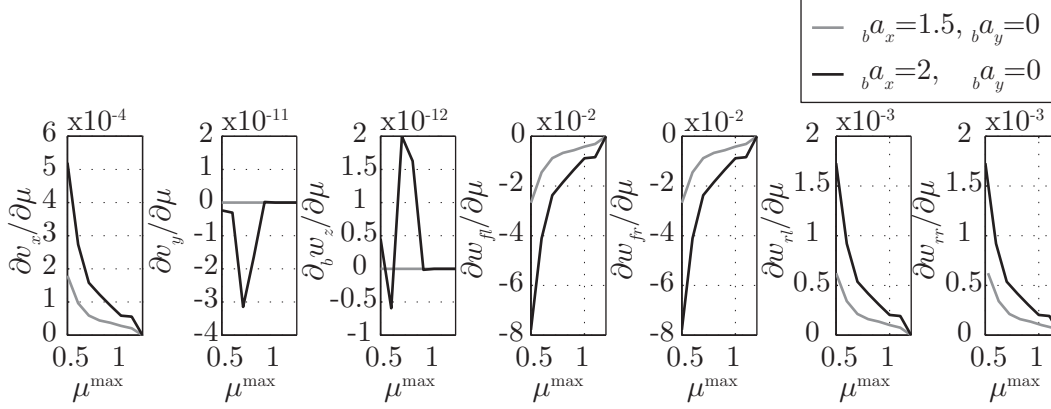


Figure 4.7.: Relation between non-normalised sensitivity of state variables and the friction potential μ^{\max} for two selected longitudinal accelerations. The units of the shown sensitivities are the same as for their respective state variable.

As expected, at all four wheels the absolute value of the sensitivities of the wheel speed is higher for low μ^{\max} and decreases with increasing μ^{\max} . This can be explained by the higher wheel's rotational accelerations at lower μ^{\max} at the same ${}_b a_x$. The absolute value of the sensitivities for the front wheels is higher than for the rear wheels. For a front-wheel drive (FWD), this can be explained by the high driving torque on the front axle and the comparably low rolling resistance torque on the rear axle. The different signs on front and rear wheels follows from the sign of the sum of torques. The sensitivity $\partial v_x / \partial \mu$ for the longitudinal speed shows the same tendency as those of the rear wheels, but the absolute value is several orders of magnitude lower. This is due to the fact that the inertia of the chassis is higher than that of the wheels, which results in a slower response to dynamic changes. This already indicates that the longitudinal velocity is not the best indicator for a change of μ^{\max} for pure longitudinal accelerations. As expected, during purely longitudinal excitation, the sensitivities of the lateral velocity $\partial v_y / \partial \mu$ and the yaw rate $\partial {}_b \omega_z / \partial \mu$ can be omitted due to the small contribution.

Figure 4.8 shows the non-normalised sensitivities of the state variables with respect to μ^{\max} for two combined longitudinal and lateral accelerations. The sensitivities for the state variables v_x , ω_{fl} , ω_{fr} , ω_{rl} and ω_{rr} show a similar behaviour as the purely longitudinal acceleration manoeuvre in Figure 4.7, although the orders of magnitude

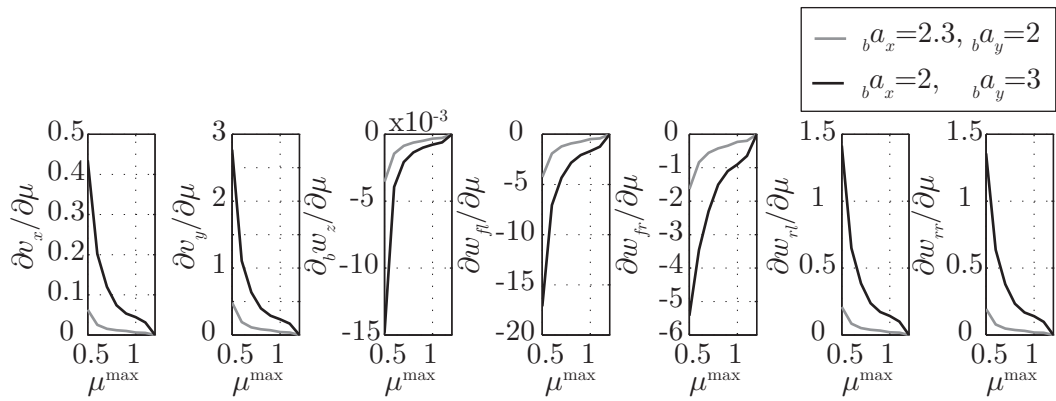


Figure 4.8.: Relation between non-normalised sensitivity of state variables and the friction potential μ^{\max} for two combined longitudinal and lateral accelerations. The units of the shown sensitivities are the same as for their respective state variable.

vary. The sensitivity of the lateral velocity $\partial v_y / \partial \mu$ shows a comparable tendency to that of the longitudinal velocity v_x , but one order of magnitude higher, despite the fact that the absolute value of v_y during cornering is generally far lower than that for v_x . Even without normalisation, this already indicates that considering v_y to estimate μ^{\max} will contribute much more than considering v_x during a manoeuvre that includes cornering. In comparison, the sensitivity $\partial_b \omega_z / \partial \mu$ is several orders of magnitude smaller and has a different sign. The yaw rate changes little with changing μ^{\max} due to the high vehicle's yaw moment of inertia, see Figure 4.9. In comparison, v_y changes significantly with μ^{\max} , as can also be seen in Figure 4.9.

4.5.1. Resulting normalised sensitivities at different driving states

Figure 4.10 shows all simulated accelerations (black lines) and the different regions (gray areas) that have been analysed. The investigated area corresponds approximately to the area that is typically traversed by a non-professional driver within the maximum physically possible area, [Weg09, p.70-71]. The black dots show all analysed data points, and the dark gray asterisks show all selected data points that are further shown and discussed in this section. It has to be mentioned that the resulting absolute values of the sensitivities depend on the initial longitudinal speed, see Section 4.3.2. Within one region, the initial longitudinal speed $v_{x,0}$ is the same. The absolute values of the sensitivities can be directly compared within one region, but not across regions.

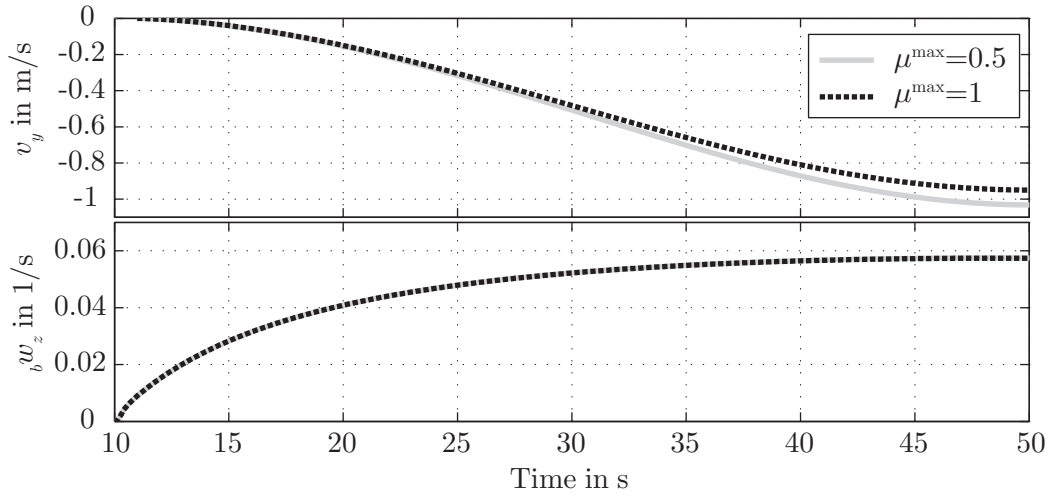


Figure 4.9.: Lateral velocity v_y and yaw rate ${}_b\omega_z$ versus time for two different μ^{\max} during the simulated manoeuvres. The maximum value for ${}_b a_y$ for both simulations was 4 m/s^2 . In the case of ${}_b\omega_z$, the two different characteristics can barely be distinguished.

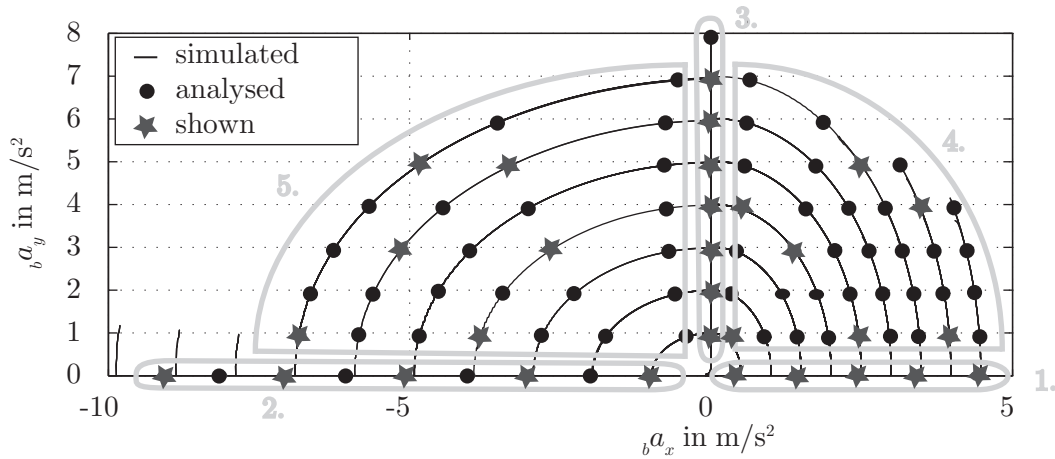


Figure 4.10.: Parameter space of simulated driving states (black lines), i.e. horizontal chassis accelerations at the vehicle's COG, and the classification into five driving state regions (gray areas). Black dots show all the data points that were analysed, and gray asterisks show the selected data points that are discussed in detail in Figures 4.11 to 4.15. It is assumed that the vehicle behaviour is similar for positive and negative lateral acceleration ${}_b a_y$ (i.e. right and left turn).

Region 1 (accelerating)

The first region examined comprises the area with positive longitudinal accelerations. Figure 4.11 shows the characteristics of the normalised sensitivities versus μ^{\max} for 5 different longitudinal accelerations. The wheel speeds ω_{fl} and ω_{fr} of the driven wheels show the highest sensitivity to μ^{\max} by a considerable margin. As expected, the absolute values of the sensitivities increase with higher dynamic excitation. For a longitudinal acceleration of about 0.4 m/s^2 , the change of sensitivity versus μ^{\max} is very small for values of μ^{\max} that are higher than 0.4. This indicates that at these low longitudinal accelerations, it will not be possible to provide a reliable estimate of μ^{\max} for $\mu^{\max} > 0.4$ using solely the vehicle-dynamics-based method presented in this work. Nevertheless, at a longitudinal excitation of about 1.4 m/s^2 , the sensitivities of the wheel speeds already show a distinguishable characteristic up to a value of μ^{\max} of 0.9. The wheel speeds ω_{rl} and ω_{rr} of the non-driven wheels also show a small dependence on μ^{\max} , especially for smaller values of μ^{\max} . Their sensitivities also increase with higher dynamic excitation. In contrast, the dependence of the longitudinal velocity is small for all μ^{\max} and dynamic excitations. This can be explained by the higher inertia and thus the slower response of the chassis than the wheels to a change in μ^{\max} . Thus, v_x is not likely to contribute to an estimate of μ^{\max} . Due to the high dependence of the sensitivities of the driven wheels on μ^{\max} , an all-wheel drive (AWD) configuration was also simulated with a torque distribution of 50% each on the front and rear axles, see Section 4.5.2.

Region 2 (braking)

The resulting sensitivities of the area of negative ${}_b a_x$ (*Region 2*) are shown in Figure 4.12, which shows the five selected data points of ${}_b a_x$. Since, in contrast to the front-wheel drive configuration in *Region 1*, wheel torque is now applied to all four wheels, the rear wheel speeds also show a higher sensitivity to μ^{\max} . The brake distribution is set to 60 % on the front axle and 40 % on the rear axle for these simulations. The sensitivities of the wheel speeds show a very high dependence on μ^{\max} and on the longitudinal acceleration. The tendencies are similar for all acceleration points, but the absolute values vary as the wheel slips, and thus the longitudinal forces depending on μ^{\max} vary. Starting at about -2 m/s^2 , the wheel speeds already show significant sensitivities for μ^{\max} lower than ≈ 1 at the simulated initial $v_{x,0}$. This indicates that starting at this longitudinal acceleration, a distinction of these road or tire conditions may be feasible. Similar to *Region 1*, the sensitivity of $v_{x,0}$ shows a negligible dependence on μ^{\max} . As it is a pure longitudinal manoeuvre, the sensitivities for both the two front and the rear wheel speeds

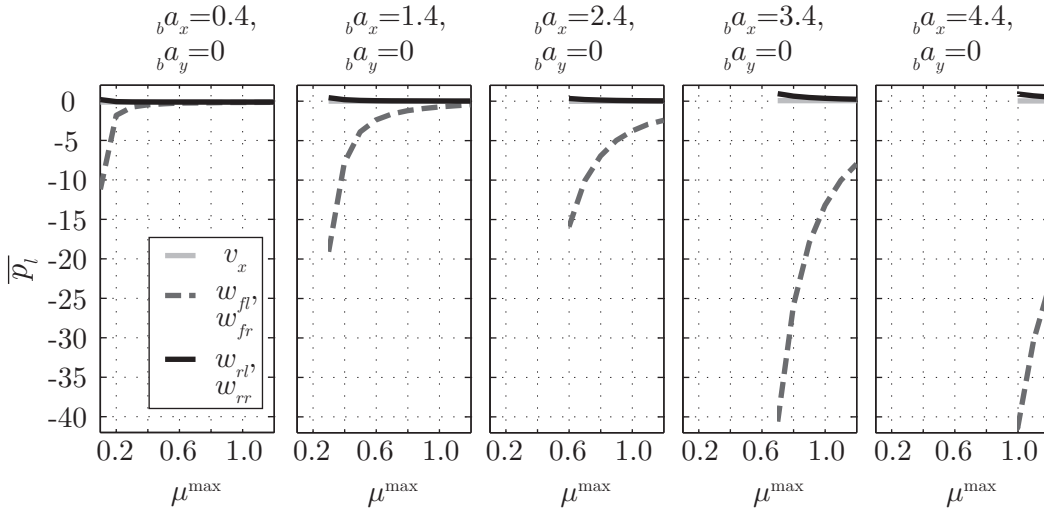


Figure 4.11.: Normalised sensitivities for all state variables except v_y and $b\omega_z$, which are zero within this region, for selected acceleration data points in *Region 1* (positive longitudinal excitation). Note: High values of $b a_x$ and $b a_y$ cannot be reached at low μ^{\max} , thus not all μ^{\max} are shown for all data points.

are congruent. For most of the longitudinal acceleration data points, the front wheel speeds show a higher sensitivity to μ^{\max} due to the higher braking torque applied on the front axle. At a longitudinal acceleration of about -6 m/s^2 and higher, the sensitivities of the rear wheels exceed those of the front wheels for the simulated initial $v_{x,0}$. Due to the higher wheel load on the front axle during braking, the rear wheels are relieved, and w_i increases more rapidly than on the front axle. The high dependency of the sensitivities of the wheel speeds on μ^{\max} and the applied brake torque on the front and rear axles is comparable to the results from the comparison of AWD and FWD in *Region 1*. Thus, a theoretical configuration with brake torque only applied to the front wheels was also simulated, see Section 4.5.3.

Region 3 (pure cornering)

Similar to the results from *Region 1* and *Region 2*, the wheel speeds show the highest sensitivity for driving states with purely lateral excitation in *Region 3*. as shown in Figure 4.13. A left turn is made during this manoeuvre. With increasing lateral accelerations, the tire load $F_{z,fl}$ decreases, which at first causes the absolute value of the sensitivity of the wheel speed ω_{fl} to increase faster compared to that of ω_{fr} . At a certain point, the sensitivity of ω_{fr} exceeds that of ω_{fl} , due to the influence of μ^{\max} within the

4 Sensitivity Analysis

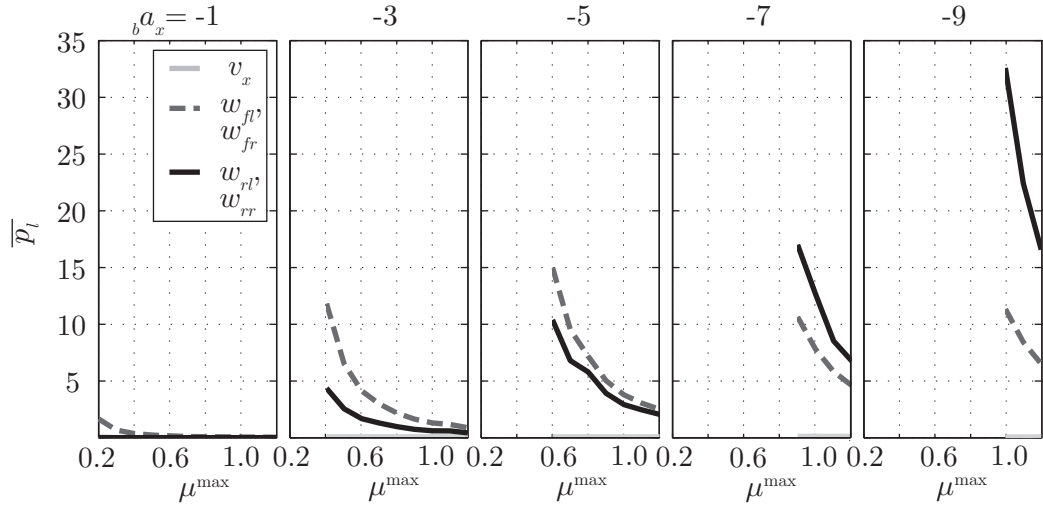


Figure 4.12.: Normalised sensitivities for all state variables except v_y and $b\omega_z$, which are zero within this region, for selected acceleration data points in *Region 2* (negative longitudinal excitation). The value for v_x is close to zero for all simulations.

transmitted tire forces, which differ at the inner (index fl) and outer wheel (index fr) during cornering. With higher dynamic excitation, the sensitivities of the front wheels increase by several orders of magnitude, from about 10^{-1} at 1 m/s^2 to 10^2 at 7 m/s^2 . Again, the sensitivities of the chassis are small compared to those of the wheel speeds. Especially the sensitivities of the longitudinal speed v_x and the yaw rate $b\omega_z$ can be omitted. Though smaller than the sensitivities of the wheel speeds, the lateral velocity v_y shows a dependence on μ^{\max} . Starting at $b a_y \approx -1 \text{ m/s}^2$, the wheel speeds show significant sensitivities for μ^{\max} lower than ≈ 0.5 for the simulated initial value of v_x . At $b a_y \approx -2 \text{ m/s}^2$, the sensitivity of the front inner wheel speed ω_{fl} indicates that a distinction of μ^{\max} until ≈ 1 might be possible.

Region 4 (combined cornering and acceleration)

The results for *Region 4* (positive longitudinal and lateral excitation) in Figure 4.14 show the sensitivities for all state variables for selected data points of $b a_x$ and $b a_y$. The bottom row of diagrams in Figure 4.14 shows data points of $b a_y = 1 \text{ m/s}^2$ with increasing $b a_x$ from left to right. Again, the front wheel speeds show the highest sensitivity to μ^{\max} . The higher the $b a_x$, the lower the sensitivity of the rear wheel speeds in comparison to the front wheel speeds. The sensitivities p_{v_x} and $p_{b\omega_z}$ are again negligible. The sensitivity p_{v_y} is small but noticeable. In the middle row of diagrams in Figure 4.14, $b a_y$ between

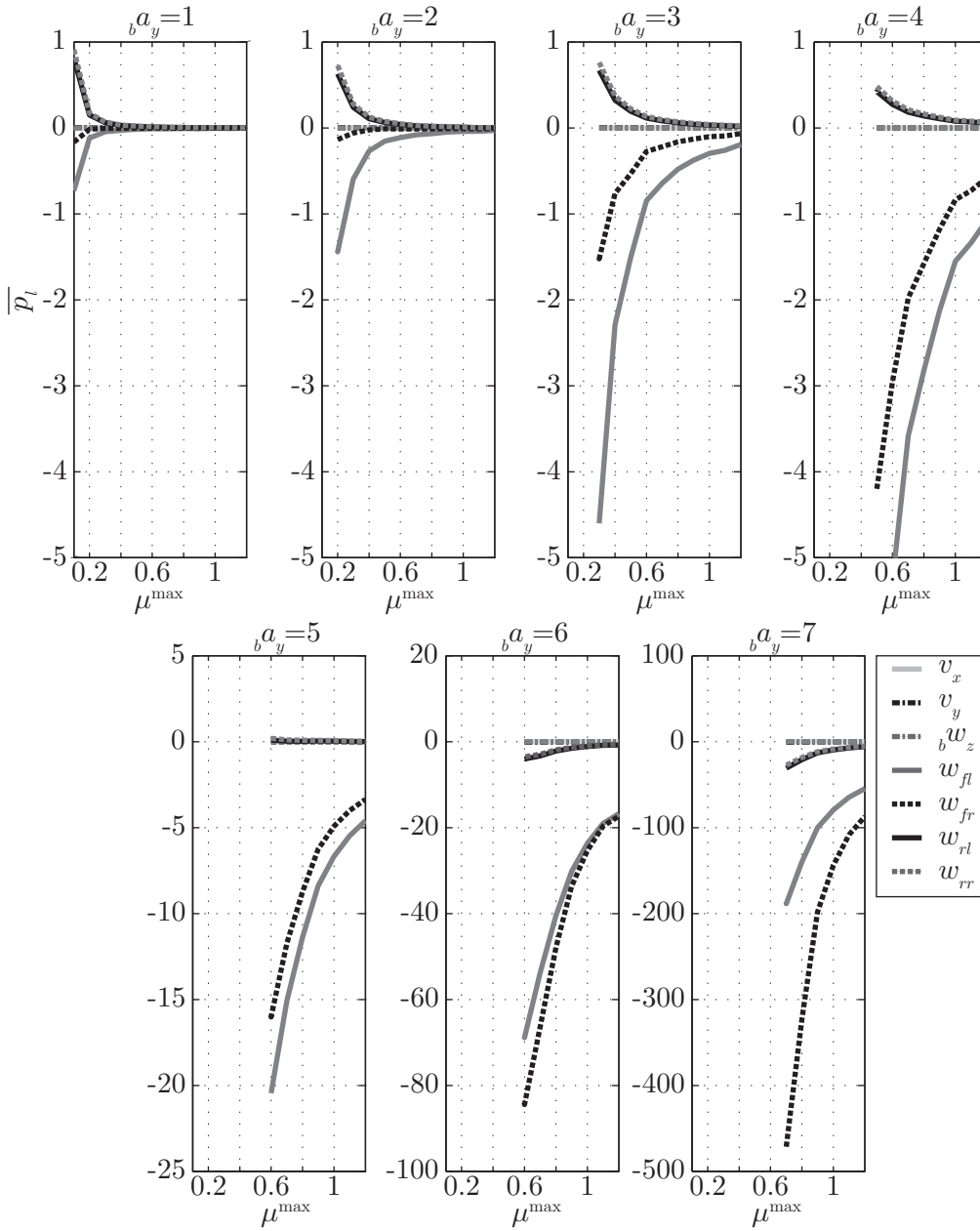


Figure 4.13.: Normalised sensitivities for all state variables for selected acceleration data points in *Region 3* (lateral excitation). Sensitivities for v_x , v_y and $b\omega_z$ are close to zero. Note: high longitudinal accelerations can only be achieved with high μ^{\max} , thus not all μ^{\max} are shown for all data points.

3 and 4 m/s^2 are shown for longitudinal accelerations increasing from left to right. Although the absolute values of the sensitivities are several orders of magnitude higher,

4 Sensitivity Analysis

the tendency is similar to the results for a lateral acceleration of 1 m/s^2 . The same factor accounts for the results presented in the upper row of diagrams in Figure 4.14, which comprises lateral accelerations between 5 and 6 m/s^2 . Here again, the longitudinal acceleration increases from the left to the right side in Figure 4.14. It has to be mentioned that the driving states of ${}_b a_x = 0.6$ and ${}_b a_y = 6$ (upper left) and ${}_b a_x = 3$ and ${}_b a_y = 5$ (upper right) were only reached in a stable way at $\mu^{\max} = 1.1$ and $\mu^{\max} = 1.2$, so there is only one data point, rather than a line, as in the other diagrams. With increasing ${}_b a_y$ at low ${}_b a_x$, the sensitivity of wheel speed ω_{fr} (outer wheel in turn) is bigger than that of the inner wheel speed ω_{fl} . The higher the longitudinal acceleration, the higher the influence of the inner wheel speed ω_{fl} . This is due to the decreasing tire load on this wheel during cornering, which leads to an increasing wheel speed in comparison to a higher-loaded wheel when a driving torque is applied.

Region 5 (combined cornering and braking)

Figure 4.15 shows the standardized sensitivities for *Region 5*, which comprises negative longitudinal and lateral excitation. Similar to Figure 4.14, ${}_b a_x$ decreases from the left to the right side, whereas ${}_b a_y$ increases from the bottom row up. Unlike in Figure 4.14, the order of magnitude of the sensitivities does not depend so much on ${}_b a_y$, but rather on ${}_b a_x$. One possibility is that the ${}_b a_x$ achieved during braking are two times higher than during accelerating, see Table 4.1.

4.5.2. Sensitivities for all-wheel-driven vehicle

In addition to the front-wheel drive (FWD), an all-wheel drive (AWD) with a wheel torque distribution of 50 % on the front and the rear axle was simulated. The simulation used the same manoeuvre and the same initial $v_{x,0}$ as the simulation of the front-wheel drive in *Region 1*. As expected, the absolute sensitivities for the AWD configuration shown in Figure 4.16 are smaller than those of the FWD configuration, cf. Figure 4.11. This can be explained by the fact that the wheel slips on the front axle are lower for the AWD configuration. Thus, it is expected that it is more difficult to estimate μ^{\max} for an AWD. This is consistent with results from previous investigations on AWD from *Holzinger*, [Hol92, p.86]. However, other than for the FWD configuration, the sensitivities of the rear wheels are higher and have a different sign. This is due to the positive driving torque applied in the AWD configuration, whereas for FWD the only torque present is the comparably small and negative rolling resistance torque.

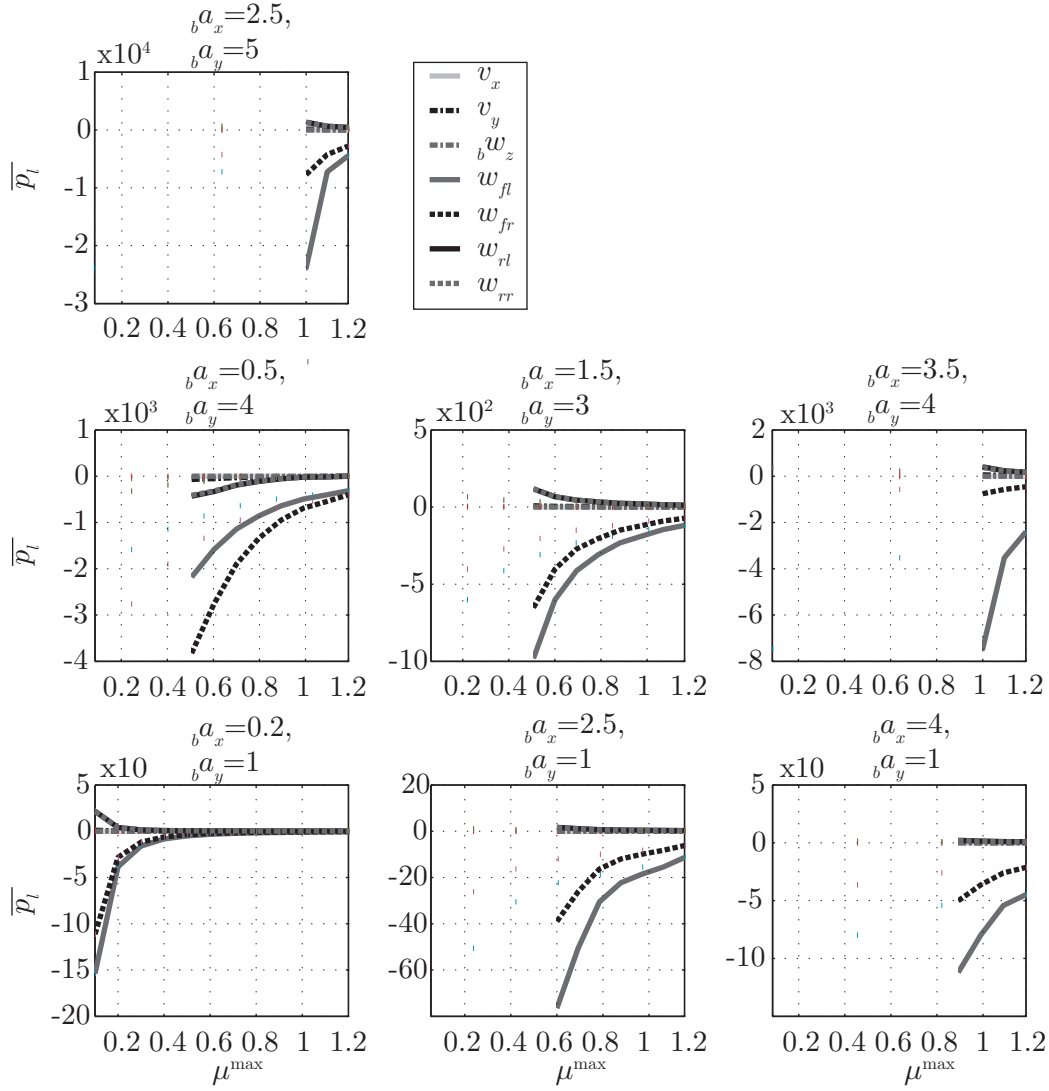


Figure 4.14.: Normalised sensitivities for all state variables for selected acceleration data points in *Region 4* (positive longitudinal and lateral excitation). Sensitivities for v_x , v_y and $b\omega_z$ are close to zero.

4.5.3. Sensitivities for front-braked vehicle (theoretical)

To investigate the influence of the brake torque distribution between front and rear axle, the extreme and theoretical case of only front braking (100 % brake torque on front axle) has been investigated. The simulation reproduced same manoeuvres and the same initial $v_{x,0}$ as the simulation of the conventional brake system in *Region 2*. For the conventional braking system (as shown in Figure 4.12), the curves for the wheel speeds on the front

4 Sensitivity Analysis

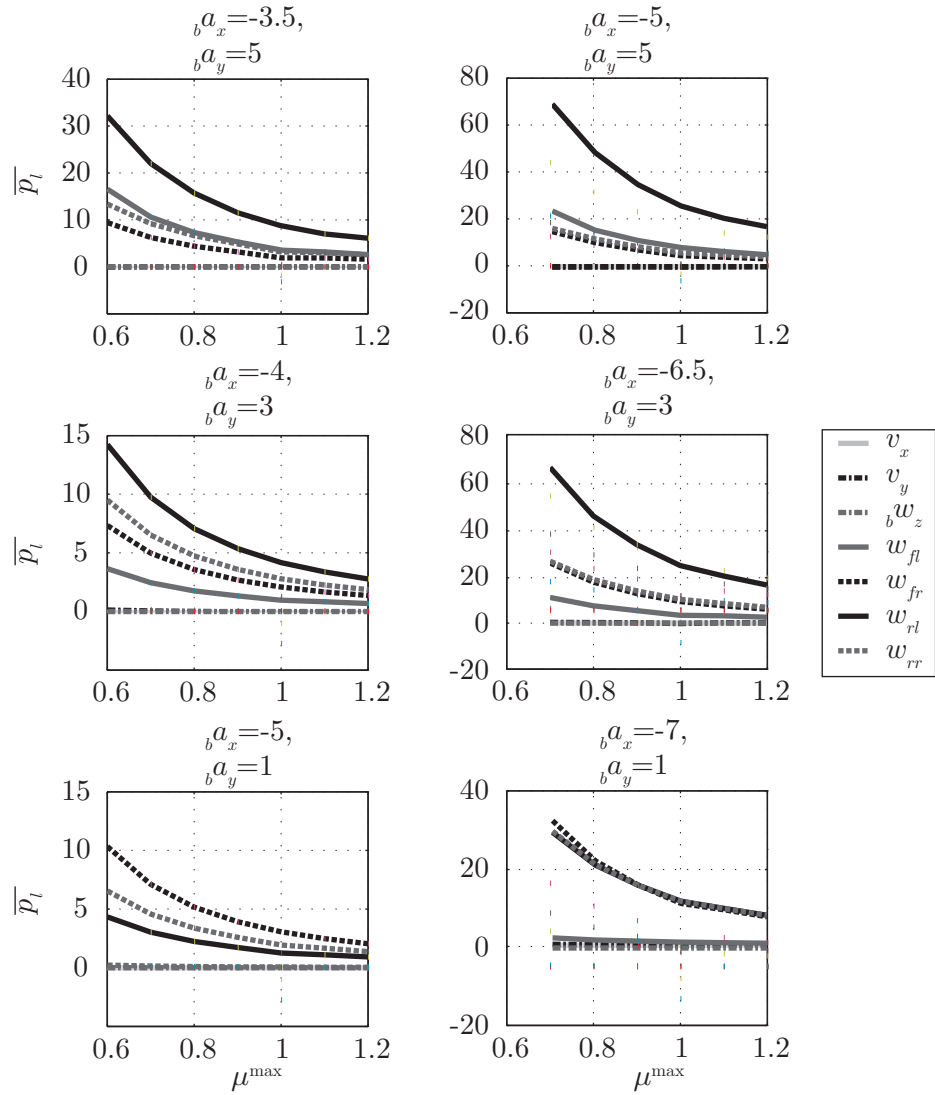


Figure 4.15.: Normalised sensitivities for all state variables for selected acceleration data points in *Region 5* (negative longitudinal and lateral excitation). Due to a numerical problem at all simulations of $\mu^{\max} = 1$ during combined braking and cornering, the normalised sensitivities have been interpolated in this Figure for $\mu^{\max} = 1$.

and rear axles have a similar tendency; only the absolute value differs in dependence on ${}_b a_x$ due to the set braking torque distribution. Figure 4.17 shows the case of 100 % braking torque on the front axle. The brake torque is controlled such that the same ${}_b a_x$ is reached as for the conventional braking system configuration. The tendency of the front wheels is comparable for both braking systems. Nevertheless, the absolute values of the

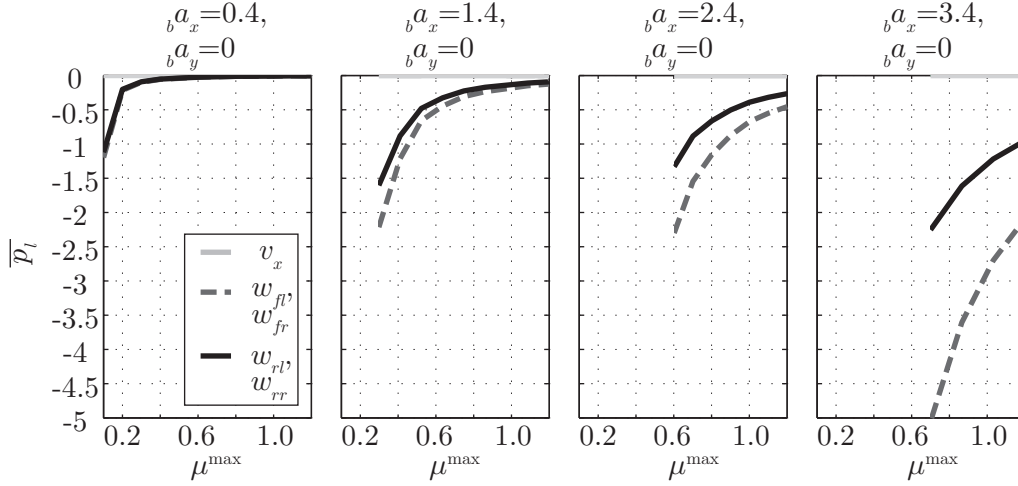


Figure 4.16.: Normalised sensitivities for all state variables except v_y and $b\omega_z$, which are zero within this region, for selected acceleration data points in *Region 1* (positive longitudinal excitation) for an AWD (torque distribution front and rear 50 % each)

front wheel speed's sensitivities are higher. This indicates that estimating μ^{\max} based on the front wheels would work better for this case than for the conventional braking system. This also highlights the results of the influence of the wheel's torque from the comparison of FWD and AWD for positive $b a_x$. The sensitivities of the rear wheels are very small and do not change much versus the simulated areas of μ^{\max} , as there is no braking torque present.

4.6. Choice of sensitive parameters for the estimation observer

This investigation clearly shows that the wheels are the most qualified sensors for friction estimation among the investigated variables, and thus are assumed to be quite qualified for friction estimation in general. Across all investigated areas shown in Figure 4.10, the wheel speeds show the highest sensitivity to μ^{\max} . Although much smaller, the lateral velocity v_y also shows a dependence on μ^{\max} in regions with lateral excitation. The sensitivity of β can be calculated using the already known sensitivities $p_{v_x} = \partial v_x / \partial \mu$ and $p_{v_y} = \partial v_y / \partial \mu$ using Equation 4.11. As $v_y / v_x^2 \cdot p_{v_x} \ll 1 / v_x \cdot p_{v_x}$, the first term can be omitted. When v_x is within the range of 0 to $v_x^{\max} = 62.5$ m/s, [AG08], the maximum value of $p_\beta \approx 1 / v_x \cdot p_{v_y}$ is within the order of magnitude of p_{v_y} , and the minimum value is about two orders of magnitudes smaller. Thus, other than its maximum value, the order of magnitude of p_β is below that of p_{v_y} . Nevertheless, as β is more likely to be

4 Sensitivity Analysis

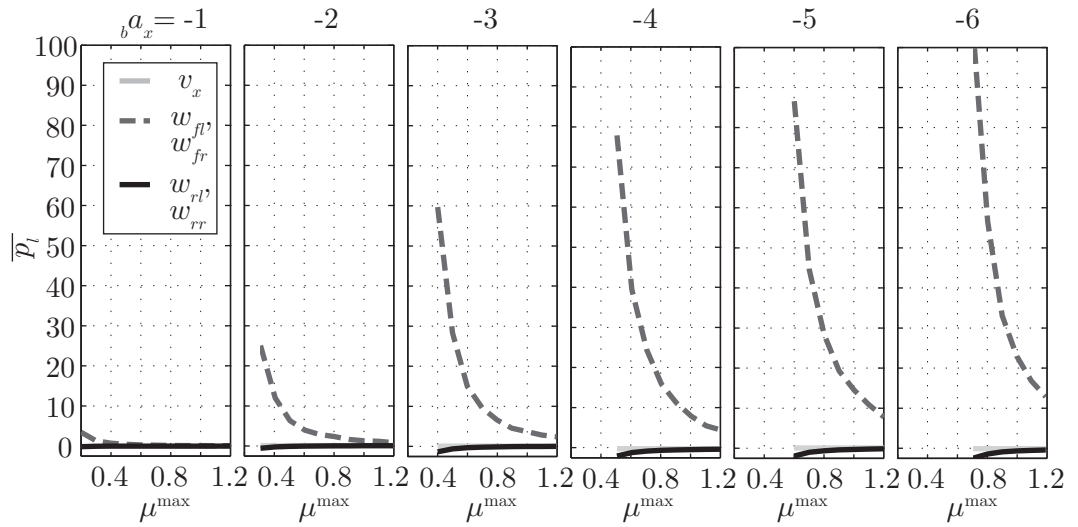


Figure 4.17.: Normalised sensitivities for all state variables except v_y and $b\omega_z$, which are zero within this region, for selected acceleration data points in *Region 2* (negative longitudinal excitation) for 100 % braking torque on the front axle

available on a future vehicle CAN than v_y due to its relevance for VDC, it is included in Table 4.2. Nevertheless, the influence of v_y and β on μ^{\max} is low compared to that of the wheel speeds. In addition, these influences have to be estimated for series application, which may compromise the robustness of an estimation algorithm of μ^{\max} . In contrast, wheel speed sensors are standard in vehicles equipped with anti-lock braking systems (ABS) or electronic stability control (ESC). Thus, from the state variables presented in Table 4.2, only the wheel rotational speeds w_i were selected for the observation strategy in Section 5.

Table 4.2.: State variables sensitive to μ^{\max} to be observed for the different driving states.
 Ratings: ++ ... *high sensitivity*, + ... *medium sensitivity*, o ... *low sensitivity*,
 - ... *lowest sensitivity (assumed negligible)*.

	<i>Region 1</i>	<i>Region 2</i>	<i>Region 3</i>	<i>Region 4</i>	<i>Region 5</i>
v_x	-	-	-	-	-
v_y	-	-	o	o	o
β	-	-	o	o	o
$b\omega_z$	-	-	-	-	-
ω_{fl}	++	++	++	++	++
ω_{fr}	++	++	++	++	++
ω_{rl}	+	++	++	++	++
ω_{rr}	+	++	++	++	++

5. Tire/road friction estimator

This chapter outlines the proposed method for estimating the friction potential based on sensor signals of a vehicle equipped with ESC. A brief introduction to recursive Bayesian state estimation (and especially the particle filter) is provided first. Both methods have proven to be suitable for state estimation problems and can deal with the presence of uncertain measurements and measurement noise. The system model to be observed, which was chosen based on the results of Section 4, is described. The advantages and disadvantages of both the observer and the model are discussed, with an emphasis on longitudinal tire force calculation, as its accuracy is crucial for the estimate's accuracy.

5.1. Recursive Bayesian state estimation

Estimating the friction potential based on measurements of the vehicle's states can be treated as a state estimation problem, since the friction potential is a time-varying model parameter that directly influences the vehicle's state equations. In state estimation, a state $\mathbf{x}(k)$ that is difficult or impossible to measure directly is observed via measurements of inputs and outputs, [Bau07, p.1]. This is usually accomplished within an observer that delivers an estimate $\hat{\mathbf{x}}(k)$ for the internal state based on a state model, which consists of a non-linear difference equation for $\mathbf{x}(k)$ and a non-linear measurement equation $\mathbf{z}(k)$ in the form

$$\mathbf{x}(k) = \mathbf{f}(\mathbf{x}(k-1), \mathbf{w}(k)) \quad (5.1)$$

$$\mathbf{z}(k) = \mathbf{h}(\mathbf{x}(k), \mathbf{v}(k)), \quad (5.2)$$

[Wat06, p.65], with $k = 1, \dots, N_k$ being the time step. Since the state model can only represent a simplified description of the real physical process, uncertainties are unavoidable. In addition, the necessary measurements are subject to measurement noise and model inaccuracies. These uncertainties, which are considered within Equations 5.1 and 5.2, are modelled as the process noise $\mathbf{w}(k)$ and the measurement noise $\mathbf{v}(k)$. Deviations between a real value and its measurement are subject to chance. This means that for a constant input, the outcome of the measurements will vary randomly. Rather than

a deterministic function, the model therefore has to be treated as a stochastic process characterised by its probability distributions. Both $\mathbf{w}(k)$ and $\mathbf{v}(k)$ are assumed to be independent white noises with *a priori* known probability density functions (PDF), e.g. from past measurements, [Sim06]. PDF describe the probabilistic characteristics of a variable u by giving its probability within a range $a \leq u < b$. PDF are standardised and can only comprise values between $0 \leq p(u) \leq 1$, [Wat06, p.35]. The recursive Bayesian state estimator combines both the state estimation of a model parameter given in the form of Equation 5.1 and the prior knowledge of the state variables' probabilistic characteristics using a Bayesian framework. The basis is Bayes' theorem, which enables the calculation of the conditional probability p of a state, written as $p(u|w)$. It describes the probability that an event u will occur under the condition that an event w arose prior. Bayes' theorem requires *a priori* knowledge of the probabilities $p(u)$ and $p(w)$, which describe the probability of the occurrence of the individual events u and w . In addition, the conditional probability $p(w|u)$ has to be known, which, unlike the desired conditional PDF, describes the conditional probability of an event w given the event u , [Bau07, p.21]. Thus, $p(u|w)$ is finally given by

$$p(u|w) = \frac{p(w|u) \cdot p(u)}{p(w)}. \quad (5.3)$$

5.1.1. The recursive Bayesian state estimator

The recursive Bayesian state estimator applies Bayes' theorem, see Equation 5.3, to the state model given in Equations 5.1 and 5.2. According to *Simon*, [Sim06], the two main steps to be solved for each time step k are:

1. Prediction step:

The *a priori* PDF of the current state $\mathbf{x}(k)$ is calculated using the Chapman-Kolmogorov equation given by

$$p(\mathbf{x}(k)|\mathbf{z}(k-1)) = \int p(\mathbf{x}(k)|\mathbf{x}(k-1)) \cdot p(\mathbf{x}(k-1)|\mathbf{z}(k-1)) \, d\mathbf{x}(k-1). \quad (5.4)$$

The term $p(\mathbf{x}(k)|\mathbf{x}(k-1))$ is known when both the state model equation for $\mathbf{f}(k)$ and the PDF of the process noise $\mathbf{w}(k)$ are known. From time step $k \geq 2$, the second term $p(\mathbf{x}(k-1)|\mathbf{z}(k-1))$ is known from the update step of the last time step. For $k = 1$, an initial value $p(\mathbf{x}(0)|\mathbf{z}(0)) = p(\mathbf{x}(0))$ has to be assumed based on the PDF of its initial state $p(\mathbf{x}(0))$.

2. Update step:

The *a posteriori* PDF is given by

$$p(\mathbf{x}(k)|\mathbf{z}(k)) = \frac{p(\mathbf{z}(k)|\mathbf{x}(k)) \cdot p(\mathbf{x}(k)|\mathbf{z}(k-1))}{\int p(\mathbf{z}(k)|\mathbf{x}(k)) \cdot p(\mathbf{x}(k)|\mathbf{z}(k-1)) \, d\mathbf{x}(k)}. \quad (5.5)$$

The term $p(\mathbf{z}(k)|\mathbf{x}(k))$ in Equation 5.5, which is called the measurement likelihood function, [Wat06, p.70], can be calculated when both the measurement equation $\mathbf{h}(k)$ and the PDF of the measurement noise $\mathbf{v}(k)$ are known. Assuming that the measurement noise is Gaussian, the likelihood $p(\mathbf{z}(k)|\mathbf{x}(k))$ is proportional to a multivariate Gaussian distribution given by

$$p(\mathbf{z}(k)|\mathbf{x}(k)) \propto \frac{1}{(2\pi)^{\frac{n}{2}} \cdot |\mathbf{S}|^{\frac{1}{2}}} e^{-\frac{1}{2}(\mathbf{z}(k)-\mathbf{h}(\mathbf{x}(k)))^T \mathbf{S}^{-1} (\mathbf{z}(k)-\mathbf{h}(\mathbf{x}(k)))}, \quad (5.6)$$

for an n -dimensional measurement equation $\mathbf{z}(k)$ with measurement noise $\mathbf{v}(k) \sim \mathcal{N}(0, \mathbf{S})$, wherein \mathbf{S} denotes the covariance matrix of the measurement noise, [Sim06]. Only for some cases is there an analytical solution for Equations 5.4 and 5.5. In the special case of linear functions of $\mathbf{f}(k)$ and $\mathbf{h}(k)$, and when $\mathbf{v}(k)$ and $\mathbf{w}(k)$ are additive, independent and Gaussian, the solution of the recursive Bayesian state estimator is the Kalman filter, [Sim06], which has also been proposed for friction potential estimation in several publications, see Section 2.2.2. A further development of the recursive Bayesian state estimator is the particle filter that is presented in Section 5.2. An adapted form of a particle filter was applied by Ray, [Ray97], see Section 2.2.2 for the observed variables and Section 5.2 for the particle filter adaptation used.

5.2. Particle filtering

According to Simon, the particle filter originated from a numerical implementation of the recursive Bayesian state estimator, [Sim06]. It is a non-linear state estimator that, unlike an extended Kalman Filter, for example, does not need to linearize the non-linear state equations at the working point for each time step before it can be solved, [Sim06]. The recursive Bayesian state estimator considers only one initial state vector $\mathbf{x}(k)$ that is to be estimated and that is given with its initial PDF $p(\mathbf{x}(0))$, see Section 5.1.1. In contrast, the particle filter considers $h = 1, \dots, N$ particles for each of the l initial state vectors $\mathbf{x}_h^+(0)$ that are generated based on the initial PDF $p(\mathbf{x}(0))$ of each state vector \mathbf{x} . These particles are then re-sampled based on the relative likelihood of each of the N different particles in order to obtain the most likely states. One of the shortcomings of

particle filtering compared to Kalman filtering, for example, is the computational effort, which depends on the number N of the particles that have to be dealt with at every time step k .

The equations that describe the particle filter are given below. A more detailed derivation of the particle filter's equation is given by *Simon*, [Sim06], and a very descriptive application (although not related to friction potential estimation) is shown in *Watzenig*, [Wat06, p.65-75]. Applied to the non-linear state model given in Equations 5.1 and 5.2, the steps to be solved within a particle filter for each state variable $x_l(k)$ at each time step k according to *Simon*, [Sim06], read:

1. Time propagation step:

The *a priori* particles $\mathbf{x}_h^-(k)$ are calculated based on the l -th state model equation f_l with the particles $\mathbf{x}_h^+(k-1)$ from the previous time step $k-1$ and the process noise $\mathbf{w}_h(k-1)$ by

$$\mathbf{x}_h^-(k) = f(\mathbf{x}_h^+(k-1), \mathbf{w}_h(k-1)). \quad (5.7)$$

For $k=1$, the first N particles are randomly generated based on the PDF $p(\mathbf{x}_l(0))$.

2. Relative likelihood:

The relative likelihood \mathbf{q}_h is computed based on the measurement equation $\mathbf{h}(\mathbf{x}_h^-(k))$ and the PDF of $\mathbf{v}_h(k)$. In the case of Gaussian noise, Equation 5.6 applies. It has to be noted that Equation 5.6 does not give a direct relation, but only a proportional one (see \propto in Equation 5.6 where $=$ would be expected). Nevertheless, if it is applied to all N particles, the relative likelihood of the states is equal to that of its particles, [Sim06],

3. Normalising relative likelihood:

To ensure that the sum of the likelihoods is equal to one, \mathbf{q}_h are normalised by

$$\bar{\mathbf{q}}_h = \frac{\mathbf{q}_h}{\sum_{h=1}^N \mathbf{q}_h}. \quad (5.8)$$

The next step, the re-sampling step, is skipped in the approach proposed by *Ray*, [Ray97], who calculates the most likely value of $\hat{\mathbf{x}}(k)$ based on the normalised relative likelihood for each particle by $\sum_{h=1}^N \mathbf{x}_h^-(k) \cdot \bar{\mathbf{q}}_h$.

4. Re-sampling step:

As some state vectors have a small relative likelihood, they do not contribute significantly to an estimate, but still require computational effort, [DGA00]. This

is counteracted by the re-sampling step, where a set of *a posteriori* particles $\mathbf{x}_h^+(k)$ is randomly generated based on the relative likelihood $\bar{\mathbf{q}}_h$ of the h states vectors. For a graphic representation of how the particles are moved during one time step, see Figure 5.1.

In the re-sampling step, different strategies can be applied to randomly generate a new set of samples $\mathbf{x}_h^+(k)$. Within this work, the re-sampling strategy proposed by *Simon* is used, [Sim06]. At every time step k , the following procedure has to be applied. First, for every particle N , a random number r is chosen that is uniformly distributed between $0 \leq r \leq 1$. Next, starting with the first particle $h = 1$, the relative likelihoods $\bar{\mathbf{q}}_h(k)$ are accumulated until the $\sum_{h=1}^m \bar{\mathbf{q}}_h(k) \geq r$. The new particle $x_1^+(k)$ is now set to $x_m^-(k)$. This is done N times at each time step k until all particles $\mathbf{x}_h^+(k)$ have been assigned. In the theoretical case of $N = \infty$, the PDF of $\mathbf{x}_h^+(k)$ is equal to the PDF $p(\mathbf{z}(k)|\mathbf{x}(k))$. It has to be mentioned that other re-sampling strategies exist that might be more efficient in terms of computational effort for this application. After the re-sampling step, any statistical measure (e.g. mean or covariance) can be computed for the current time step k with the *a posteriori* particles. The N particles are already distributed according to the PDF $p(\mathbf{x}(k)|\mathbf{z}(k))$. For friction potential estimation, the most likely state of $\hat{\mathbf{x}}(k)$ at every time step k , which is of interest, is given by its expected value $E(\mathbf{x}(k)|\mathbf{z}(k))$, which reads

$$\hat{\mathbf{x}}(k) = E(\mathbf{x}(k)|\mathbf{z}(k)) = \frac{1}{N} \sum_{h=1}^N \mathbf{x}_h^+(k), \quad (5.9)$$

[Sim06]. Figure 5.1 shows a graphic representation of the steps of the particle filter. It can be seen that at time step k , the N particles are distributed based on the state's PDF $p(\mathbf{x}(k-1))$ from the last time step $k-1$. After calculating the relative likelihoods $\bar{\mathbf{q}}_h$ based on measurements and a given distribution $p(\mathbf{z}(k)|\mathbf{x}(k))$, the re-sampling step is conducted. The again N new particles $\mathbf{x}_h^+(k)$ now move toward $p(\mathbf{z}(k)|\mathbf{x}(k))$, as can be seen by comparing the gray line in Figure 5.1a and the gray particles in Figure 5.1b). As these particles are randomly generated, a few particles also occur in regions with a low probability. This ensures that the algorithm is also able to detect changes in the vehicle state $\mathbf{x}(k)$ from one time step to another. Nevertheless, how fast the particle filter can converge depends on how close the measurement distribution is to the prior distribution.

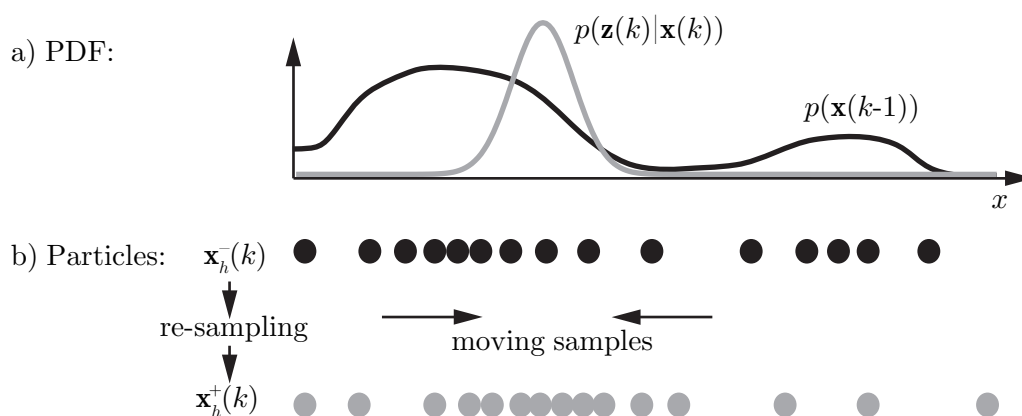


Figure 5.1.: a) Probability density functions (PDF) of the initial state $p(\mathbf{x}(k-1))$ in black and the measurement likelihood $p(\mathbf{z}(k)|\mathbf{x}(k))$ in gray, b) Particles $\mathbf{x}_h^-(k)$ distributed based on $p(\mathbf{x}(k-1))$ before re-sampling and new particles $\mathbf{x}_h^+(k)$ randomly generated during re-sampling based on $\bar{\mathbf{q}}_h$, which depends on $p(\mathbf{z}(k)|\mathbf{x}(k))$. Graphic representation based on *Watznig*, [Wat06, p.68, 71].

5.3. Choice of observer model

The following sections describe the application of the theoretical considerations on state estimation from Sections 5.1 and 5.2 on the estimation of the friction potential. As a first step, a comparison is given of the state of the art on estimators for the friction potential that are based on observers within the Bayesian framework. In a second step, both a suitable state estimation method and a suitable model to be observed are selected based on the results of the sensitivity analysis (cf. Section 4).

In existing works, observers within the Bayesian framework have already been successfully implemented for non-series application and have shown promising results for certain driving states (e.g. braking, cornering) or certain road conditions (e.g. only road surfaces with low friction potential). An overview is given in Section 2.2.2. In particular, the approach used by *Ray*, [Ray97], which can be described as a particle filter without the re-sampling step, has attracted attention due to its ability to deal with non-linear systems while still having the advantages of treating state models under uncertain measurements (e.g. as with a Kalman filter). Within *Ray*'s proposed approach, see also Section 2.2.2, the tire forces are estimated using an extended Kalman filter. These estimated tire forces are then treated as the measurement input for the particle filter, in which μ^{\max} is then estimated, [Ray97]. This means that the measurement input for the particle filter is also an uncertain estimate. The results from the sensitivity analysis

in Section 4 show that the wheel rotational speeds show the highest sensitivity to a change in μ^{\max} . In addition, since the wheel rotational speeds are directly measured in every vehicle with ABS, they do not require an uncertain estimate. Thus, one possible approach could be to use the wheel's angular momentum as given in Equation 3.15 to estimate μ^{\max} . In discrete time notation, the i -th's wheel's rotational equilibrium for the time interval $\Delta t = t(k+1) - t(k)$ reads

$$\omega_i(k+1) = \omega_i(k) + \frac{1}{I_i} \cdot (M_{D,i}(k) - M_{R,i} - r_{S,i} \cdot F_{x,i}(k)) \cdot \Delta t. \quad (5.10)$$

Equation 5.10 is primarily determined by the difference between the momentum implied by the longitudinal tire force $F_{x,i}$ which is a function of μ^{\max} and the wheel's torque $M_{D,i}$. Nevertheless, changes of ω_i for typical driving states are smaller or within the same range as the accuracy with which the term $M_{D,i}(k) - M_{R,i} - r_{S,i} \cdot F_{x,i}(k)$ can be calculated, and this relation cannot be used directly. Thus, this work uses an approach related to the one proposed by Ray, [Ray97], in which the observed variables comprise the horizontal tire forces. *A priori* calculated values of the longitudinal tire force $F_{x,i}$ are used as the measurement input for the particle filter. Within the particle filter algorithm, these real values are then compared to N hypothesis of the longitudinal tire forces calculated using a tire model and N different particles of μ^{\max} . The real value of the longitudinal tire force $F_{x,i}$ is calculated using the discrete time notation of the wheel's angular momentum shown in Equation 5.10 and is given by

$$F_{x,i}(k) = \frac{1}{r_{S,i}} \cdot \left(M_{D,i}(k) - M_{R,i} - I_i \cdot \left(\frac{\omega_i(k+1) - \omega_i(k)}{\Delta t} \right) \right). \quad (5.11)$$

5.3.1. Overview on observer model

With the relation in Equation 5.11, the state model for the observer can now be defined using the notation for the state estimation problem given in Equations 5.2 and 5.2. The state vector \mathbf{x} is given by $\left[\mu_{fl}^{\max} \quad \mu_{fr}^{\max} \quad \mu_{rl}^{\max} \quad \mu_{rr}^{\max} \right]^T$. The measurement equation $\mathbf{z}(k)$ is given by $\left[F_{x,fl} \quad F_{x,fr} \quad F_{x,rl} \quad F_{x,rr} \right]^T$ and is being calculated for each wheel using Equation 5.11. Within the particle filter, the measurements $\mathbf{z}(k)$ are being compared to $\mathbf{h}(\mathbf{x}(k))$, assuming a multivariate Gaussian distribution (cf. Equation 5.6). The vector $\mathbf{h}(\mathbf{x}(k))$ includes the longitudinal tire forces that are calculated based on the model for combined horizontal tire forces presented in Section 3.3. It depends on the longitudinal slip $s_{x,i}$, the slip angle α_i , the vertical tire load $F_{z,i}$ and the state vector \mathbf{x} , i.e. μ_i^{\max} . Using N particles for μ_i^{\max} , N hypothesis for the longitudinal tire force are

calculated for each wheel.

Section 5.4 provides a more detailed description of the observer and the necessary measurements as well as vehicle and tire parameters. To calculate the tire forces for the N different hypotheses or particles of μ^{\max} , the horizontal tire model for combined forces presented in Section 3.3 is used.

5.3.2. Friction potential and longitudinal tire force

Before presenting the observer structure in Section 5.4, it is important to mention some reflections on the influence of μ^{\max} on the longitudinal tire force $F_{x,i}$. As discussed in Section 2.2.2, *Boßdorf-Zimmer* estimated both the slip angle α and μ^{\max} at the same time, [BZ07, p.84-86]. To implement the non-linear tire behaviour in an extended Kalman filter, he needed its derivatives to both α and μ^{\max} . He showed the lateral tire forces and their derivatives versus both α and μ^{\max} , [BZ07, p.84-86]. In the present work, the longitudinal tire forces are needed rather than the lateral tire forces within the observer model, see Section 5.4. Thus, Figure 5.2 shows the non-linear behaviour of $F_{x,i}$ versus both the longitudinal slip s_x and the friction potential μ^{\max} . Longitudinal tire force $F_{x,i}$ was calculated using the tire model shown in see Section 3.3 and parametrised with longitudinal tire data, see Table D.3.

Figure 5.2 (above) shows $F_{x,i}$ and its change $\Delta F_{x,i}/\Delta s_x$ with respect to s_x for two μ^{\max} . It can be seen that the initial slope for both $F_{x,i}$ and for $\Delta F_{x,i}/\Delta s_x$ does not depend on μ^{\max} . This is due to the tire model used, which, like most existing models, does not include any dependence of the initial slip slope on μ^{\max} , although a small effect has been empirically proven by *Dieckmann*, [Die92, p.32-45], see also Section 2.2.2. Only for higher values of s_x , does μ^{\max} show a distinguishable characteristic up until about 8 %. Figure 5.2 (bottom) shows $F_{x,i}$ and its change $\Delta F_{x,i}/\Delta \mu^{\max}$ with respect to μ^{\max} for two s_x . In these cases, it can be seen that the behaviour with respect to s_x is distinguishable. For small values of s_x (e.g. 0.5 % as shown in Figure 5.2), $\Delta F_{x,i}/\Delta \mu^{\max}$ is small. In contrast, the change in $F_{x,i}$ is higher for higher s_x , as shown for 6 %. According to *Boßdorf-Zimmer*, this shows that it is possible to simultaneously estimate μ^{\max} and s_x in an observer because the range of influence on $F_{x,i}$ is a different one. Although very promising, simultaneous estimation of s_x was not investigated in this thesis.

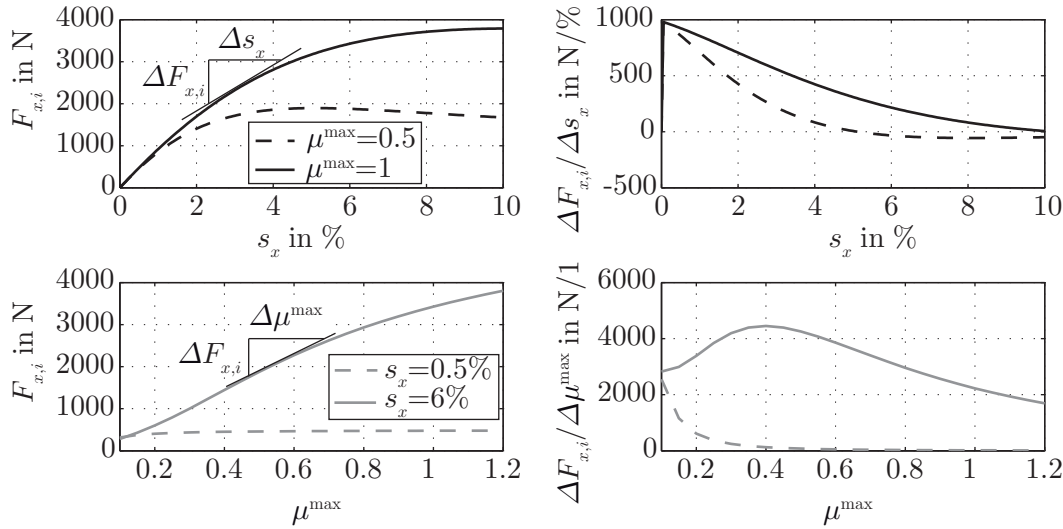


Figure 5.2.: Non-linear behaviour of longitudinal tire characteristics for $F_{z,i} = 3000$ N in dependence of longitudinal slip s_x for two μ^{\max} (**top left**) and depending on μ^{\max} for two s_x (**bottom left**). The right side shows the partial derivatives $\Delta F_{x,i}/\Delta s_x$ versus s_x (**top right**) and $\Delta F_{x,i}/\Delta \mu^{\max}$ versus μ^{\max} (**bottom right**). The graphic representation is based on *Boßdorf-Zimmer*, [BZ07, p.85].

5.4. Observer structure

Figure 5.3 provides a general overview of the non-linear observer used in this work. The inputs $\mathbf{u}(k)$ to both the real vehicle and the parallel observer are the inputs from the driver, including the steering wheel angle δ_S , the choice of gear and the activation of the accelerator and braking pedal. The wheel torque $M_{D,i}(k)$ accounts for the driver's inputs in the longitudinal direction. In the observer, a simplified model is used to incorporate the expected vehicle reaction to the inputs. The real vehicle is also exposed to disturbances $\mathbf{d}(k)$ (e.g. wind forces or road unevenness), which are not considered by the observer. The vehicle's state ${}_b\mathbf{z}(k)$ is measured and forwarded to the observer. It is a function of the internal state $\mathbf{x}(k)$, which is not directly measured, and the measurement noise $\mathbf{v}(k)$. It has to be mentioned that Figure 5.3 also shows an output ${}_b\dot{\mathbf{z}}(k)$. Although there is no direct relation such as an ODE considered for ${}_b\dot{\mathbf{z}}(k)$ within the model, its components ${}_b a_x$ and ${}_b a_y$ are necessary for the observer, e.g. to calculate the tire load variation (cf. Equation 3.22). Finally, an estimate $\hat{\mathbf{x}}(k)$ is calculated in the observer using a model of the observed variable. The observer itself is shown in more detail in Figure 5.4. The main component is the particle filter, where the most probable μ^{\max} is

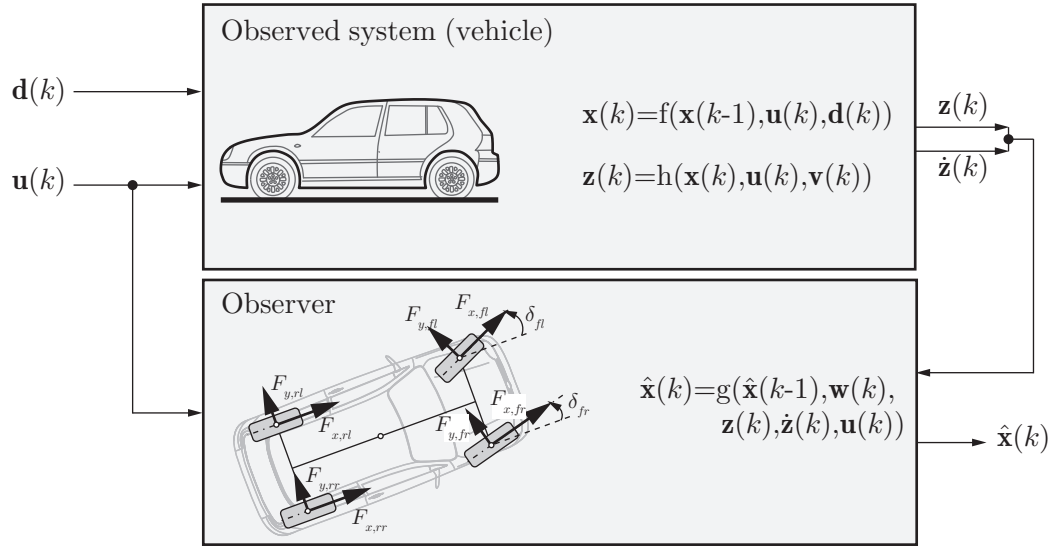


Figure 5.3.: Observed system (vehicle) and non-linear observer with the vector $\mathbf{u}(k)$ of the driver's input (steering wheel angle δ_S and wheel torque $M_{D,i}$) and the disturbance vector $\mathbf{d}(k)$ that are input to the real vehicle, and its outputs $\mathbf{z}(k)$ and $\dot{\mathbf{z}}(k)$, which are measured and fed into the observer model; based on *Simon*, [Sim06]. Within this model, the internal state $\hat{\mathbf{x}}(k)$ is estimated.

estimated based on the longitudinal tire forces, as shown in Section 5.3. For N particles of μ^{\max} , the hypotheses of the longitudinal tire forces are calculated at each wheel i with the respective tire load $F_{z,i}$, the longitudinal slip $s_{x,i}$ and the side slip angle α_i depending on the current inputs at time step k . Comparing this to a longitudinal force derived from the wheel's angular momentum with the inputs at time step k , see Equation 5.11, the most likely estimate of μ_i^{\max} for every wheel is calculated with the particle filter described in Section 5.2. In addition, a global μ^{\max} can be calculated using Equation 2.8. This can be done by directly applying Equation 2.8 to the prior estimated μ_i^{\max} or by observing all four wheel states at the same time, i.e. setting $\mathbf{h}(\mathbf{x}(k)) = [F_{x,fl} \ F_{x,fr} \ F_{x,rl} \ F_{x,rr}]^T$ as a function of one μ_g^{\max} rather than four wheel-individual μ_i^{\max} . The results from the two approaches do not vary significantly.

5.4.1. Measurement inputs

For an estimation method based on the vehicle dynamics, the theoretical achievable accuracy of an estimate of μ^{\max} depends on the dynamic excitation during a manoeuvre. The closer to the physical limits of road adhesion, the more accurate an estimate of μ^{\max} can be, see Section 6.1. Apart from this theoretical accuracy, the effectively

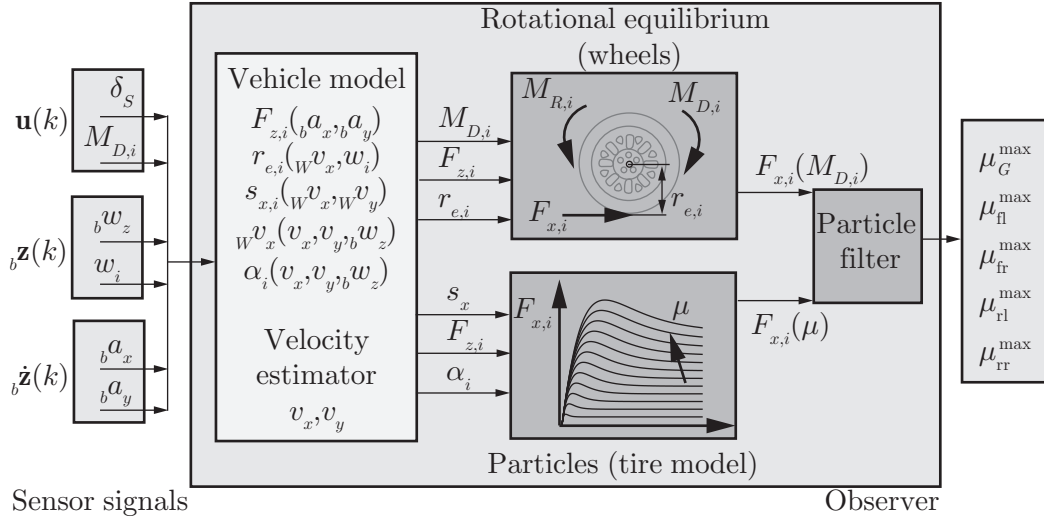


Figure 5.4.: Schematic structure of tire/road friction estimator showing the driver's inputs $\mathbf{u}(k)$, the measurement inputs $\mathbf{z}(k)$ and $\dot{\mathbf{z}}(k)$ on the left side and the estimation outputs $\hat{\mathbf{x}}(k)$ comprising $\mu_G^{\max}(k)$ and $\mu_i^{\max}(k)$ on the right side. The observer model consists of the vehicle model (cf. Section 3.2) and the velocity estimator, which deliver the inputs needed to calculate the expected $F_{x,i}$ based on the wheel's angular momentum and the tire forces from the horizontal tire model for N particles of μ^{\max} , which are then forwarded to the particle filter.

achievable accuracy depends on the accuracy of the measured and calculated inputs for the particle filter and also the accuracy of the necessary vehicle and tire parameters. The required parameters are discussed in Section 5.4.2. Table 5.1 shows all measured signals necessary for the tire/road friction estimator, as shown in Figure 5.4. All these signals are available in a vehicle equipped with ESC, except for the accurate longitudinal and lateral velocities, which have to be estimated, see Section 5.5.1. For all measurements and evaluations shown in Section 6, the sensor signals have been measured with a sample rate of 200 Hz. The accuracy of an estimate of μ^{\max} with the proposed method mainly depends on the accuracy of the inputs longitudinal slip $s_{x,i}$ and wheel torque $M_{D,i}$. The longitudinal slip $s_{x,i}$ is necessary for the calculation of the hypotheses of the longitudinal tire forces $F_{x,i}$ that depend on the the particles of μ^{\max} . An accurate calculation of $F_{x,i}$ and thus $s_{x,i}$ is particularly important. Therefore, these topics are discussed in more detail in Section 5.5. These hypotheses of $F_{x,i}$ are compared to an expected value of $F_{x,i}$ within the particle filter, which depends on the wheel torque $M_{D,i}$, the rolling resistance torque $M_{R,i}$ and the wheel's angular momentum $I_r \cdot \Delta\omega_i$, as shown in Equation 5.11.

5 Tire/road friction estimator

Table 5.1.: Necessary signals for the tire/road friction estimator, all measured with a sample rate of 200 Hz

Necessary Signal	Symbol	Source
Steering wheel angle	δ_S	measured
Wheel speeds	ω_i	measured
Longitudinal chassis accelerations	${}_b a_x$	measured
Lateral chassis acceleration	${}_b a_y$	measured
Yaw rate	${}_b \omega_z$	measured
Wheel's torque	$M_{D,i}$	calculated, see Section 5.5.3

Compared to $M_{D,i}$, the absolute values of $M_{R,i}$ and $I_r \cdot \Delta\omega_i$ are small and therefore play a minor role. The calculation of the wheel torque $M_{D,i}$ is shown in Section 5.5.3. Within the calculation of $M_{D,i}$, the vehicle's longitudinal acceleration ${}_b a_x$ is necessary. The acceleration ${}_b a_x$ is also required to calculate the dynamic tire load distribution, as well as ${}_b a_y$ during cornering. It has to be mentioned that for the results presented in Section 6, the acceleration signals have not been taken from the vehicle's CAN bus, as they were not available for all measurements due to a procedural error. Instead, the acceleration signals of an advanced measurement system, [Gmb14], were used. Since the higher accuracy of ${}_b a_x$ is not necessary within the observer, it is assumed that estimation with ESC acceleration sensors would not perform worse. As the results presented in Section 6 are limited to longitudinal manoeuvres, the influence of the accuracy of ${}_b a_y$ is not further discussed. It also has to be noted that estimates of v_x are typically available in the vehicle's COG. By measuring both the yaw rate and the steering wheel angle, the longitudinal velocity v_x in the vehicle's COG can be transformed to the i -th wheel-fixed coordinate system when the horizontal distances between wheel centre C and the vehicle's COG are known, cf. Section 3.2.

5.4.2. Model parameters

For the observer model, the knowledge of some vehicle and tire parameters is necessary. The vehicle parameters include the vehicle's mass m_b , the wheels' moment of inertia I_i and the rolling resistance coefficient $f_{r,i}$. To transform v_x and v_y or β from the vehicle's COG to the wheel's coordinate systems and into the wheel's contact points W_i , the horizontal distances from the four wheels' centres to the vehicle's COG have to be known. To calculate $F_{z,i}$, the position of the vehicle's COG, the vehicle's mass and the spring stiffnesses of the front and rear suspension have to be known (cf. Equation

3.22). The calculation of $M_{D,i}$ is discussed in Section 5.5.3. A model for combined longitudinal and lateral forces is used to consider the reduced longitudinal force available when longitudinal and lateral tire forces are present. Thus, lateral tire parameters also have to be known to calculate $F_{x,i}$. In total, six parameters each for the longitudinal and lateral tire force characteristics, as well as the nominal tire load $F_{z,nom}$ and nominal friction potential μ_0 have to be known (cf. the tire model described in Section 3.3). Tables D.4 and D.3 show the parameters needed for the vehicle and the tire, respectively.

5.5. Considerations for the calculation of the longitudinal tire forces

Within the rotational equilibrium for the wheels, see Equation 5.10, the horizontal tire force model described in Section 3.3.1 was used to calculate $F_{x,i}$. The transmittable $F_{x,i}$ is limited when an additional $F_{y,i}$ is present (cf. the depiction of the Krempel ellipse shown in Figure 2.5). This implies that $F_{y,i}$ also impacts the calculation of $F_{x,i}$ due to the combined tire model used. The inputs needed to calculate both $F_{x,i}$ and $F_{y,i}$ are the longitudinal slip $s_{x,i}$, the slip angle α_i and the tire load $F_{z,i}$. As discussed in Section 2.2.2, the treatment of $s_{x,i}$ is the most critical part in most published friction potential estimation algorithms. The calculation of α_i is also not trivial, but fortunately it is not needed with a high accuracy for $F_{x,i}(F_{y,i})$. In addition, the results presented in Section 6 focus on longitudinal manoeuvres. Some considerations concerning the estimation of both $s_{x,i}$ and α_i are shown in Section 5.5.1 and E.3.

Unfortunately, more than ESC sensors were necessary to calculate the longitudinal slips $s_{x,i}$ with the required accuracy, see Section 5.5.1. For a future application, it is crucial to place greater emphasis on the slip determination. Nevertheless, with approaches combined with a global navigation satellite system (GNSS) or radar sensors, it will be possible to achieve the necessary accuracy of the longitudinal slip s_x for series application. A discussion of the most promising methods to estimate s_x as proposed in literature is also provided in Section 5.5.1. It also has to be mentioned that the hypotheses of the longitudinal tire forces $F_{x,i}$ based on the tire model and the particles of μ^{\max} had to be corrected with a linear factor¹. The exact origin of the deviation is unclear, but it very likely comes from parameter inaccuracies. A deviation of the parameter μ_0 in Equation

¹The longitudinal tire forces had to multiplied with 0.8 for the wheels on the front axle and 0.6 on the rear axle, meaning that only 80 % and 60 % of the calculated hypotheses of $F_{x,i}$ were considered, respectively

B.3 in the horizontal tire data shown in Table D.3 measured on a tire test bench can be excluded, since this effect does not have a linear dependence with $s_{x,i}$.

5.5.1. Estimation of the longitudinal slip

To use the definition of $s_{x,i}$ presented in Equation 2.3 in Section 2.1.2, the wheel's rotational speed ω_i , the vehicle's longitudinal velocity v_x and the effective tire radius $r_{e,i}$ are required. For the wheel's rotational speed ω_i , the series-application ABS sensors of the vehicle were used. The signals were not taken from the CAN bus directly to avoid time delays, a low sample rate and dealing with an unknown filter used in the control unit. Instead, an analogue signal of the ABS sensors was used directly and then filtered using a one-dimensional median filter with order 10, meaning that the median values of the measurements of the last 10 time steps are used to calculate the output for the current time step.

An accurate monitoring of the vehicle's longitudinal velocity v_x is more difficult. There are different approaches to calculate v_x using different sensor combinations, see Appendix E. Within this work, the reference velocity v_x was measured using a combination of GNSS and inertial measurement, as discussed in Section 5.5.1. It has to be mentioned that the inertial measurement platform was not a low-cost sensor, but an advanced laboratory measurement system, [Gmb14]. For automotive series-application, these signals have to be replaced. The velocity estimation methods mentioned in Appendix E also discuss promising solutions for automotive series-application regarding costs.

A model for the effective tire radius $r_{e,i}$ is shown in Equation 3.23 in Section 3.2.3. The measurements showed that for real driving states, these influences seem to play a minor role compared to other factors. For this reason, $r_{e,i}$ was regularly reset for each wheel using free rolling manoeuvres. As proposed by *Miller et al.*, v_x calculated based on global navigation satellite system (GNSS) velocity and inertial measurements was used to calculate $r_{e,i}$ during free rolling, [MYM⁺01]. Using the constant values of these calibrated $r_{e,i}$ showed better results than additionally considering Equation 3.23. The calculated value of s_x was filtered again with a one-dimensional median filter with an order of 50.

5.5.2. Estimation of the slip angles

Several approaches for estimating the side slip angle or the horizontal velocities in the vehicle's COG have been published. In this work, a non-linear observer developed by *Kollienz*, [Kol13, p.34-42], which is based on *Zhao et al.*, [ZLC11], was used. With measurements of ${}_b a_x$, ${}_b a_y$ and ${}_z \omega_z$, the velocities v_x and v_y in the vehicle's COG are estimated based on a two-track vehicle model for a given wheel torque $M_{D,i}$ and the steering wheel angle δ_S . As mentioned in the case of v_x for the estimation of s_x , the lateral velocity component v_y or the side slip angle β in the vehicle's COG also need to be transformed from the vehicle's COG to the i -th wheel-fixed coordinate system.

5.5.3. Wheel's torque

In the case of propulsion (no braking), the wheel's torque can be calculated based on the engine torque, which is available on the vehicle's CAN bus. Thus, the wheel's torque is calculated based on gear ratios within the powertrain, also considering the current gear and the mechanical efficiency. Unfortunately, for the majority of measurements the demanded engine torque was measured instead of the delivered engine torque. As the signal course of the demanded engine torque is clearly linked to accelerator pedal activation, but not directly linked to the vehicle's reaction, it could not be used. Using it to directly calculate $M_{D,i}$ resulted in a non-negligible time delay between wheel's torque and wheel's longitudinal slip s_x in the range of tenths of a second. With a first order element, this behaviour could be reproduced for many conditions, but problems with the amplitude compared to the course of ${}_b a_x$ still remained. Overall, the approach described below was more applicable. However, this does not automatically imply that the original proposal would perform worse.

Instead, the wheel torque was calculated using the vehicle's body longitudinal acceleration ${}_b a_x$, which is comparable to the approaches of *Ray*, [Ray97], *Rajamani*, [RPLG06], etc. This approach has also been used to calculate the wheel's torques in the case of braking. Interventions of systems like ABS, TC or ESC were not considered and those systems were also deactivated during the driving tests. For future applications, effects of these systems will have to be investigated.

Excluding additional wind forces $F_{W,x}$ and road slope β_r in the applied forces given by Equation 3.9, the total of longitudinal applied forces acting on the vehicle reads ${}_b \sum F_x = \sum_i {}_b F_{x,i} - F_A$. Using this relation in the first row of Equation 3.6, which

5 Tire/road friction estimator

describes the linear momentum of the vehicle in longitudinal direction, and substituting ${}_b a_x = \dot{v}_x - {}_b \omega_z \cdot v_y$, the overall tire forces for accelerating and braking are given by

$$\sum_i {}_b F_{x,i} = m_b \cdot {}_b a_x - F_A. \quad (5.12)$$

The total of longitudinal forces $\sum_i {}_b F_{x,i}$ has to be apportioned to the four wheels based on the driving and braking torque distribution. Since the tested vehicle was front-wheel driven, 50 % was assigned to each front wheel during driving. During deceleration, a braking distribution of 60 % on the front axle and 40 % on the rear axle is considered. On each axle, the left and the right wheel are assigned 50 % of the axle's theoretical braking force each. These assigned forces could have been used directly in the particle filter to be compared to the longitudinal tire forces for the different particles of μ^{\max} . However, it is assumed that a good wheel torque estimate will improve the algorithm and may be available in an industrial implementation.

6. Results and conclusion

This chapter presents the results for several driving manoeuvres, including accelerating and braking. The identification of the friction potential on high and low-friction surfaces, as well as for changing road conditions (μ *step*) and different road conditions on the left and right wheels (μ *split*) were investigated. In addition, examples of the influence of the longitudinal acceleration on the estimation accuracy is shown. Concerning the particle filter, this chapter discusses how the evolution of particles versus time affects the μ^{\max} estimate and shows strategies for influencing the course of particles. The achieved accuracy of the friction potential estimate is discussed with respect to the requirements established in Section 1.3.2 for the application in an autonomous emergency braking system (AEB), which was chosen as an exemplary application of a friction potential estimate to adapt an ADAS activation strategy. This chapter then concludes with a general discussion of the results and provides an outlook.

6.1. Strong acceleration manoeuvre with constant μ^{\max}

Figure 6.1 shows different hypotheses of $F_{x,i}$ (gray) for different particles of μ^{\max} during an acceleration manoeuvre. As described in Section 5.2, N hypotheses of longitudinal tire forces $F_{x,i}$ are calculated for all N particles of μ^{\max} for the inputs of the longitudinal slip s_x , the side slip angle α and the tire load $F_{z,i}$ of the current time step k . These are then compared to the expected tire force (black) at each time step, which is calculated based on the engine torque $M_{D,i}$ or with the vehicle's longitudinal acceleration ${}_b a_x$, cf. Section 5.5.3.

It can be seen in Figure 6.1 that between about second 4.7 and 5, $F_{x,i}(M_{D,i})$ (black) is momentarily higher than is posited by any of the hypothesis of F_x (particles) (gray). This can happen due to inaccuracies in the calculation of either $F_{x,i}(M_{D,i})$ or $F_{x,i}(s_{x,i}, N)$. In this case, the highest particle is assigned the highest probability. Although it is not possible to extrapolate to conditions outside of the minimum and maximum particle values, interpolation between the discrete particle states is carried out at each time step.

6 Results and conclusion

It can also be seen around second 5 that the hypotheses of $F_x(\text{particles})$, which depend on s_x , show a steeper slope for the simulated manoeuvre than $F_x(M_{D,i})$.

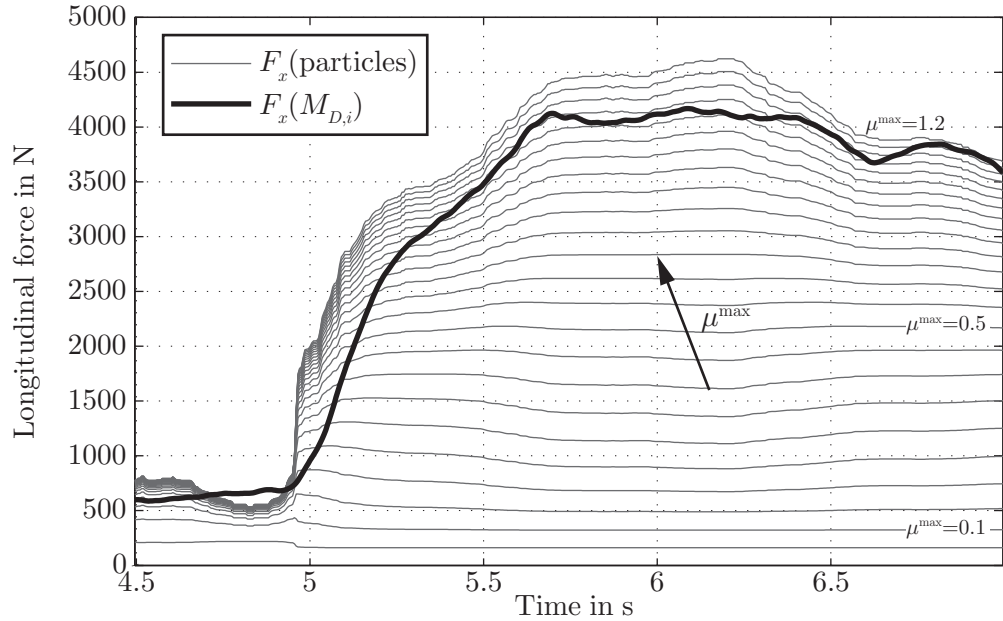


Figure 6.1.: Hypotheses for longitudinal tire forces $F_{x,i}$ (gray) for different particles (e.g. values) of μ^{\max} , but with the same inputs for longitudinal slip s_x , side slip angle α and tire load $F_{z,i}$. The thick black line denotes the expected longitudinal tire force based on the vehicle's acceleration ${}_b a_x$.

6.1.1. Results without resampling step

Section 5.2 described the particular steps within the particle filter and also mentioned an implementation without the resampling step. Without this step, the particles of μ^{\max} do not change with time. Thus, the hypotheses of the longitudinal tire forces are always calculated for the same particles. At every time step, the particles of μ^{\max} are assigned probabilities, which then makes it possible to calculate an estimate using the probability of each particle as its weight for each time step.

Since the probabilities of the particles are calculated based on the difference between the hypothesized values of $F_{x,i}$ and $F_{x,i}(M_{D,i})$ for every time step, every small deviation between the expected and the current inputs results in an inaccurate estimate. In the best case, the estimate just appears noisy. These deviations occur due to measurement uncertainties, especially in the determination of s_x and $M_{D,i}$. Deviations also arise due

to model simplifications. As ${}_b a_x$ reacts with a time delay to longitudinal forces built up on the wheel, the estimate of μ^{\max} deviates in these transient areas with changing acceleration, see the example in Figure 6.1 around second 5. Nevertheless, this specific behaviour of a particle filter without the resampling step, which uses only fixed particles, enables fast detection of changes in the observed variable.

Figure 6.2 shows the course of ${}_b a_x$ for a driving manoeuvre on dry road starting around second 5 with a maximum acceleration ${}_b a_x \approx 4.5 \text{ m/s}^2$, which corresponds to the maximum achievable acceleration of the test vehicle at an initial speed of about 20 kph.

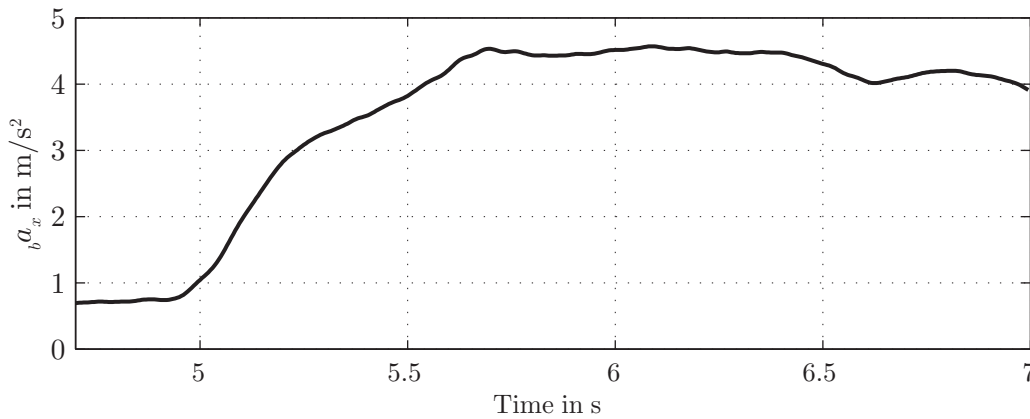


Figure 6.2.: Longitudinal acceleration ${}_b a_x$ during acceleration manoeuvre as shown in Figure 6.3 performed on dry road with a maximum acceleration ${}_b a_x \approx 4.5 \text{ m/s}^2$. The manoeuvre was started at $v_x = 20 \text{ km/h}$ and ended at 50 km/h .

Figure 6.3 shows the estimate of μ^{\max} using a particle filter with fixed particles for the manoeuvre shown in Figure 6.2. The reference value for the friction potential was determined using measurements at the longitudinal and lateral physical limits with the vehicle and the investigated tires and by comparing these results to tire characteristics measured on a tire test-bench. The reference values for the tires show a slight variation, which is due to the degressive influence of the vertical tire load (cf. Section 2.1.3). Due to the steeper slopes of $F_x(\text{particles})$ compared to $F_x(M_{D,i})$, as shown in Figure 6.1, μ^{\max} shows a higher deviation between the estimate of μ^{\max} and the reference value in Figure 6.3 shortly before second 5 and until about second 5.5. A similar effect can also be observed at around second 6.2. Although ${}_b a_x$ is still constant, s_x already decreases.

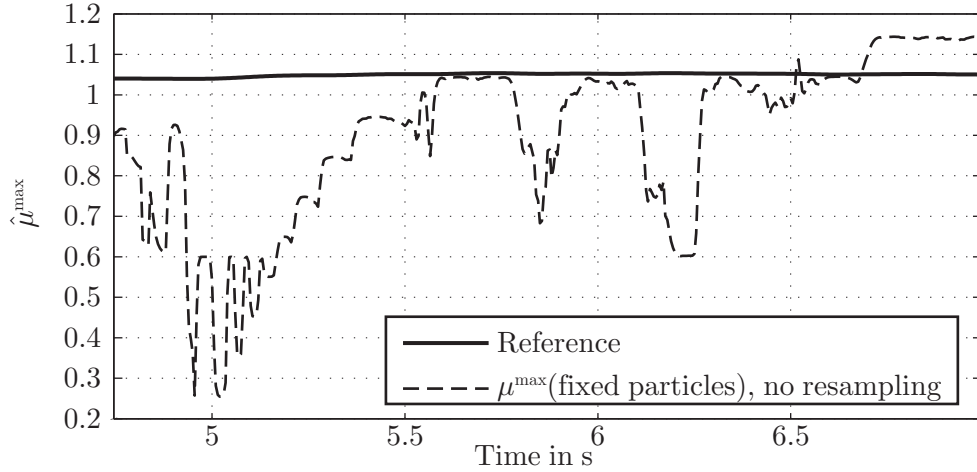


Figure 6.3.: Estimate of μ^{\max} for a driving manoeuvre with a longitudinal acceleration of $b a_x \approx 4.5 \text{ m/s}^2$ with fixed particles of μ^{\max} for all time steps. The mean absolute error (MAE) of the estimate is 0.1725 and the maximum absolute error of 0.7860 occurs around second 5, see also Table 6.1.

6.1.2. Results with resampling step

With the resampling step described in Section 5.2 and the particles moving towards the most probable condition shown in Figure 5.1, convergence towards the most likely state can be achieved by smoothing short-term outliers. Figure 6.4 shows how the particles converge with time (top) for the manoeuvre shown in Figure 6.2 and how, in contrast, the particles of the particle filter without the resampling step (fixed particles, bottom) stay constant over time. It has to be mentioned that regardless of whether a particle is fixed or variable, its PDF changes with time.

Figure 6.5 shows three exemplary results of the estimation with μ^{\max} for the same measurement input. As the resampling strategy is subject to chance, the outcome of every experiment or run on the same measurement input is slightly different. Thus, three different outcomes are shown as examples. It can be seen that the resampling step delivers a smooth and accurate estimate.

When including a resampling step, the maximum deviations between the reference and the estimated μ^{\max} are small. For the examples shown in Figure 6.5, the mean absolute error (MAE) is less than 0.08, and the absolute error is still less than 0.15, see Table 6.1. There is a reason that all three examples converge to different values even though

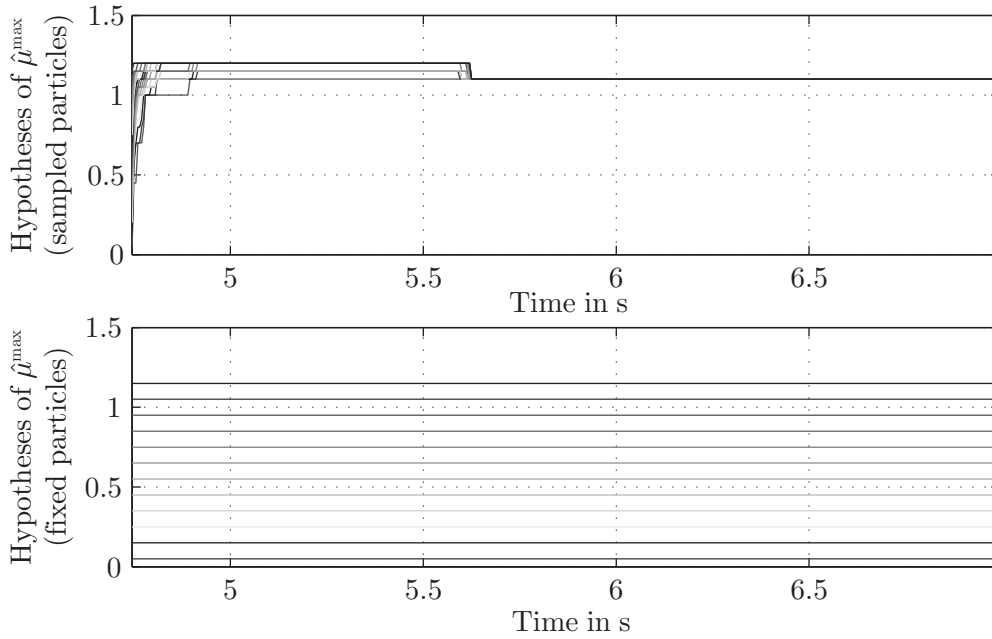


Figure 6.4.: **Top:** Different particles marked by gray scale converge with time to the most likely value of μ^{\max} for particle filter with resampling step (The corresponding estimate to this particle behaviour is shown as Example 1 in Figure 6.5). **Bottom:** Particles are fixed and thus remain constant versus time for particle filter without resampling step (Depiction corresponding to the estimate shown in Figure 6.3).

they are fed the same input. It results from the chance-based resampling algorithm that deletes unlikely states and multiplies very likely states based on the particles' PDF. Thus, the time to convergence and the values to which the particle filter converges vary. Once the presented particle filter converged, the estimate no longer changes, regardless of whether the inputs and the value to be observed have changed. It has to be mentioned that changes in the estimate can no longer be identified after all particles have moved towards the current most probable value. Thus, the particles have to be reset or re-initialised after convergence in order to be able to detect changes. The following section describes and compares two methods that enable new spreading of particles under certain circumstances.

6.1.3. Resampling step with particle re-initialisation

For initial tests, 12 fixed and 24 variable particles were used in parallel, and the most likely estimate for each of the set of particles was calculated. In a first approach, the

6 Results and conclusion

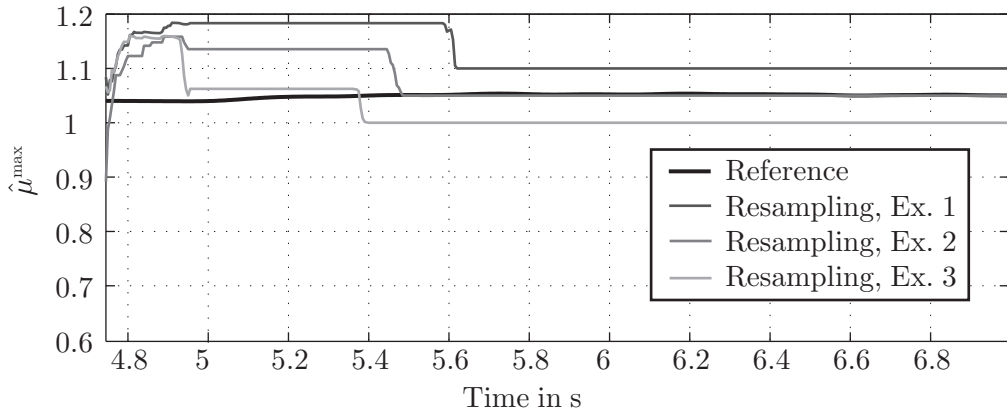


Figure 6.5.: Three estimation examples of μ^{\max} for a driving manoeuvre with a longitudinal acceleration of ${}_b a_x \approx 4.5 \text{ m/s}^2$ with variable particles of μ^{\max} converging due to resampling. Mean absolute errors (MAE) and maximum absolute error of the three estimates are shown in Table 6.1.

Table 6.1.: Mean absolute error (MAE) and maximum absolute error for driving manoeuvre with ${}_b a_x \approx 4.5 \text{ m/s}^2$

Example	Mean absolute error (MAE)	Maximum absolute error
Fixed Particles	0.1725	0.7860
Variable Particles, Ex. 1	0.0798	0.1445
Variable Particles, Ex. 2	0.0299	0.1486
Variable Particles, Ex. 3	0.0494	0.1209

weighted sum of both estimates was used, which unfortunately combined the disadvantages of both estimators. Once the estimate of the variable particles converged, it did not change anymore with time, whereas the estimate of the fixed particles contributed noise to the final estimate.

In a second step, it was considered that the state of convergence of the estimate is known because of the current distribution of the variable particles. Thus, by observing the standard deviation (SD) of the particles at each time step, it is evident when particles are no longer changing over time and thus should be re-initialised. A limit of the standard deviation of 0.1 was attempted, see Figure 6.6. It can be seen that for the investigated manoeuvre shown in Figure 6.2, the SD was often below this limit, resulting in many re-initialisations of the particles. This makes the estimate noisy, but enables fast detection of changes in μ^{\max} . During re-initialisation, the initial distribution of

particles was always used. A particle distribution that is different than the initial one (e.g. based on the particles' PDF) might improve an estimate, but this was not investigated. In addition, the SD limit can be optimized. This re-initialisation method has the advantage that no fixed particles need to be calculated in parallel.

In a third step, an alternative initialisation strategy for the variable particles was implemented using the difference between the estimates of the variable and the fixed particles. If the difference between $\hat{\mu}^{\max}$ (fixed particles) and $\hat{\mu}^{\max}$ (variable particles) was higher than a set limit of 0.2, it was assumed that there had been a change of μ^{\max} , and the current variable particles were replaced with particles with the initial distribution. This criterion was exceeded less frequently during the manoeuvre shown in Figure 6.6 than when using the SD limit discussed above, which led to a smoother estimate. Again, it may be possible to improve the estimate by adjusting the set limit (e.g. in dependence on the covariance) and by an alternative selection of the distribution of the new particles. Table 6.2 shows the impact of the choice of re-initialisation on the estimate's accuracy, which is discussed further below.

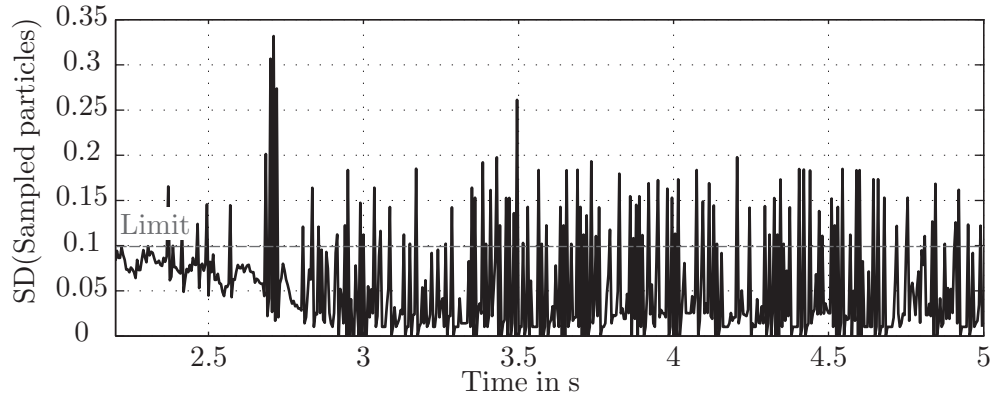
6.2. Strong braking manoeuvre with varying μ^{\max}

To evaluate the performance of the two proposed particle re-initialisation methods, a so-called μ *step* manoeuvre, in which the road surface changes during the manoeuvre, was selected. Thus, during a braking manoeuvre with a deceleration of ≈ -4.5 m/s² as shown in Figure 6.7, the test vehicle drove from dry road ($\mu^{\max} \approx 1$) to icy road ($\mu^{\max} \approx 0.3$). The resulting estimates using both fixed particles and variables particles re-initialised by SD or $\Delta\hat{\mu}^{\max}$, as shown in Figure 6.8. It can also be seen in Figure 6.8 that the estimate using variable particles re-initialised by SD (light gray) is very noisy, due to the high number of re-initialisations. It is interesting that it is even noisier than the method using no resampling step (black dotted). Nevertheless, the changes in μ^{\max} are detected quickly with both methods mentioned. In contrast, the estimate using variable particles that are re-initialised based on $\Delta\hat{\mu}^{\max}$ (dark gray) is very smooth, but needs more time to detect the decrease in μ^{\max} . Furthermore, for this case, the real value is not as well met as with fixed particles or re-initialisation using SD limits. This occurs because the particles are not newly distributed, which suggests that the limit of 0.2 may be too high.

Figure 6.9 shows the behaviour of the particles versus time for the two different ini-

6 Results and conclusion

a) Standard deviation of sampled particles



b) Difference between $\hat{\mu}^{\max}$ (sampled particles) and $\hat{\mu}^{\max}$ (fixed particles)

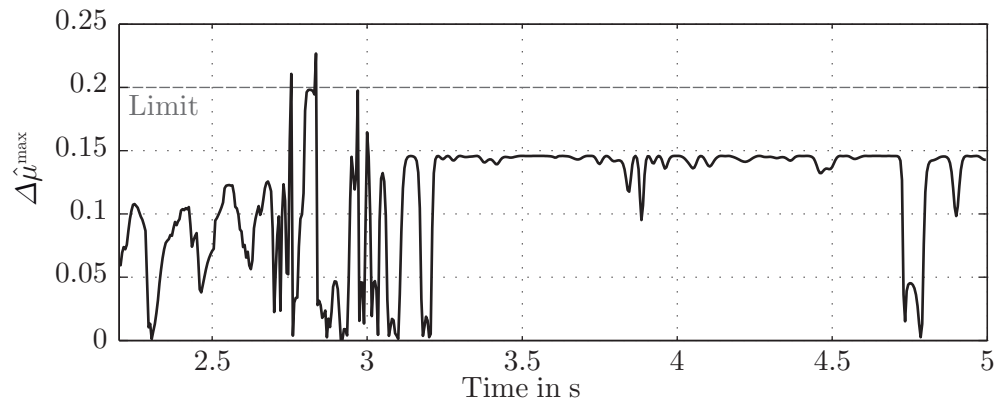


Figure 6.6.: **Top:** Standard deviation (SD) of variable particles (black) and SD limit of 0.1 (gray) versus time during a braking manoeuvre with deceleration of $\approx -4.5 \text{ m/s}^2$ for a μ step manoeuvre. **Bottom:** Difference $\Delta\hat{\mu}^{\max}$ between $\hat{\mu}^{\max}$ (fixed particles) and $\hat{\mu}^{\max}$ (variable particles) and the limit of 0.2 versus time for the same manoeuvre.

tialisation methods. Whereas in the case of SD, the number of re-initialisations is high, see Figure 6.9 (top), the infrequent re-initialisation using $\Delta\hat{\mu}^{\max}$ as shown in Figure 6.9 (bottom) favors higher deviations between the reference value and the estimate which is not corrected versus time.

Table 6.2 shows the MAE and maximum absolute errors for the estimates shown in Figure 6.8. For the short periods of time where a change in μ^{\max} is not yet detected, the maximum absolute error of about 0.75 is quite high for all three cases. For this manoeuvre in general, the estimate $\hat{\mu}^{\max}$ (fixed particles) shows the best accuracy with

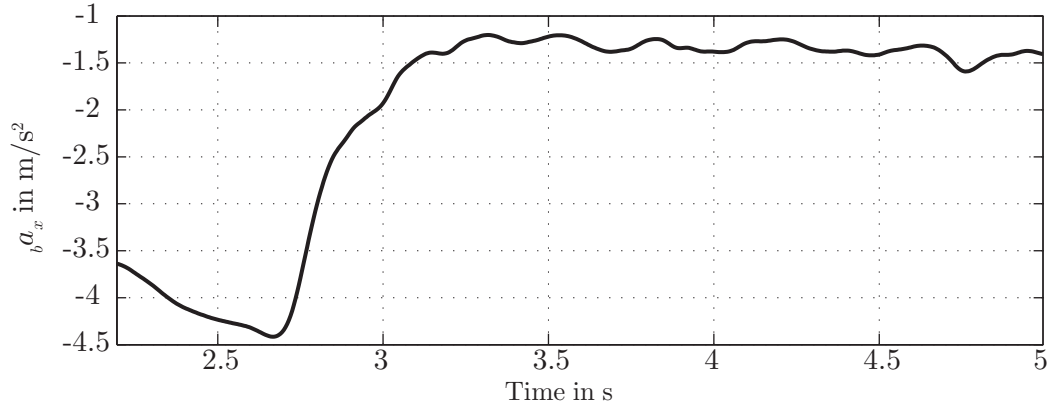


Figure 6.7.: Longitudinal acceleration ${}_b a_x$ during a braking manoeuvre on varying μ^{\max} with a maximum deceleration ${}_b a_x \approx -4.5$ m/s². The manoeuvre was started at $v_x \approx 50$ km/h and ended at 30 km/h.

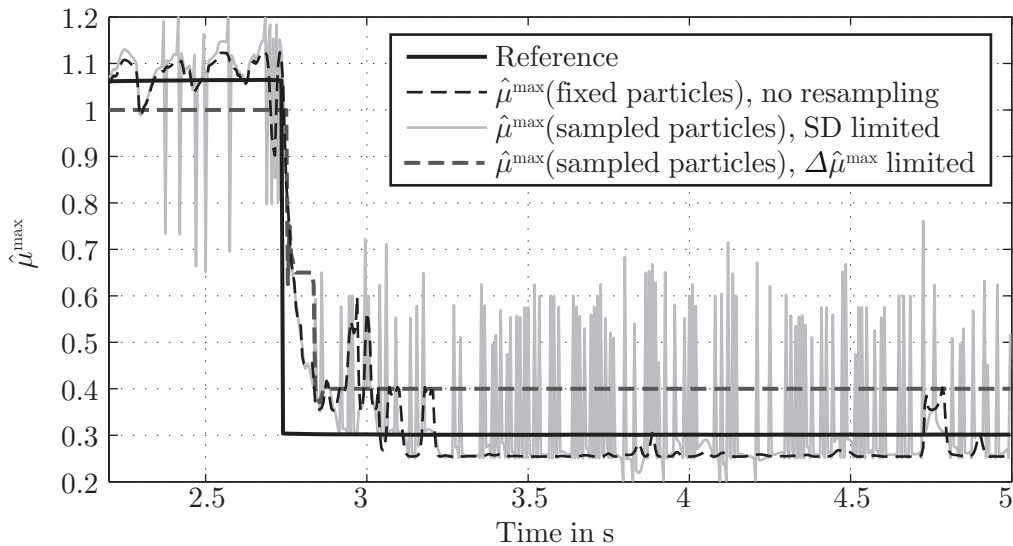


Figure 6.8.: Estimates of μ^{\max} using fixed particles (black dotted), variable particles re-initialised based on SD (light gray) or variable particles re-initialised based on $\Delta\hat{\mu}^{\max}$ (dark gray) versus time during a braking manoeuvre with deceleration of ≈ -4.5 m/s² for a μ step manoeuvre with $\mu^{\max} \approx 1$ before and $\mu^{\max} \approx 0.3$ after second 2.75. MAE and maximum absolute errors are shown in Table 6.2.

an MAE below 0.06 and the fast detection of the change in μ^{\max} . The overall accuracy of the estimate using $\Delta\hat{\mu}^{\max}$, described by its MAE of 0.1035, performs slightly worse than the two other approaches, due to the low value of μ^{\max} not being accurately met.

Table 6.2.: Mean absolute error (MAE) and maximum absolute error for all braking manoeuvres

Example	Mean absolute error (MAE)	Maximum absolute error
Braking ($\approx 4.5 \text{ m/s}^2$), $\mu \text{ step}$		
fixed	0.0582	0.7496
SD	0.0970	0.7549
$\Delta\hat{\mu}^{\max}$	0.1035	0.6964
Braking ($\approx 2 \text{ m/s}^2$), $\mu \text{ step}$		
fixed	0.3029	0.9969
SD	0.2973	1.0027
$\Delta\hat{\mu}^{\max}$	0.3577	1.0034
Braking ($\approx 3 \text{ m/s}^2$), $\mu \text{ split}$, low		
fixed	0.1953	0.3529
SD	0.1592	0.4669
$\Delta\hat{\mu}^{\max}$	0.1582	0.3954
Braking ($\approx 3 \text{ m/s}^2$), $\mu \text{ split}$, high		
fixed	0.6025	1.0088
SD	0.6010	1.0197
$\Delta\hat{\mu}^{\max}$	0.6508	1.0210

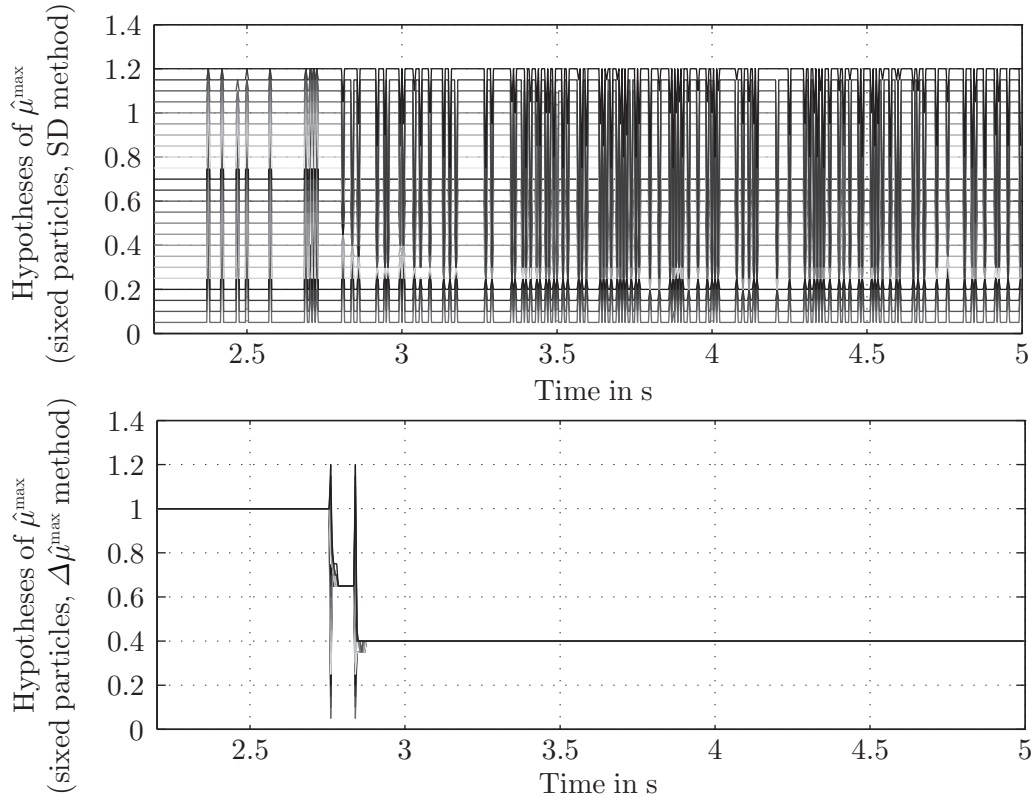


Figure 6.9.: Convergence and re-initialisation of variable particles marked by gray scale using the standard deviation (SD) of the variable particles (**top**) and the difference $\Delta\hat{\mu}^{\max}$ between the estimates of fixed and variable particles (**bottom**).

6.3. Gentle braking manoeuvre on varying μ^{\max}

Since the proposed method for estimating μ^{\max} requires a change in the driving state, the value of longitudinal acceleration ${}_b a_x$ acting on the vehicle's body has an influence on the estimation accuracy. The closer ${}_b a_x$ is to the physical limits partly set by μ^{\max} , the more accurately μ^{\max} can theoretically be estimated. Thus, high values of ${}_b a_x$, as previously discussed, are assumed to generally provide better estimation results. Figure 6.10 shows the estimates of μ^{\max} for a braking manoeuvre with a maximum deceleration of $\approx -2 \text{ m/s}^2$ as shown in Figure 6.11 that was performed during a μ step manoeuvre, starting on dry road ($\mu^{\max} \approx 1$) and proceeding to icy road ($\mu^{\max} \approx 0.3$) at second 9. Due to the significant difference between the low ${}_b a_x$ and the high μ^{\max} , the dry road condition cannot be detected at all. It appears that the low dynamic excitation is being confused with a low μ^{\max} . Regardless of the method, only the low-friction surface can

6 Results and conclusion

be detected in an acceptable and reliable manner. The inferior performance during this manoeuvre that includes a low dynamic excitation on a road with high μ^{\max} road is also visible in the error values in Table 6.2 when one compares its error values to those for the manoeuvre with the higher dynamic excitation. Nevertheless, the MAE is still below 0.35 for all methods, which is remarkable considering the total failure to detect the dry surface. Looking more closely at the estimate using variable particles re-initialised by SD (light gray) in Figure 6.10, the SD on the dry road (before second 9) appears higher than on the correctly detected low-friction surface. Thus, the SD might be a helpful measure to estimate the current estimation accuracy.

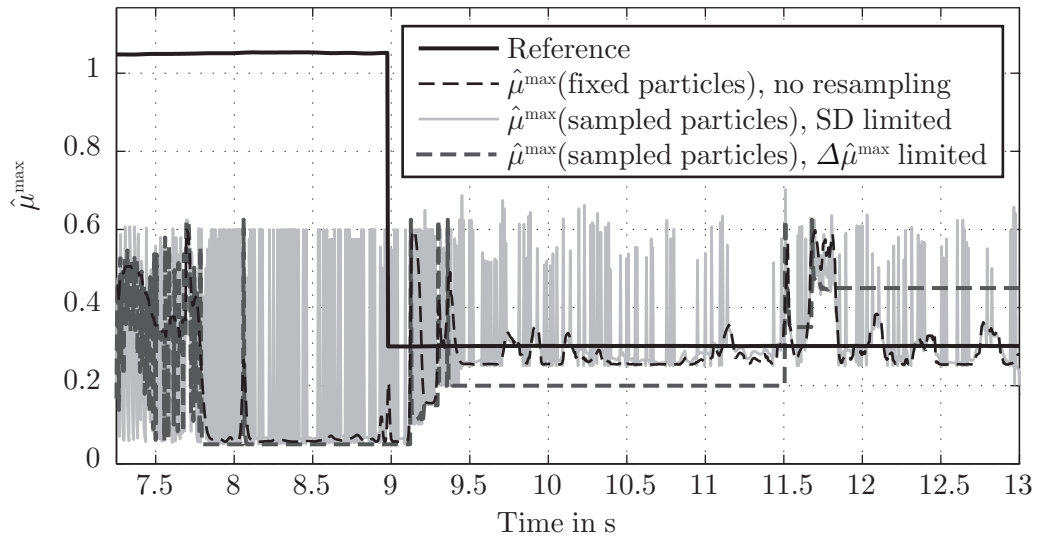


Figure 6.10.: Estimates of μ^{\max} using fixed particles (black dotted), variable particles re-initialised based on SD (light gray) or variable particles re-initialised based on $\Delta\hat{\mu}^{\max}$ (dark gray) versus time during a braking manoeuvre with a maximum deceleration of $\approx -2 \text{ m/s}^2$ for a μ step manoeuvre with $\mu^{\max} \approx 1$ before and $\mu^{\max} \approx 0.3$ after second 9. MAE and maximum absolute errors are shown in Table 6.2.

Figure 6.12 clearly shows that the SD for this manoeuvre is generally lower after the step of μ^{\max} occurs at second 9. Knowledge about the actual accuracy is of great interest when considering the application of an estimated μ^{\max} for adaptation of the activation strategy of ADAS. *Kobialka et al.* showed that the estimation of the estimation accuracy is possible using ANN, [KL13]. Nevertheless, further investigations are necessary to support the hypothesis that the SD of the variable particles can be used for accuracy estimation.

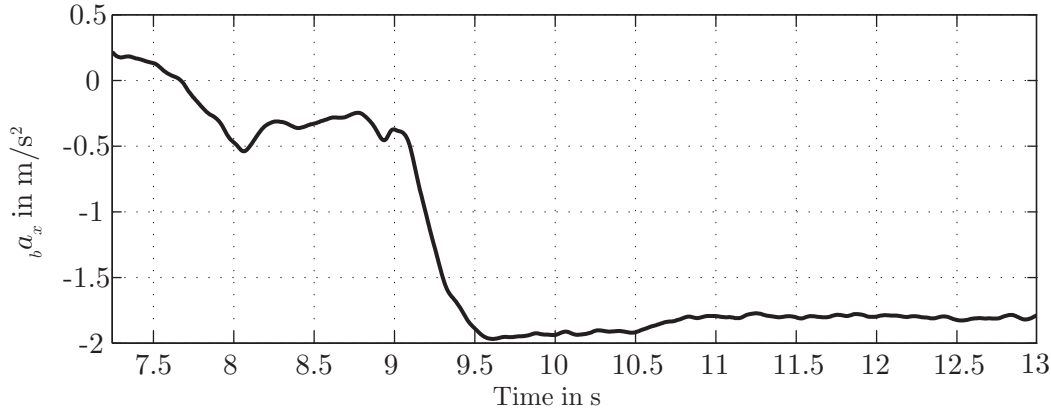


Figure 6.11.: Longitudinal acceleration $b a_x$ during gentle braking manoeuvre on varying μ^{\max} with a maximum deceleration $b a_x \approx -2 \text{ m/s}^2$. The manoeuvre was started at $v_x \approx 40 \text{ km/h}$ and ended at 15 km/h .

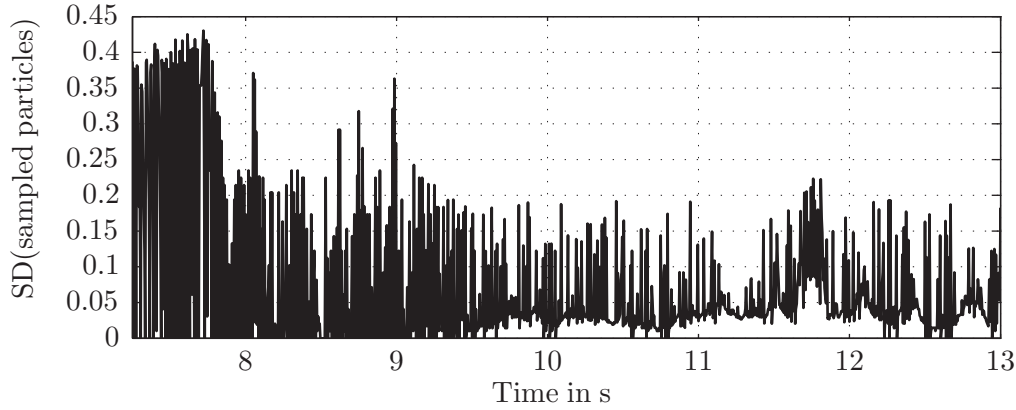


Figure 6.12.: Standard deviation of variable particles versus time during a braking manoeuvre with a maximum deceleration of $\approx -2 \text{ m/s}^2$ for a μ step manoeuvre with $\mu^{\max} \approx 1$ before and $\mu^{\max} \approx 0.3$ after second 9. The corresponding estimate $\hat{\mu}^{\max}$ is shown as a light gray line in Figure 6.10.

6.4. Braking manoeuvre on μ split conditions

The last case which is examined are different road conditions for the left and the right sides of the vehicle, a so-called μ split condition. In the investigated case, the left side of the vehicle (i.e. wheel indices fl and rl) was located on a low-friction surface ($\mu^{\max} \approx 0.3$), whereas the right side (i.e. wheel indices fr and rr) was located on a surface with $\mu^{\max} \approx 1$. The driver was supposed to keep the vehicle straight (yaw angle $\psi \approx 0$) during the manoeuvre using steering inputs.

6 Results and conclusion

The estimation result for the wheel located on the low-friction surface is shown in Figure 6.13, which shows a braking manoeuvre with a maximum deceleration of $\approx -3 \text{ m/s}^2$ as shown in Figure 6.14. Although the estimates deviate from the real value within the first second, the overall estimation performance is acceptable. These deviations can be partly explained by the fact that during abrupt braking manoeuvres, the local water film under the tire does not stay constant, which leads to an inaccurate reference value of μ^{\max} . In accordance with the results presented in Section 6.3, the algorithm fails to

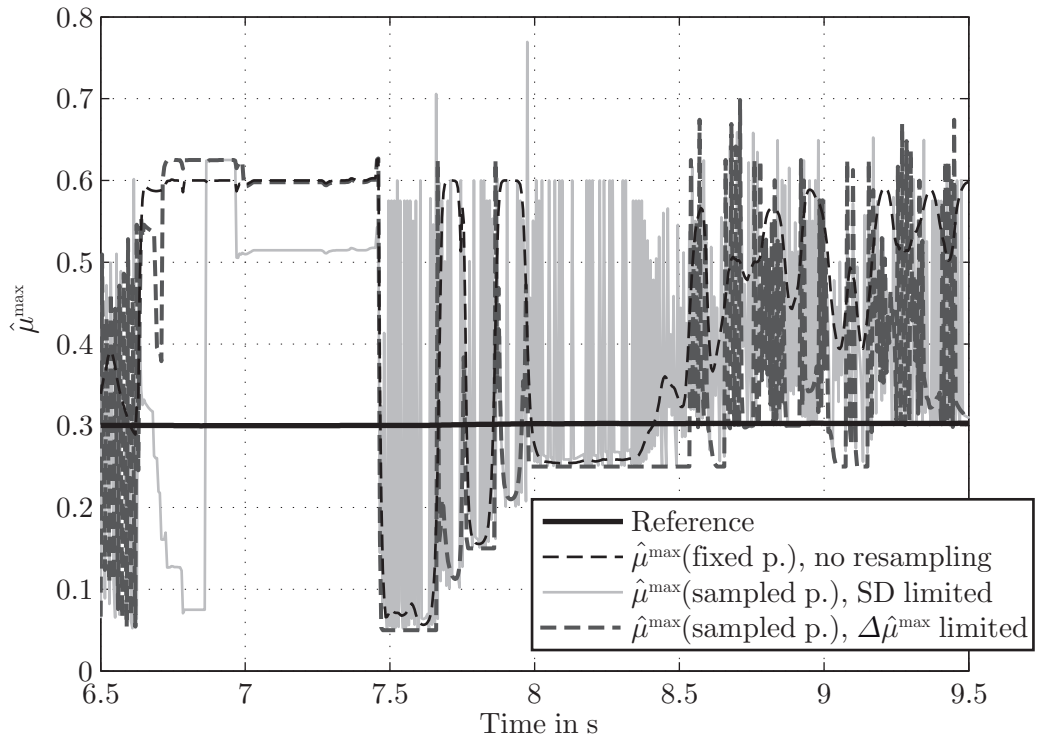


Figure 6.13.: Estimates of μ^{\max} using fixed particles (black dotted), variable particles re-initialised based on SD (light gray) or variable particles re-initialised based on $\Delta\hat{\mu}^{\max}$ (dark gray) versus time during a braking manoeuvre with a maximum deceleration of $\approx -3 \text{ m/s}^2$. A μ split manoeuvre is performed. The result for the rear left wheel is displayed, which was located on a low-friction surface ($\mu^{\max} \approx 0.3$).

detect high μ^{\max} with low dynamic excitation, as can be seen in Figure 6.15. The comparison of the error values shown in Table 6.2 supports the statement that low-friction conditions can be estimated more accurately. For low-friction conditions, the MAE is below 0.2 for all methods, whereas for dry roads the MAE is about 0.65.

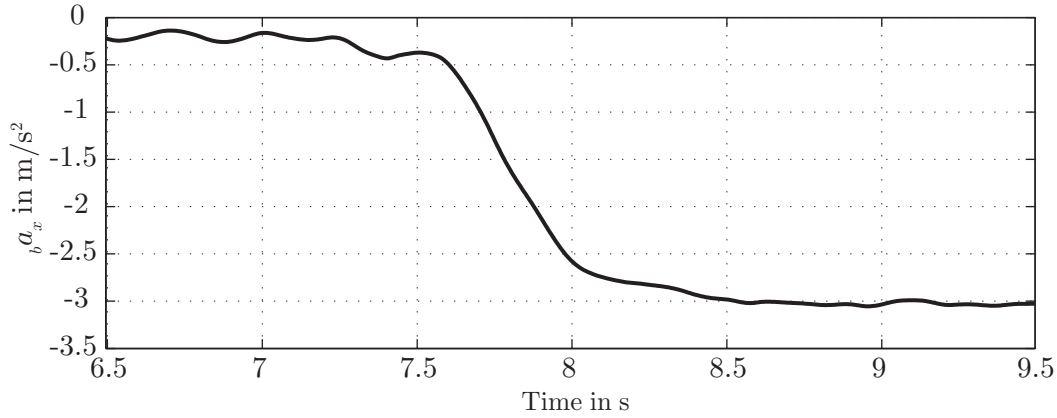


Figure 6.14.: Longitudinal acceleration $b a_x$ during braking manoeuvre on μ split conditions with a maximum deceleration $b a_x \approx -3 \text{ m/s}^2$. The manoeuvre was started at $v_x = 30 \text{ km/h}$ and ended at 10 km/h .

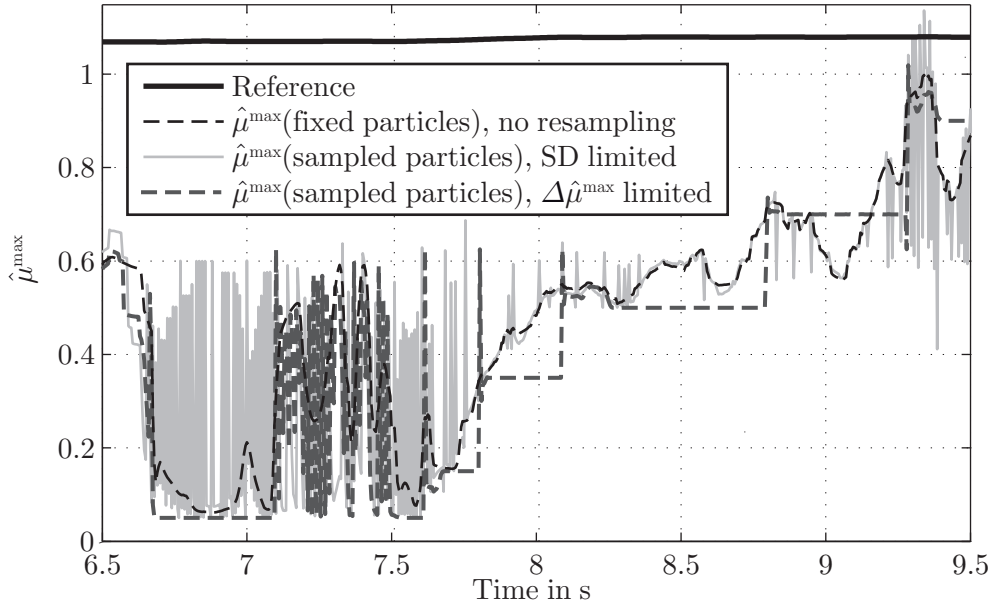


Figure 6.15.: Estimates of μ^{\max} using fixed particles (black dotted), variable particles re-initialised based on SD (light gray) or variable particles re-initialised based on $\Delta\hat{\mu}^{\max}$ (dark gray) versus time during a braking manoeuvre with a maximum deceleration of $\approx -3 \text{ m/s}^2$. A μ split manoeuvre is performed. The result for the rear right wheel is displayed, which was located on a high-friction surface ($\mu^{\max} \approx 1$).

6.5. Comparison of results with requirements of an AEB

The aim of the presented algorithm is to provide an estimate of the friction potential for adapting the intervention strategy of an AEB, cf. Section 1.3.2. By having an estimate before a possibly critical situation is being detected by the system, different intervention strategies can be evaluated (e.g. braking or steering) and warning and activation times as well as the magnitude of deceleration during the braking phases can be adapted on the current friction potential. The proposed algorithm depends on the dynamic excitation during the manoeuvre, thus a phase with e.g. partial braking during the AEB intervention will deliver better estimates than a low dynamic driving state before AEB may be necessary. However, this information is available only very late in terms of adapting the intervention strategy.

Figure 1.8 in Section 1.3.2 shows the relation between the tolerable deviation $\Delta\mu$ and the time delay τ_M for two different friction potentials in order to not exceed a certain impact speed when approaching a standstill object. When not considering a time delay τ_M , the tolerable deviation $\Delta\mu$ can be expressed as a function of the reference value μ^{ref} and the initial speed $v_{x,0}$ for the same requirements in terms of maximum impact speed, [LKE13a]. Figure 6.16 shows the limits for $\Delta\mu$ in dependence of μ^{ref} and $v_{x,0}$.

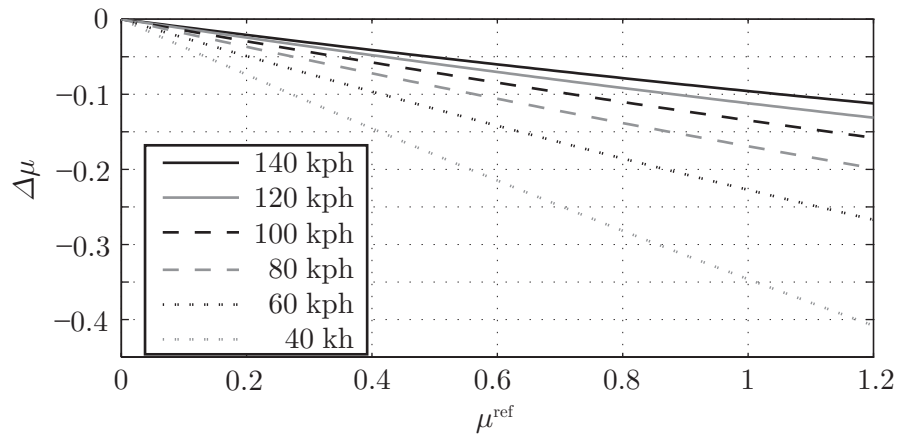


Figure 6.16.: Tolerable deviation $\Delta\mu$ in dependence on the real value μ^{ref} of the friction potential and for different initial longitudinal speed $v_{x,0}$, [LKE13a]

The error results in Table 6.1 and Table 6.2 show that for many conditions, an MAE below 0.2 can be achieved, which fulfils the requirements of an estimate of μ^{max} for inner-city speeds up to a reference road condition of $\mu^{\text{ref}} \approx 0.4$. Since current AEB

are designed for dry roads, cf. Section 1.3.2, the adaptation to low-friction surfaces is especially interesting. The results in Section 6.3 support the idea that the identification of low-friction surfaces is more accurate than that of dry conditions for a given dynamic excitation of $b a_x$.

It has to be mentioned that the work of *Lex et al.*, [LKE13b], was based on the same assumptions concerning the requirements for application in an AEB and, in addition, was based on the exact same measurement data that has been used within this work. Using ANNs, see Section 2.2.2, the achieved estimation results are comparable to those achieved with the particle filter presented within this chapter. For summer tire data, the MAE was given between 0.17 and 0.22 for the four tires, [LKE13b], which is comparable to the results in Table 6.1 and Table 6.2. Nevertheless, it has to be mentioned that a direct comparison of the two results is only legitimate for a rough evaluation. Whereas the MAE shown by *Lex et al.*, [LKE13b], count for a larger amount of measurement data, the resulting MAE shown in this work only count for individual measurements.

6.6. Discussion and outlook

The results of the sensitivity analysis in Section 4 suggest that it is worth focusing on the wheel dynamics or wheel-related variables rather than the vehicle's body reaction. This statement is directly supported by other works such as *Rajamani*, [RPPL12], and indirectly supported by the existence of much research that focuses on the horizontal tire forces or the longitudinal slips and the side slip angles, cf. Section 2.2.2. In this work, the wheel's angular momentum was used to calculate the expected longitudinal tire forces $F_{x,i}$. The results presented in this chapter suggest that the proposed observer based on a particle filter can fulfill the requirements of an AEB in certain driving states. This is especially true for inner-city applications, as the requirements for an estimate of the friction potential are relatively low at these v_x , cf. Figure 6.16.

In particular, the particle filter with resampling and using $\Delta\mu_{\max}$ within the re-initialisation strategy is promising, as the result is not too noisy yet still converges quickly. The estimate of the friction potential itself only depends on the variable particles. The fixed particles are only used to detect when re-initialisation is necessary. In order to ensure that the estimated value gets closer to the real value of the friction potential, the limit of $\Delta\mu_{\max}$ has to be optimized. Due to the nature of the proposed method, the influence of the road and the tire condition are estimated inseparably. Therefore,

6 Results and conclusion

tire wear and ageing may also be identified as effects that decrease the transmittable tire forces and thus the friction potential.

However, before series application can be considered, further investigations are necessary. In particular, this includes a robust and accurate determination of the longitudinal slip s_x , which was only possible using measurements of the longitudinal velocity v_x based on a GNSS-supported inertial measurement platform and resetting each wheel's effective tire radius. Apart from the dynamic excitation during driving, it is the accuracy of s_x that limits the proposed approach. Another promising approach that is worth testing is to estimate s_x and μ^{\max} simultaneously, as discussed in Section 5.3. In addition, there is room for improvement in the determination of the wheel torque $M_{D,i}$. To guarantee robustness and accuracy under many driving states, additional investigations are essential.

Optimizing parameters of the particle filter (e.g. by using other resampling strategies or adapting the proposed re-initialisation strategies) will likely further reduce the estimation error. In addition, current plans call for the development and testing of a real-time implementation of the proposed algorithm.

The results presented in this chapter have to be extended by investigations, including more measurement data for each of the driving and road conditions discussed. Although there are no theoretical objections, the proposed algorithm also has to be tested with real measurements of cornering manoeuvres, with other tire types and within a higher range of dynamic excitations. Furthermore, the estimation of a global friction potential was not demonstrated with measurement data. In addition, the algorithm is currently limited to even roads. Although it would be very easy to implement a road slope and inclination within the observer model, reliable and robust estimates are necessary. The same applies to the consideration of wind forces. Vertical excitation by the road is not intended to be considered with the simplified model. However, it is also important to recognise that the proposed approach has the potential to contribute to a sensorfusion system.

Extending the proposed algorithm by including the lateral tire characteristics and observing μ^{\max} based on the side slip angles α_i similar to Ray, [Ray97], or based on the self-aligning torque shows promise for improving the estimation accuracy for lateral driving states. However, this was beyond the scope of this work, as it was assumed that estimating μ^{\max} based on longitudinal driving states is more difficult due to the slow vehicle's response compared to the lateral direction. In addition, it is the more likely

driving state prior to an AEB intervention, which was the targeted ADAS.

7. Summary

According to the relevant literature, advanced driver assistance systems (ADAS) provide a high potential to increase road safety and are therefore the focus in the European white paper on road safety for 2020. The warning and activation strategies of ADAS could be significantly improved by the knowledge of two basic parameters. First, knowledge about the driver behaviour in the pre-collision phase can be used to optimally plan further ADAS interventions. This includes the prediction of whether or not the driver reacts to an ADAS warning and, in case the driver intervenes, it depends on whether it is a braking or steering input, for example. Secondly, the conditions of the road surface and the mounted tires limit the transmittable forces between tire and road and thus also the inputs to steering system, powertrain or braking system performed either by the driver and/or an ADAS. Currently, ADAS are designed to meet requirements for dry road, in order to avoid false interventions and reduce missed interventions. Enhancing the activation strategy of an ADAS by an estimate of the current road and tire conditions increases the potential to avoid an accident or reduce the injury severity when an accident is inevitable on low friction surfaces. Studies have shown that an additional potential to avoid an accident or reduce the injury severity when an accident is inevitable can be reached by adapting the ADAS intervention strategy to the current road condition. This potential increases with decreasing maximum coefficient of friction between tire and road, which is referred to as friction potential. The present thesis dealt with methods that identify the current friction potential in a fast, reliable and sufficiently accurate way.

An algorithm was developed to estimate the friction potential between tire and road, which is the primary indicator for the road and tire conditions. By using an automated emergency braking system (AEB) as an application case, requirements for the estimate were defined. One requirement is the accuracy of the friction potential estimate, which limits the ability to adapt the activation strategy. In addition, vehicle states that are most sensitive to a change of the road and tire condition were identified, as they promise to contribute to an observer of a friction potential estimate. The algorithm developed based on these prior investigations, which is mainly based on signals from standard

sensors of a vehicle equipped with electronic stability control (ESC), also require some information about vehicle and tire parameters.

The **first chapter** (*Introduction*) of this thesis discussed the significance of the friction potential to enhance traffic safety. The influence of the road conditions on the number of accidents was shown, and possible traffic safety measures were discussed. Thereafter, the importance of the friction potential for ADAS and vehicle dynamic controls (VDC) were shown, with an emphasis on the requirements for an estimate of the friction potential for selected applications. Finally, the AEB was selected as an exemplary application case to adapt the intervention strategy based on an estimate of the friction potential.

The **second chapter** (*Estimation of the friction potential*) presented the main factors that influence the friction potential, as well as the state of the art for existing estimation methods. After a brief definition of the friction potential, the basics of rubber physics and the relevant effects on the rotating wheel were discussed. An overview was given of the factors that influence the friction potential. Main effects (e.g. road surface, intermediary layers, tire's vertical load and vehicle's longitudinal velocity) were discussed in more detail. Next, there was a brief discussion of the wide variety of methods published in the research area of tire/road friction estimation, with a focus on vehicle-dynamics-based methods. Within these approaches, methods using a Bayesian observer framework such as the Kalman filter or the particle filter were emphasized.

The **third chapter** (*Vehicle model*) comprised a description of the vehicle model that was used throughout this thesis for both the sensitivity analysis in Chapter 4 and (partially) for the observer model presented in Chapter 5. In a first step, the required model complexity was investigated in order to be able to model the tire/road contact as accurately as possible but keeping in mind the computational effort. Thus, the influence of the model complexity of certain sub-systems on the model accuracy was evaluated using a validated vehicle model with 14 degrees of freedom and certain driving manoeuvres. Based on the results of this investigation, a vehicle model with 7 degrees of freedom was then chosen, which was presented along with the tire model used. Pitch and roll motion are neglected within the chosen vehicle model, but tire load distribution during braking, accelerating and cornering is included by considering the horizontal accelerations in the vehicle's COG.

In the **fourth chapter** (*Sensitivity analysis*), a mathematical solution to the problem

of identifying state variables that contribute to the estimation of the friction potential is presented. Unlike most of the published friction estimation approaches that use heuristic strategies, a sensitivity analysis was performed on a vehicle model described by ordinary differential equations (ODE) in order to identify the state variables that show a high sensitivity with respect to a change of the friction potential. To this end, different manoeuvres were simulated to cover longitudinal and lateral accelerations that are within physically possible limits and in a range in which vehicles are frequently driven. The results of these analyses showed that, independent of the longitudinal and lateral acceleration, the wheel's rotational speed have the highest sensitivity to a change in the friction potential. As the dynamic response of the body to a driver input is slow compared to the wheel's reaction, the state variables describing the vehicle body's state are omitted for estimation of the friction potential within the present thesis.

The **fifth chapter** (*Tire/road friction estimator*) includes the main part of this thesis, which is the presentation of the observer used to estimate the friction potential during driving. First, a general introduction to the particle filter, which is an observer within the Bayesian framework, was given. It enables the observation of non-linear internal states that are difficult or impossible to measure and is also able to deal with measurements that are subject to noise and inaccuracies. Second, the system model to be observed was presented, which was chosen based on the results of the sensitivity analysis. Using the wheel's angular momentum, the longitudinal tire forces of all four wheels are calculated. Within the particle filter, these are then compared to hypothetical longitudinal tire forces that are calculated for different values of the friction potential. In a third part of this chapter, information on signal processing of the measurement inputs was offered, as well as a discussion of the challenges to achieving the necessary signal quality. It was demonstrated that the accuracy with which the wheel's longitudinal slip can be calculated is the main limiting factor for the proposed estimation procedure. Among other values, the vehicle's longitudinal velocity is required to calculate the longitudinal slip. To achieve the required accuracy of the velocity measurement, velocity signals from global navigation satellite system (GNSS) combined with inertial measurements had to be used, in addition to ESC standard sensors. The velocity estimator was not part of this thesis.

The **sixth chapter** (*Results and conclusion*) applied the estimation results obtained using the proposed observer to real vehicle measurements. Different driving states were investigated, including accelerating and braking, as well as changing road conditions (μ

7 Summary

step) and different road conditions on the left and right wheels (μ *split*). In addition, different strategies for re-initialising particles after convergence were discussed in terms of noisiness and estimation accuracy. The results show that for a range of driving states, especially urban applications, the estimate of the particle filter is accurate enough to be used in an AEB. In general, the accuracy of an estimate of the friction potential increases with a longitudinal acceleration that is closer to the physical limits. For example, this is the case during acceleration and deceleration manoeuvres with high longitudinal accelerations, as well as when driving on surfaces with lower friction potential. In the case of a certain value of a longitudinal acceleration, lower friction potentials are easier to be identified than dry conditions.

The present thesis has introduced a novel method for the identification of the current friction potential that will have valuable benefit when used to enhance the activation strategies of advanced driver assistance systems, such as AEB systems. In order to achieve the necessary reliability for automotive applications, it is recommended that this approach be combined with other methods that are not based on vehicle dynamics in a sensorfusion system. Nevertheless, it is important to recognise that the proposed approach has the potential to contribute to a sensorfusion system. Compared to identification methods that are not based on vehicle dynamics (e.g. measuring precipitation type or thickness, infrastructure-aided systems), the proposed approach makes it possible to observe the tire condition in combination with the road condition, which also enables the detection of an influence on the friction potential (e.g. tire wear and ageing). The proposed identification method is also suitable for identifying the friction potential during combined longitudinal and lateral excitation, since combined tire forces are considered. In principal, lateral tire forces could also be used for friction estimation with the proposed approach, although the observed model would clearly need to be adapted. Nevertheless, the proposed algorithm seems to be accurate enough to be applied in an ADAS such as the AEB for urban applications, as well as for the detection of lower friction potentials than dry road during typical driving states.

A. Friction potentials in literature

Table A.1.: Ranges for the friction potential for different road conditions based on a literature review by Barace, [Urd12, p.50-51]

Road Conditions ^a	Bachmann ^b	Mundl ^c	Gustafsson ^d	Mitschke ^e	PC Crash ^f	Barace ^g
Asphalt, dry	1.05 - 1.2	1.05	1	0.88 - 1.15	0.7 - 0.9	0.9 - 1.2
Concrete, dry	-	-	-	-	-	-
Cobblestone, dry	-	-	-	-	-	-
Gravel, dry	-	0.5 ^h	0.5	-	-	0.5
Asphalt, wet	0.73 - 0.81	0.85	0.7	-	0.5 - 0.7 (wet) 0.4 - 0.5 (very wet)	0.7-0.9 0.65 - 0.8
Concrete, wet Σ	0.66 - 0.8	-	-	0.7 - 0.95	-	-
Asphalt, sandy	-	-	-	-	-	0.5 ⁱ
Asphalt, snow	-	0.2	0.3	-	0.1 - 0.5	0.2 - 0.3
Asphalt, ice (scattered)	0.18 - 0.38 ^j	-	-	0.07 - 0.2	0.05 - 0.25	0.1 - 0.2
Asphalt, ice	-	0.1	0.1	-	-	-

^aCategories according to ZEDATU, [TS06]

^b[Bac98, p.62-64]

^c[Mun12, H2 p.35]

^d[Gus97]

^e[MW04, p.19]

^f[SM01]

^g[Urd12, p.50-51]

^hMean value for loose gravel

ⁱAssumed to be in the range of gravel

^jharsh ice

B. Tire model *TMsimple* and tire dynamics

This section provides additional information about the tire model presented in Section 3.3. This includes the relationship between the *TMsimple* parameters K , B and A and physically describable tire characteristics, as well as an approach to calculate the time function τ_y for lateral tire dynamics.

B.1. Parameter relationships between static tire model

Within the tire model *TMsimple*, the parameters K , B and A show a dependence on parameters that can be described by physical relations. The three influencing parameters are the peak value Y_{\max} , the saturation value Y_{∞} and the initial stiffness dY_0 , which are shown in Figure B.1 for a constant tire load. The required *TMsimple* parameters read

$$\begin{aligned} K &= Y_{\max}, \\ B &= \pi - \arcsin\left(\frac{Y_{\infty}}{Y_{\max}}\right), \\ A &= \frac{1}{dY_0} \cdot K \cdot B \quad \text{with} \quad Y_{\infty} \leq Y_{\max}. \end{aligned} \tag{B.1}$$

To include the dependence of the tire forces on the friction potential, the extension

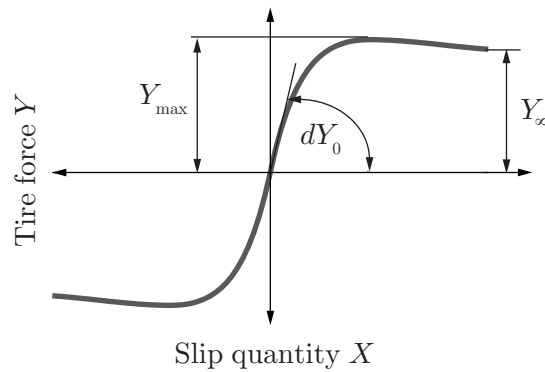


Figure B.1.: Physical relation of lateral tire parameters and the lateral tire characteristics in *TMsimple* for a constant tire load F_z , [Hir09a].

proposed by *Hirschberg et al.* as shown in Equation B.3 is used, [HRW07]. This is done by adjusting the maximum force Y_{\max} and the saturation force Y_{∞} by the proportional factor $\frac{\mu^{\max}}{\mu_0}$, where μ_0 is the nominal value of the friction potential for which the respective tire parameters have been measured. The initial stiffness dY_0 remains unaltered.

$$\begin{aligned}
 Y_{\max}(F_z) &= \left(a_1 \frac{F_z}{F_{z,nom}} + a_2 \left(\frac{F_z}{F_{z,nom}} \right)^2 \right) \cdot \frac{\mu^{\max}}{\mu_0} \\
 dY_0(F_z) &= b_1 \frac{F_z}{F_{z,nom}} + b_2 \left(\frac{F_z}{F_{z,nom}} \right)^2 \\
 Y_{\infty}(F_z) &= \left(c_1 \frac{F_z}{F_{z,nom}} + c_2 \left(\frac{F_z}{F_{z,nom}} \right)^2 \right) \cdot \frac{\mu^{\max}}{\mu_0}
 \end{aligned} \tag{B.2}$$

The coefficients a_1 to c_2 in Equation B.3 are needed to consider the decreasing influence of the tire load F_z on the horizontal tire forces. These coefficients depend on measured values for the nominal tire load $F_{z,nom}$ and the doubled nominal tire load $2 \cdot F_{z,nom}$. The values for a_1 and a_2 are given, for example, by

$$\begin{aligned}
 a_1 &= 2 \cdot Y_1 - \frac{1}{2} Y_2 \quad \text{and} \\
 a_2 &= -Y_1 + \frac{1}{2} Y_2,
 \end{aligned} \tag{B.3}$$

with $Y_1 = Y_{\max}(F_{z,nom})$ and $Y_2 = Y_{\max}(2 \cdot F_{z,nom})$ at $2 \cdot F_{z,nom}$. Accordingly, the coefficients b_1 and b_2 are calculated using the respective initial stiffness values, and c_1 and c_2 are calculated using the respective saturation values.

B.2. Modelling time function τ_y

When a rolling tire is being steered, the time until a lateral tire contact force is built up can be described by a first order system, as shown in Section 3.3.2. According to *Rill*, the time function τ in Equation 3.29, which describes the dynamic processes that occur in the contact patch, depends on two factors, [Ril06]. The first factor is the transport velocity $r_e \cdot |\omega_r|$ with which the particles in the tire tread are moving through the contact patch. The second factor is the relaxation length r_{α} that describes the distance that a particle in the tire tread travels from when a change of α occurs until the full force is built up. The time function τ is given by

$$\tau = \frac{r_{\alpha}}{r_e \cdot |\omega_r|}. \tag{B.4}$$

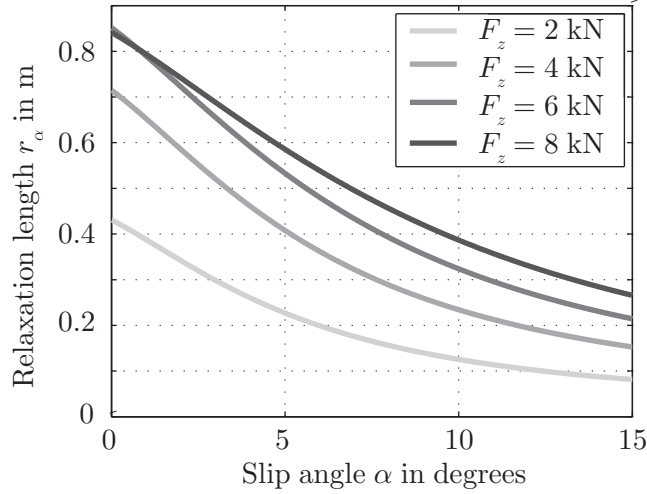


Figure B.2.: Relaxation length for the tire described in Appendix D with $c_{T,y} = 100000$ N/m at a transport velocity $v_e \cdot |\omega_r| = 60$ km/h computed according to *Rill*, [Ril06]. Tire damping d_y is omitted.

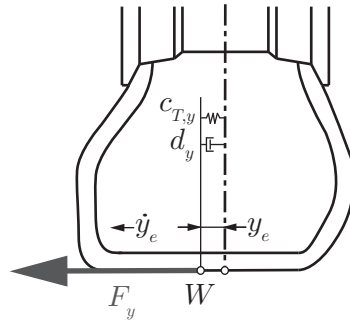


Figure B.3.: Lateral tire deflection y_e caused by the lateral force F_y , [Ril06]

The relaxation length r_α is a function of the wheel load F_z and the slip angle α , as shown in Figure B.2. It increases with higher F_z and decreases with higher α , [dJ00, p.33]. However, since measurements of r_α are not available for the investigated tires, the following approach is used to model τ . A lateral tire force acting in the contact patch causes a lateral deflection y_e , see Figure B.3. A first order approximation considering y_e is given by *Rill*, [Ril06], and reads

$$F_y^D \approx F_y + \frac{\partial F_y}{\partial v_y} \dot{y}_e. \quad (\text{B.5})$$

With the lateral stiffness $c_{T,y}$ and the lateral damping coefficient d_y of the tire, the

dynamic force F_y^D is given with

$$F_y^D = c_{T,y} \cdot y_e + d_y \cdot \dot{y}_e. \quad (\text{B.6})$$

The partial derivative of the lateral force F_y with respect to the lateral velocity v_y in the contact point can be calculated with

$$\frac{\partial F_y}{\partial v_y} = \frac{\partial F_y}{\partial s_\alpha} \frac{\partial s_\alpha}{\partial v_y} = \frac{\partial F_y}{\partial s_\alpha} \frac{-1}{r_e \cdot |\omega_r|}, \quad (\text{B.7})$$

including an alternative definition of the lateral slip s_α which is related to the side slip angle by $s_\alpha = \tan \alpha$, [Ril06]. According to *Rojas Rojas*, the partial derivative of the lateral tire force with respect to the slip angle α can be approximated by their global derivatives for small values of α , [Roj12, p.29], and hence reads

$$\frac{\partial F_y}{\partial s_\alpha} \approx \frac{F_y}{s_\alpha}. \quad (\text{B.8})$$

Inserting Equations B.6, B.7 and B.8 in Equation B.5 gives

$$\frac{1}{c_{T,y}} \cdot \left(\frac{F_y}{s_\alpha} \frac{1}{r_e \cdot |\omega_r|} \right) \cdot \dot{y}_e + y_e = \frac{F_y}{c_{T,y}}, \quad (\text{B.9})$$

including the term before \dot{y}_e , which gives a formulation of τ that can be used in the simulation model. Thus, the time function ultimately reads

$$\tau = \frac{1}{c_{T,y}} \cdot \left(\frac{F_y}{s_\alpha} \frac{1}{r_e \cdot |\omega_r|} \right). \quad (\text{B.10})$$

C. Vehicle model structure for sensitivity analysis

The structure of the dependencies between the state variables, the inputs and the investigated parameters of the vehicle model derived in Section 4.1 is helpful to solve the ODE of the sensitivity system. The differential equations of the vehicle model in Equation 3.6 are extended by the differential state equations of the lateral tire forces in Equation 3.29.

Table C.1.: Relation between state variables at the current time step k and the previous time step $k - 1$ in the vehicle model adapted for the sensitivity analysis

	State variables \mathbf{z}_k											$\dot{\mathbf{z}}_{k-1}$	
	v_x	v_y	$b\dot{\omega}_z$	$\dot{\omega}_{fl}$	$\dot{\omega}_{fr}$	$\dot{\omega}_{rl}$	$\dot{\omega}_{rr}$	$F_{y,fl}^D$	$F_{y,fl}^D$	$F_{y,fl}^D$	$F_{y,fl}^D$	$\dot{v}_x(k-1)$	$\dot{v}_y(k-1)$
\dot{v}_x	x	x	x	x	x	x	x	x	x	x	x	x	x
\dot{v}_y	x	x	x	x	x	x	x	x	x	x	x	x	x
$b\dot{\omega}_z$	x	x	x	x	x	x	x	x	x	x	x	x	x
$\dot{\omega}_{fl}$	x	x	x	x								x	x
$\dot{\omega}_{fr}$	x	x	x		x							x	x
$\dot{\omega}_{rl}$	x	x	x			x						x	x
$\dot{\omega}_{rr}$	x	x	x				x					x	x
$\dot{F}_{y,fl}^D$	x	x	x	x				x				x	x
$\dot{F}_{y,fr}^D$	x	x	x		x				x			x	x
$\dot{F}_{y,rl}^D$	x	x	x			x				x		x	x
$\dot{F}_{y,rr}^D$	x	x	x				x				x	x	x

C Vehicle model structure for sensitivity analysis

The structure of the differential equation for time step k can then be represented as

$$\dot{\mathbf{z}}(k) = \mathbf{M}^{-1} \cdot (\mathbf{q}(\mathbf{z}(k), \mathbf{z}(k-1), \delta_i(k), M_{D,i}(k), \mu_i^{\max}(k)) - \mathbf{k}(\mathbf{z}(k))). \quad (\text{C.1})$$

with $\mathbf{k} = f(\mathbf{z}(k)) = f(v_x, v_y)(k)$ and the inputs for \mathbf{q} which are the wheels' steering angles $\delta_i(k)$, the wheels' driving and braking torques $M_{D,i}(k)$ and the friction potential $\mu_i^{\max}(k)$. The dependency on \mathbf{q} and $\dot{\mathbf{z}}(k-1)$ originates from the simplifications in the calculation of the tire load variation and the effective tire radius, see Section 4.3. A systematic overview of the dependencies is given in Table C.1 and C.2.

Table C.2.: Relation between state variables and the inputs as well as the friction potentials in the vehicle model adapted for the sensitivity analysis

	Inputs						Parameter μ^{\max}			
	$\delta_{fl}(k)$	$\delta_{fr}(k)$	$M_{D,fl}(k)$	$M_{D,fr}(k)$	$M_{D,rl}(k)$	$M_{D,rr}(k)$	$\mu_{fl}^{\max}(k)$	$\mu_{fr}^{\max}(k)$	$\mu_{rl}^{\max}(k)$	$\mu_{rr}^{\max}(k)$
\dot{v}_x	x	x					x	x	x	x
\dot{v}_y	x	x					x	x	x	x
$b\dot{\omega}_z$	x	x					x	x	x	x
$\dot{\omega}_{fl}$	x		x				x			
$\dot{\omega}_{fr}$		x		x				x		
$\dot{\omega}_{rl}$					x				x	
$\dot{\omega}_{rr}$						x				x
$\dot{F}_{y,fl}^D$	x						x			
$\dot{F}_{y,fr}^D$		x						x		
$\dot{F}_{y,rl}^D$									x	
$\dot{F}_{y,rr}^D$										x

C.1. Numerical implementation of vehicle model for automatic differentiation

To calculate the Jacobian \mathbf{J} and the derivative \mathbf{f}_c using AD, the vehicle model has to be at least one time differentiable. To achieve at least weak derivatives, numerical approximations were necessary for the following two unsteady functions.

C.1.1. Find maximum out of two values

Within the calculation of the longitudinal slip, see Equation 2.3, it is necessary to select the bigger variable out of two variables u and w . This function is discontinuous at the transition between u and w . The derivable numerical approximation given by

$$\max(u, w) = \frac{w}{2} \cdot \left(1 + \frac{2}{\pi} \cdot \arctan((w - u) \cdot \epsilon)\right) + \frac{u}{2} \cdot \left(1 + \frac{2}{\pi} \cdot \arctan((u - w) \cdot \epsilon)\right) \quad (\text{C.2})$$

is used instead. The accuracy can be increased by the factor ϵ which was set at 10^5 within the simulation.

C.1.2. Absolute value

Calculating an absolute value of a variable w is necessary for several calculations (e.g. the longitudinal slip with Equation 2.3). As conditional programming (e.g. *if statements*) are also not supported within *Adimat*, the formulation

$$|w| = \sqrt{w^2} \quad (\text{C.3})$$

is used. Although this formulation is still discontinuous at zero, it can be used within *Adimat*, as it is a weak derivative.

D. Vehicle and tire model parameters

The tire and vehicle parameters presented in Tables D.1 and D.2 are valid for both the investigation of the model complexity in Section 3.1 and the initial validation of the vehicle model in Section 3. They have been validated in previous projects using a multi-body vehicle model (the same one used in Section 3.1 to select the model complexity) and by using measurement data from an *Opel Combo 1.6 CNG*, [Roj12, p.13-15]. The sensitivity analysis was conducted with validated parameters of an *Audi A4 Avant 1.8 Tfsi* that was also used for all measurements for the observer, as presented in Section 6. The tire and vehicle parameters of the Audi are presented in Tables D.3 and D.4.

Table D.1.: *TMsimple* tire model parameters for a summer tire of type Radial 185/60 R15, as given by *Rojas Rojas*, [Roj12, p.203]

	Parameter	Symbol	Value		Unit
			$F_{z,nom}$	$2 \cdot F_{z,nom}$	
Long.	Peak	$Y_{max,x}$	2740	5480	N
	Saturation	$Y_{\infty,x}$	2130	4350	
	Initial stiffness	$dY_{0,x}$	430	1100	N/%
Lat.	Peak	$Y_{max,y}$	2720	4990	N
	Saturation	$Y_{\infty,y}$	2600	4700	
	Initial stiffness	$dY_{0,y}$	51600	80200	N/rad
	Longitudinal spring stiffness	$c_{T,x}$	200000		N/m
	Lateral spring stiffness	$c_{T,y}$	100000		
	Vertical spring stiffness	$c_{T,z}$	200000		
	Nominal tire load	$F_{z,nom}$	2500		N
	Nominal friction potential	μ_0	1		-
	Rolling resistance coefficient	f_r	0.01		-
	Unloaded tire radius	r_0	0.3159		m

D Vehicle and tire model parameters

Table D.2.: Vehicle model parameters of *Opel Combo 1.6 CNG*, as identified by *Rojas Rojas*, [Roj12, p.202], except for the value of the wheel mass m_w , which is from a separate measurement.

Parameter	Symbol	Value	Unit
Vehicle Mass	m_b	1320	kg
Vehicle's principal moment of inertia (around z axis)	I_z	2000	kg m ²
Wheel base	l_{wb}	2.716	m
Front track	t_f	1.417	m
Rear track	t_r	1.44	m
Distance centre of gravity to front axle	l_f	1.3	m
Height of centre of gravity (from ground)	h_{CG}	0.65	m
Height of instantaneous centre of the pitch movement	$h_{IC,\theta}$	0.3	m
Height of instantaneous centre of the roll movement	$h_{IC,\phi}$	0.3	m
Projected frontal area	A_p	2.3	m ²
Drag coefficient	c_D	0.35	-
Wheel mass	m_w	15	kg
Linear spring stiffness (front axle)	$c_{S,f}$	30000	N/m
Linear spring stiffness (rear axle)	$c_{S,r}$	42000	N/m
Anti-roll bar stiffness (front axle)	$c_{ARB,f}$	40000	N/m
Anti-roll bar stiffness (rear axle)	$c_{ARB,r}$	10000	N/m
Wheel's principal moment of inertia (around y_C axis)	I_i	2	kg m ²

Table D.3.: *TMsimple* tire model parameters for the summer tire of type Radial 245/40 R18 that was mounted on the test vehicle (Audi A4 Avant 1.8 Tfsi) during the measurements. All values were measured on a tire test bench, except $c_{T,x}$ and $c_{T,y}$ which were taken from Table D.1 in the absence of other data.

	Parameter	Symbol	Value		Unit
			$F_{z,nom}$	$2 \cdot F_{z,nom}$	
Long.	Peak	$Y_{max,x}$	3789	6688	N
	Saturation	$Y_{\infty,x}$	2809	4890	
	Initial stiffness	$dY_{0,x}$	1963	3021	N/%
Lat.	Peak	$Y_{max,y}$	3766	6581	N
	Saturation	$Y_{\infty,y}$	3565	5898	
	Initial stiffness	$dY_{0,y}$	54028	94461	N/rad
	Longitudinal spring stiffness	$c_{T,x}$	200000		N/m
	Lateral spring stiffness	$c_{T,y}$	100000		
	Vertical spring stiffness	$c_{T,z}$	282000		
	Nominal tire load	$F_{z,nom}$	3000		N
	Nominal friction potential	μ_0	1		-
	Rolling resistance coefficient	f_r	0.01		-
	Unloaded tire radius	r_0	0.3266		m

D Vehicle and tire model parameters

Table D.4.: Vehicle model parameters of *Audi A4 Avant 1.8 Tfsi* based on measurements and the data sheet, [AG08]

Parameter	Symbol	Value	Unit
Vehicle Mass	m_b	1796	kg
Vehicle's principal moment of inertia (around z axis)	I_z	3006	kg m ²
Wheel base	l_{wb}	2.808	m
Front track	t_f	1.564	m
Rear track	t_r	1.551	m
Distance centre of gravity to front axle	l_f	1.337	m
Height of centre of gravity (from ground)	h_{CG}	0.549	m
Height of instantaneous centre of the pitch movement	$h_{IC,\theta}$	0.3	m
Height of instantaneous centre of the roll movement	$h_{IC,\phi}$	0.1	m
Projected frontal area	A_p	2.2	m ²
Drag coefficient	c_D	0.273	-
Rolling torque stiffness (front axle)	$c_{S,f}$	68500	N/m
Rolling torque stiffness (rear axle)	$c_{S,r}$	35780	N/m
Wheel's principal moment of inertia (around y_C axis)	I_i	1	kg m ²

E. Longitudinal velocity estimation

An accurate monitoring of the vehicle's longitudinal velocity v_x is necessary for the calculation of the longitudinal slips $s_{x,i}$ as described in Section 5.5.1. The following sections present different approaches to estimate v_x with the required accuracy. These approaches are divided into methods that only use the ESC sensors, in observer-based methods, in radar-based methods and in methods based on global navigation satellite system (GNSS). This classification is based on *Uchanski*, who mentions measuring or estimating v_x either by a vehicle speed observer, by using radar sensors or by using data from a , [Uch01, p.114]. The following sections also discuss promising solutions for automotive series-application regarding costs.

E.1. Estimation of the longitudinal velocity using only ESC sensors

The reference velocity v_x can be calculated using only the wheel speeds ω_i for certain driving states. With a free rolling wheel (e.g. when accelerating on a non-driven axle), a reference velocity v_x can be calculated for a known effective tire radius $r_{e,i}$. Nevertheless, at least one wheel has to be slip-free. This generally excludes all four-wheel driven vehicles and all vehicles during braking. An additional problem is the accuracy that can be reached. As mentioned by *Dieckmann*, [Die92, p.19-22, 110], it is possible to estimate s_x with a high resolution when the wheel rotational speeds are observed for several revolutions. Due to this principle, this only works when ω_i does not change quickly. In addition, the observed wheel needs to be slip-free, as mentioned above. Again, free rolling conditions have to be used for calibration to compensate for differences in the effective tire radius $r_{e,i}$ between front and rear axle, [Die92, p.110-111]. One promising idea is to estimate s_x simultaneously to μ^{\max} , as mentioned in Section 5.3. This is possible because the influences of μ^{\max} and $s_{x,i}$ are in different ranges of $F_{x,i}$, cf. [BZ07, p.84-86]. Nevertheless, this was not investigated, as this special focus was beyond the scope of this thesis.

E.2. Observer-based estimation of the longitudinal velocity

Several methods using observers to estimate the longitudinal velocity v_x or the wheels' slips $s_{x,i}$ directly are described in the literature. *Daiß and Kiencke* compared two different observers for estimating the wheel slip s_x with an accuracy of 1 % using sensors for the four wheel speeds, the longitudinal body acceleration and the vehicle's yaw rate, [DK95]. The use of a Kalman filter applied to a two-track vehicle model and Fuzzy logic showed similar results in terms of the accuracy of calculating s_x . Concerning computational and implementational effort, the Fuzzy logic approach seemed to be advantageous. Nevertheless, this accuracy is not sufficient for the present application.

Klomp et al. estimated both v_x and the road slope from measurements of the wheels' torques, the wheels' speeds and ${}_b a_x$ using a Kalman filter, [KGB14]. Only one wheel's velocity (usually the one with the lowest wheel slip) is used as an input. Therefore, it is necessary to detect high values of s_x robustly and early, which is a crucial part of the proposed algorithm. Experimental results on ice showed that the achieved estimate was between 5 % of the real v_x , except when the test started on a road slope of 10 %.

Imsland et al. propose a non-linear observer to estimate v_x and v_y based on signals of ${}_b a_x$, ω_z and ω_i , [IJF⁺05]. In a first step, v_x is estimated using mainly the wheel speeds, but also ${}_b a_x$ and ω_z . Then, v_y is estimated also using ${}_b a_y$ and δ_S . The basis is a two-track vehicle model used to describe the motion in the horizontal plane. Experimental results show some shortcomings on surfaces with low μ^{\max} . Nevertheless, results were only shown for highly dynamic manoeuvres and on a circle, which makes the estimation of accuracy in normal driving states difficult.

Tanelli only uses measurements of ${}_b a_x$ and ω_i to estimate v_x within a non-linear estimator, [TSC06]. It is assumed that the effective tire radii $r_{e,i}$ is known and ${}_b a_x$ is compensated by pitch effects. Road slope is not considered. At low vehicle speeds, constant vehicle speeds or soft accelerating or braking (e.g. ${}_b a_x < -0.8$ m/s), the mean of the four wheel speeds multiplied by their $r_{e,i}$ is used for v_x . When accelerating, only the wheel speeds of the non-driven wheels are used. Braking is the most critical driving state for estimation. In this state, the filtered ${}_b a_x$ is integrated using a discrete time integrator. Nevertheless, for a braking manoeuvre starting at about 30 kph and ${}_b a_x \approx 3$ m/s², the maximum error in estimating v_x was shown to be below 0.4 m/s.

Villagra et al. propose estimating v_x and v_y using ${}_b a_x$, ${}_b a_y$, ω_z and ω_i based on algebraic estimation approaches, [VdFM08]. To estimate only v_x , an estimate of v_y is also necessary. The sensitivity of the results to μ^{\max} seems to be low. It has to be mentioned that no vehicle parameters are necessary. Nevertheless, no experimental results were shown, but just experiments with simulated data.

Rajamani et al. discussed the estimation of v_x based on two different sensor combinations, [RPPL12]. For the first approach, the wheel speeds and an accelerometer are used to estimate v_x within an observer. Although this approach takes into account aerodynamic drag and estimating the climbing resistance, it showed some shortcomings in the form of under-damped estimation dynamics and was not suitable, according to the authors. The second approach is described within the GNSS-based approaches.

E.3. Radar-based estimation of the longitudinal velocity

Radar sensors are already available in vehicles equipped with adaptive cruise control (ACC). The necessary accuracy with which the relative velocity Δv_x to other objects (including stationary objects) has to be detected for ACC are ≤ 2 m/s or ≤ 3 % of Δv_x . This high accuracy of the relative velocity makes it possible to improve the on-board calculation of the vehicle's own velocity v_x , [WDS09, p.492]. The resolution with which the relative velocity Δv_x between the vehicle and another object can theoretically be measured depends on the measurement time T and the frequency range f_0 , [Win09b]. For automotive applications world-wide the transmitted frequency f_0 is most often 76.5 GHz. Given the light speed $c_L = 299792458$ m/s² and a typical measurement time $T = 0.04$ s, the theoretical resolution $\Delta \bar{v}_x$ of the relative velocity is

$$\Delta \bar{v}_x = \frac{c_L}{2 \cdot f_0 \cdot T} = \frac{299792458}{2 \cdot 76.5 \cdot 10^9 \cdot 0.04} \approx 0.05 \text{ m/s}, \quad (\text{E.1})$$

[Win09b]. As an example for the real achieved accuracy, the *Bosch LRR3* radar sensor currently used in series application for ACC has an accuracy of Δv_x of 0.1 m/s, [Win09b]. Nevertheless, this is the accuracy of the relative speed to other objects. It cannot be assumed that this high accuracy can also be achieved for the relative velocity between the vehicle and the road. This accuracy also depends on the mounting height of the sensor, the direction of the centre of the transmitted signal and especially on the reflection capability of the road. The reflection capability depends in general on the type of object, its geometry and its orientation. Metal objects (e.g. stationary objects such

as parked cars, sewer covers or traffic signs) have a better reflection capability than the road surface, for example. In addition, the road conditions influence the received signal power. In particular, the presence of water is limiting, since it diffuses the signal, [Win09b]. Nevertheless, for many driving states, a sensorfusion of radar-based velocity estimation with on-board sensors seems to be sensible for this application.

E.4. GNSS-based estimation of the longitudinal velocity

Global navigation satellite system (GNSS) is the umbrella term for existing satellite-based navigation infrastructures, such as the global positioning system (GPS) or Galileo, [WHW09b, p.677]. Starting in October 2015, it will be mandatory for new vehicles in the European Union to be able to automatically communicate with the European emergency call infrastructure system (eCall) after a severe accident (e.g. in case the driver is unconscious and unable to call an emergency service), [Dat14]. The data received by the emergency services include the time of the accident, the position of the vehicle, and its direction, which can be relevant on highways or in tunnels. The technical considerations for the vehicle's on-board system to be approved include the use of GNSS, [EotEC14]. Thus, it can be assumed that GNSS will be available in series production vehicles in the near future.

Belvy and Gerdes used GNSS velocity information to calculate the longitudinal slips $s_{x,i}$, slip angles α_i and the vehicle's side slip angle β , [BG00]. To calculate the wheel slip, the GNSS velocity was directly used in combination with the wheel speed sensors. During free rolling of the tires, they propose using the GNSS velocity to calibrate the wheel speed sensors' signals. The results showed high slip noise and an offset that could have been subject to miscalibration. Nevertheless, it was also shown that the noise was brought in by the wheel speed sensors rather than the GNSS velocity measurement. A similar approach was used by *Rajamani et al.*, [RPPL12], where s_x is calculated directly using the GNSS velocity and the wheel speeds.

Miller et al. used the GNSS velocity to estimate the effective tire radius and the longitudinal stiffness of the tires, [MYM⁺01]. Beyond calculating s_x directly using the GNSS velocity, it has been used to calculate the effective tire radius $r_{e,i}$ of non-driven wheels during free rolling within a sub-millimeter accuracy. Then, s_x was calculated using only the wheel speed measurements, which excludes estimation of braking conditions (other than engine braking) and for 4WD vehicles.

The standard GNSS receiver update is 1 Hz, which is sufficient for automotive navigation, [SZZ13], but not to determine the vehicle speed for the proposed application. Although technically feasible receiver rates go up to 200 Hz (e.g. for aeronautic applications), [SZZ13], these systems are not affordable for automotive series application. In addition, these rates only apply in ideal conditions (e.g. good satellite visibility). Especially in urban areas, GNSS outage is inevitable. In combination with measurements of the vehicle's state, both the calculation of position and velocity can be significantly improved and, in case of GNSS outage, also temporarily deliver v_x estimates without GNSS velocity. Many approaches can be found in literature to combine GNSS and inertial measurements, often by using a Kalman filter. For example, *Hide et al.* achieved good results for high-accuracy real-time navigation using a low-cost micro-electromechanical system (MEMS) as a sensor to measure accelerations and angular rates with an update rate of 100 Hz and a GNSS with a receiver update of 1 Hz with a Kalman filter, [HMS03]. Thus, combined with additional on-board sensor information, GNSS-velocity-based estimators show promising results.

Bibliography

- [AB09] B. Abendroth and R. Bruder. *Die Leistungsfähigkeit des Menschen für die Fahrzeugführung*, chapter 1, pages 4–14. Handbuch Fahrerassistenzsysteme Grundlagen, Komponenten und Systeme für aktive Sicherheit und Komfort. Vieweg+Teubner, 1. edition, 2009.
- [ABC⁺07] M. Andersson, F. Bruzelius, J. Casselgren, M. Gäfvert, M. Hjort, J. Hultén, F. Håbring, M. Klomp, G. Olsson, M. Sjö Dahl, J. Svendenius, S. Woxneryd, and B. Wälvaara. Road Friction Estimation. Technical report, Intelligent Vehicle Safety Systems (IVSS), 2007. Göteborg, Sweden.
- [AFBJ14] A. Albinsson, M. Jonasson F. Bruzelius, and B. Jacobson. Tire Force Estimation Utilizing Wheel Torque Measurements and Validation in Simulation and Experiments. In *Proceedings of the International Symposium on Advanced Vehicle Control*, pages 294–299, 2014. Tokyo, Japan.
- [AG08] AUDI AG. Technische Daten Audi A4 1.8 TFSI (118 kW). Available at http://www.audi.de/content/dam/ngw/product/used_cars/a4/pdf/a4b7/2008_09_a4_b7_18tfsi.pdf, 2008. Accessed on 14.7.2014.
- [APT09] C. Ahn, H. Peng, and H. E. Tseng. Estimation of road friction for enhanced active safety systems: Dynamic approach. In *Proceedings of American Control Conference (ACC)*, pages 1110–1115. IEEE Computer Society, 10-12 June 2009. St. Louis, Missouri, USA.
- [Bac96] T. Bachmann. *Literaturrecherche zum Reibwert zwischen Reifen und Fahrbahn*, volume 286. VDI Verlag, 1996.
- [Bac98] T. Bachmann. *Wechselwirkungen im Prozess der Reibung zwischen Reifen und Fahrbahn*, volume 360. VDI Verlag, 1998.
- [Bau07] R. Bauer. Zustandschätzung und Filterung. Lecture notes, Institute of Automation and Control, Graz University of Technology, 2007.

Bibliography

- [BBB⁺02] B. Breuer, M. Barz, K. Bill, S. Gruber, M. Semsch, T. Strothjohann, and C. Xie. The Mechatronic Vehicle Corner of Darmstadt University of Technology - Interaction and Cooperation of a Sensor Tire, New Low-Energy Disc Brake and Smart Wheel Suspension. *International Journal of Automotive Technology*, 3(2):63–70, 2002.
- [BBES94] B. Breuer, T. Bachmann, S. Ernesti, and J. Stöcker. Methods and Instruments for On-Board Measurement of Tyre/Road Friction. Sae technical paper 942470, Society of Automotive Engineers (SAE), 1994.
- [BBL⁺02] C. H. Bischof, H. M. Bückler, B. Lang, A. Rasch, and A. Vehreschild. Combining Source Transformation and Operator Overloading Techniques to Compute Derivatives for MATLAB Programs. In *Proceedings of the Second IEEE International Workshop on Source Code Analysis and Manipulation (SCAM)*, pages 65–72. IEEE Computer Society, 1 October 2002. Montreal, Canada.
- [BER92] B. Breuer, U. Eichhorn, and J. Roth. Measurement of tyre-road friction ahead of the car and inside the tyre. In *Proceedings of the International Symposium on Advanced Vehicle Control*, pages 347–353, 1992. Tokyo, Japan.
- [BG00] D.M. Bevly and J.C. Gerdes. The Use of GPS Based Velocity Measurements for Improved Vehicle State Estimation. In *Proceedings of the American Control Conference (ACC)*, pages 2538–2542. IEEE Computer Society, 28–30 June 2000. Chicago, Illinois, USA.
- [BH00] M. Bückler and P. Hovland. www.autodiff.org - Introduction. Available at <http://www.autodiff.org/?module=Introduction>, 2000. Accessed on 29.7.2014.
- [Bre09] J. Breuer. *Bewertungsverfahren von Fahrerassistenzsystemen*, chapter 6, pages 55–68. Handbuch Fahrerassistenzsysteme Grundlagen, Komponenten und Systeme für aktive Sicherheit und Komfort. Vieweg+Teubner, 1 edition, 2009.
- [BSY⁺10] F. Bruzelius, J. Svendenius, S. Yngve, G. Olsson, J. Casselgren, M. Andersson, J. Rönnerberg, and S. Löfving. Evaluation of Tire and Road Friction Estimators, Test Methods and Metrics. *International Journal of Vehicle Systems Modelling and Testing*, 5(2/3):213–236, 2010.

- [BZ07] B. Boßdorf-Zimmer. Nichtlineare Fahrzustandsbeobachtung für die Echtzeitanwendung. Dissertation thesis, 2007. Braunschweig University of Technology.
- [BZFHK07] B. Boßdorf-Zimmer, L. Frömmig, R. Henze, and F. Küçükay. Real-Time-Processing Vehicle State Estimation. In *Proceedings of chassis.tech*. Springer Vieweg, 1-2 March 2007. Munich, Germany.
- [CSST00] F. Campolongo, A. Saltelli, T. Sorensen, and S. Tarantola. *Hitchhiker's Guide to Sensitivity Analysis*, chapter 2, pages 14–50. Sensitivity Analysis. John Wiley and Sons, 2000.
- [Dat14] European Commission Press Release Database. eCall: automated emergency call for road accidents mandatory in cars from 2015. Available at http://europa.eu/rapid/press-release_IP-13-534_en.htm, 2014. Accessed on 4.12.2014.
- [Deu12] Statistisches Bundesamt Deutschland. *Verkehr. Verkehrsunfälle. 2011*, volume 8, Nr. 7. Statistisches Bundesamt Deutschland, 2012.
- [DG76] R. P. Dickinson and R. J. Gelinas. Sensitivity Analysis of Ordinary Differential Equation Systems - A Direct Method. *Journal of Computational Physics*, 21:123–143, 1976.
- [DGA00] A. Doucet, S. Godsill, and C. Andrieu. On sequential Monte Carlo sampling methods for Bayesian filtering. *Journal of Statistics and Computing*, 10(3):197208, 2000.
- [Die92] T. Dieckmann. Der Reifenschlupf als Indikator für das Kraftschlußpotential. Dissertation thesis, 1992. Hannover University.
- [dJ00] P. Van der Jagt. The Road to Virtual Vehicle Prototyping. new CAE-models for accelerated vehicle dynamics development. Dissertation thesis, 2000. Eindhoven University of Technology.
- [DK95] A. Daiß and U. Kiencke. Estimation of vehicle speed fuzzy-estimation in comparison with Kalman-filtering. In *Proceedings of the 4th IEEE Conference on Control Applications*, pages 281–284. IEEE Computer Society, 28-29 September 1995. Albany, New York, USA.

Bibliography

- [Don09] E. Donges. *Fahrerverhaltensmodelle*, chapter 2, pages 15–23. Handbuch Fahrerassistenzsysteme Grundlagen, Komponenten und Systeme für aktive Sicherheit und Komfort. Vieweg+Teubner, 1. edition, 2009.
- [DT10] N. Ding and S. Taheri. Application of Recursive Least Square Algorithm on Estimation of Vehicle Sideslip Angle and Road Friction. *Mathematical Problems in Engineering*, 2010:1–19, 2010.
- [Eic11] A. Eichberger. Contributions to Primary, Secondary and Integrated Traffic Safety. Habilitation thesis, 2011. Graz University of Technology.
- [EotEC09] Enterprise and Industry Directorate-General of the European Commission. Standardisation mandate addressed to CEN, CENELEC and ETSI in the field of information and communication technologies to support the interoperability of co-operative systems for intelligent transport in the European Community. Innovation policy M/453 EN, European Commission, 2009.
- [EotEC14] Enterprise and Industry Directorate-General of the European Commission. eCall - Automated emergency call for serious road accidents. Available at <http://ec.europa.eu/enterprise/sectors/automotive/safety/ecall/index.en.htm>, 2014. Accessed on 4.12.2014.
- [ER92] U. Eichhorn and J. Roth. Prediction and Monitoring of Tyre/Road-Friction. In *Proceedings of XXIV FISITA Congress*, pages 67–74. FISITA, 7-11 June 1992. London, UK.
- [ETR⁺10] A. Eichberger, E. Tomasch, R. Rohm, H. Steffan, and W. Hirschberg. Detailed analysis of the benefit of different traffic safety systems in fatal accidents. In *Proceedings of the annual EVU meeting*, pages 301–315. Europäische Vereinigung für Unfallforschung und Unfallanalyse (EVU), 14-16 October 2010. Prague, Czech Republic.
- [fSI99] International Organization for Standardization (ISO). ISO 3888-1: Passenger cars - Test track for a severe lane-change manoeuvre - Part 1: Double lane change. International standard, Technical Committee ISO/TC 22/SC 9, 1999.
- [fSI04] International Organization for Standardization (ISO). ISO 4138 - Passenger cars - Steady-state circular driving behavior - Open-loop test methods. International standard, Technical Committee ISO/TC 22/SC 9, 2004.

- [fSI11] International Organization for Standardization (ISO). ISO 8855:2011. Road vehicles - Vehicle dynamics and road-holding ability - Vocabulary. International standard, Technical Committee ISO/TC 22/SC 9, 2011.
- [GH04] H. Goertz and T. Huesemann. The intelligent Tyre - A vision for accident free traffic. In *Inproceedings of tyre.wheel.tech*. TÜV Süd, 7-8 December 2004. Munich, Germany.
- [Gmb14] GeneSys Elektronik GmbH. High Performance Fibre Optic Gyro Platform with DGPS for Vehicle Dynamics Testing. Available at <http://www.genesys-adma.de/adma.php?lang=2&ID=6935>, 2014. Accessed on 4.12.2014.
- [Gus97] F. Gustafsson. Slip-based tire-road friction estimation. *Automatica*, 33(6):1087–1099, 1997.
- [Har11] B. Hartmann. Emergency Brake & Steer Assist. Ein integriertes Fahrerassistenzsystem für Notsituationen. In *Proceedings of Symposium Reifen und Fahrwerk*. ÖAMTC, 4 October 2011. Vienna, Austria.
- [HE11] B. Heißing and M. Ersoy. *Chassis Handbook. Fundamentals, Driving Dynamics, Components, Mechatronics, Perspectives*. Vieweg+Teubner, 2011.
- [Hei94] H. Heinijoki. Kelin kokemisen, rengaskunnon ja rengustyypin vaikutus nopenskäryttäytymiseen (Influence of the Tyre and Condition of Tyres and Drivers' Perceptions of Road conditions on Driving Speed). Technical Report 19, Finnish Road Administration (FinnRA), Helsinki, Finland, 1994.
- [HG09] J. Hoffmann and J. Gayko. *Fahrerwarnelemente*, chapter 24, pages 343–354. *Handbuch Fahrerassistenzsysteme. Grundlagen, Komponenten und Systeme für aktive Sicherheit und Komfort*. Vieweg+Teubner, 1. edition, 2009.
- [Hir09a] W. Hirschberg. TMsimple: A simple to use tyre model. Technical report, Institute of Automotive Engineering, Graz University of Technology, 2009.
- [Hir09b] W. Hirschberg. Tyre - The Essential Component for Traction and Vehicle Dynamics. In *Proceedings of 9th European All-Wheel Drive Congress (EAWD)*. Magna Powertrain & Magna Steyr, 15-17 April 2009. Graz, Austria.

Bibliography

- [Hir13] W. Hirschberg. Vorlesungsskriptum Fahrzeugdynamik. Lecture notes, Institute of Automotive Engineering, Graz University of Technology, 2013.
- [HLGG06] J. Hsu, S. Laws, C. Gadda, and J. C. Gerdes. A Method to Estimate Friction and Slip Angle Using Steering Torque. In *Proceedings of ASME (IMECE)*, 5-10 November 2006. Chicago, Illinois, USA.
- [HMS03] C. Hide, T. Moore, and M. Smith. Adaptive Kalman Filtering for Low-cost INS/GPS. *The Journal of Navigation*, 56:143–152, 2003.
- [Hol92] J. Holzinger. Fahrdynamische Bestimmung der Kraftschlußverhältnisse und Sicherheitsreserve von Personenkraftwagen. Dissertation thesis, 1992. Graz University of Technology.
- [HPRS09] W. Hirschberg, F. Palcak, G. Rill, and J. Sotnik. Reliable Vehicle Dynamics Simulation in Spite of Uncertain Input Data. In *Proceedings of 12th EAEC European Automotive Congress*. Slovak Society of Automotive Engineers (SAITS), 2009. Bratislava, Slovakia.
- [HRW07] W. Hirschberg, G. Rill, and H. Weinfurter. Tire model TMeasy. *Vehicle System Dynamics*, 45(Suppl. 1):101–119, 2007.
- [HW12] W. Hirschberg and H. M. Waser. Kraftfahrzeugtechnik. Lecture notes, Institute of Automotive Engineering, Graz University of Technology, 2012.
- [IJF⁺05] L. Imsland, T.A. Johansen, T.I. Fossen, J.C. Kalkkuhl, and A. Suissa. Vehicle Velocity Estimation using Modular Nonlinear Observers. In *Proceedings of 44th Conference on Decision and control and the European Control Conference*, pages 6728–6733. IEEE Computer Society, 12-15 December 2005. Seville, Spain.
- [Ins10] European Telecommunications Standards Institute. Intelligent Transport Systems (ITS); European profile standard for the physical and medium access control layer of Intelligent Transport Systems operating in the 5 GHz frequency band. European Standard ETSI ES 202 663, V1.1.0, European Telecommunications Standards Institute (ETSI), January 2010.
- [ISAA10] V. Ivanov, B. Shyrokau, K. Augsburg, and V. Algin. Fuzzy evaluation of tyre-surface interaction parameters. *Journal of Terramechanics*, 47(2):113–130, 4 2010.

- [KGB14] M. Klomp, Y. Gao, and F. Bruzelius. Longitudinal velocity and road slope estimation in hybrid electric vehicles employing early detection of excessive wheel slip. *Vehicle System Dynamics*, 52(Suppl.):172–188, 2014.
- [KH09] T. Q. Khanh and W. Huhn. *Sichtverbesserungssysteme*, chapter 30, pages 448–470. Handbuch Fahrerassistenzsysteme. Grundlagen, Komponenten und Systeme für aktive Sicherheit und Komfort. Vieweg+Teubner, 1. edition, 2009.
- [KKP⁺10] A. Kerschbaumer, D. Kollreider, C. Prettenthaler, W. Hirschberg, G. Schagerl, and M. Peinsitt. About the Identification of Tyre Characteristics Based on Vehicle Dynamics Measurements. In *Proceedings of 10th Stuttgart International Symposium*, pages 233–233. Springer Vieweg, 16-17 March 2010. Stuttgart, Germany.
- [KL13] H. Kobialka and C. Lex. Accuracy of Friction Estimation during Driving. In IAV GmbH, editor, *7th Conference on Design of Experiments (DoE) in Engine Development*, volume in press, Renningen, 18.6-19.6. 2013. Expert Verlag. Berlin.
- [Kol09] D. Kollreider. Identifikation der Reifeneigenschaften als Grundlage zur Fahrdynamikbewertung. Dissertation thesis, 2009. Graz University of Technology.
- [Kol13] H. Kollienz. Entwicklung eines robusten Schätzers für Fahrzustandsgrößen für die Anwendung in Fahrerassistenzsystemen. Master’s thesis, 2013. Graz University of Technology.
- [KP09] S. Koskinen and P. Peussa. FRICTI@N. Final Report - Public. Deliverable 13 for the european commission, Technical Research Centre (VTT), 2009. Tampere, Finland.
- [Kra08] F. Kramer. *Passive Sicherheit von Kraftfahrzeugen. Biomechanik-Simulation-Sicherheit im Entwicklungsprozess*. Vieweg+Teubner, 2008.
- [LE11] C. Lex and A. Eichberger. Der Reifen als Einflussgröße für Fahrerassistenzsysteme und Fahrdynamikregelungen. In *Symposium Reifen und Fahrwerk*. ÖAMTC, 4 October 2011. Vienna, Austria.
- [LEH11] C. Lex, A. Eichberger, and W. Hirschberg. Systematische Bewertung von Methoden zur Ermittlung des Kraftschlussbeiwerts zwischen Reifen und

Bibliography

- Fahrbahn und deren Anwendungspotentiale in Fahrerassistenzsystemen. *ATZ Automobiltechnische Zeitschrift*, 12:992–997, 2011.
- [LHY04] C. Lee, K. Hedrick, and K. Yi. Real-time slip-based estimation of maximum tire-road friction coefficient. *IEEE/ASME Transactions on Mechatronics*, 9(2):454–458, 2004.
- [LKE13a] C. Lex, H. Kobialka, and A. Eichberger. Identification of the friction potential for the application in an automated emergency braking system. In *Proceedings of 13th Stuttgart International Symposium*, volume 2, pages 55–69. Springer Vieweg, 26-27 February 2013. Stuttgart, Germany.
- [LKE13b] C. Lex, H. Kobialka, and A. Eichberger. Wheel-individual estimation of the friction potential for split friction and changing friction conditions for the application in an automated emergency braking system. In *Chassis.tech plus 2013*, pages 609–621. Springer Vieweg, 13-14 June 2013. Munich, Germany.
- [LRNE13] C. Lex, A. E. Rojas Rojas, H. Niederkofler, and A. Eichberger. Evaluation of the potential of active powertrain, braking and steering systems based on in-wheel motors to improve the effectiveness of an evasive manoeuvre assistant. *International Journal of Powertrains*, 2(2/3):132–152, 2013.
- [Mun12] R. Mundl. Reifentechnik. Lecture notes, Institute of Automotive Engineering, Graz University of Technology, 2012.
- [MW04] M. Mitschke and H. Wallentowitz. *Dynamik der Kraftfahrzeuge*. Springer, 4. edition, 2004.
- [MYM⁺01] S.L. Miller, B. Youngberg, A. Millie, P. Schweizer, and J.C. Gerdes. Calculating Longitudinal Wheel Slip and Tire Parameters Using GPS Velocity. In *Proceedings of the American Control Conference (ACC)*, pages 1800–1805. IEEE Computer Society, 25-27 June 2001. Arlington, Virginia, USA.
- [Nie11] H. Niederkofler. Analyse radselektiv eingreifende Fahrdynamikregelsysteme für die Anwendung in elektromechanischen Corner-Modulen. Dissertation thesis, 2011. Graz University of Technology.
- [NLER11] H. Niederkofler, C. Lex, A. Eichberger, and A. E. Rojas Rojas. Potentialanalyse von aktiven Fahrwerks- und Antriebssystemen für die Anwendung in Fahrerassistenzsystemen in kritischen Fahrsituationen. In *Proceedings of*

13. *VDI-Tagung Reifen - Fahrwerk - Fahrbahn*. VDI Verlag, 25-26 October 2011. Hannover, Germany.
- [Off01] Office for Official Publications of the European Commission. European Transport Policy for 2010: time to decide. White paper COM(2001) 370 final, European Commission, 2001.
- [Off11] Office for Official Publications of the European Commission. Roadmap to a Single European Transport Area - Towards a competitive and resource efficient transport system. White paper COM(2011) 144 final, European Commission, 2011.
- [Pop09] V. L. Popov. *Gummireibung und Kontaktmechanik von Gummi*, chapter 16, pages 245–262. *Kontaktmechanik und Reibung. Ein Lehr und Anwendungsbuch von der Nanotribologie bis zur numerischen Simulation*. Springer, 1. edition, 2009.
- [Ran13] W. L. Randeu. Schneller als Blitzes: System der TU Graz ermöglicht Prognosen zum Straßenzustand. Available at <http://www.presse.tugraz.at/pressemitteilungen/2013/09.04.2013.htm>, 9.4.2013. Accessed on 20.04.2013.
- [Ras09] T. Raste. *Sichtverbesserungssysteme*, chapter 26, pages 395–403. *Handbuch Fahrerassistenzsysteme. Grundlagen, Komponenten und Systeme für aktive Sicherheit und Komfort*. Vieweg+Teubner, 1. edition, 2009.
- [Ray97] L. R. Ray. Nonlinear Tire Force Estimation and Road Friction Identification: Simulation and Experiments. *Automatica*, 33:1819–1833, 1997.
- [Ril06] G. Rill. First Order Tire Dynamics. In *Proceedings of III European Conference on Computational Mechanics Solids, Structures and Coupled Problems in Engineering*, 5-8 June 2006. Lisbon, Portugal.
- [Roi93] M. Roine. Driver behaviour in sharp curves and queues on main roads. Technical Report 87, Finnish Road Administration (FinnRA), Helsinki, Finland, 1993.
- [Roj12] A. E. Rojas Rojas. Passenger Vehicles with In-Wheel Motors: Fundamentals, Potentials and Limitations. Dissertation thesis, 2012. Graz University of Technology.

Bibliography

- [Rot92] J. Roth. Untersuchungen zur Kraftübertragung zwischen PKW-Reifen und Fahrbahn unter besonderer Berücksichtigung der Kraftschlußerkennung im rotierenden Rad. Dissertation thesis, 1992. Darmstadt University of Technology.
- [RPLG06] R. Rajamani, D. Piyabongkarn, J. Y. Lew, and J. A. Grogg. Algorithms for real-time estimation of individual wheel tire-road friction coefficients. In *Proceedings of American Control Conference (ACC)*, pages 4682–4687. IEEE Computer Society, 14-16 June 2006. Minneapolis, Minnesota, USA.
- [RPPL12] R. Rajamani, G. Phanomchoeng, D. Piyabongkarn, and J. Y. Lew. Algorithms for Real-time Estimation of Wheel Tire-Road Friction Coefficient. *IEEE/ASME Transactions on Mechatronics*, 17(6):1183–1195, 2012.
- [RS40] P. Riekert and T. E. Schunck. Zur Fahrmechanik des gummibereiften Kraftfahrzeugs. *Archive of Applied Mechanics*, 11(3):210–224, 1940.
- [Saa93] K. Saastamoinen. Kelin vaikutus ajokäyttäytymiseen ja liikennevirran ominaisuuksiin. Tielaitoksen selvityksiä (Effect of Road conditions on driving behaviour properties of the traffic flow). Technical Report 80, Finnish Road Administration (FinnRA), Helsinki, Finland, 1993.
- [SHB10] D. Schramm, M. Hiller, and R. Bardini. *Zweispurmodelle ohne Radaufhängungskinetik*, chapter 11.1, pages 277–291. Modellbildung und Simulation der Dynamik von Kraftfahrzeugen. Springer, 2010.
- [Sim06] D. Simon. *The particle filter*, chapter 15, pages 461–483. Optimal State Estimation. Kalman, H_∞ , and Nonlinear Approaches. John Wiley and Sons, 2006.
- [SM01] H. Steffan and A. Moser. PC-Crash, a simulation program for vehicle accidents. Technical manual, Mac Innis Engineering, October 2001.
- [SS90] M. Sistonen and A. Seise. Observation road investigation of winter maintenance. In *Proceedings of VIIIth International Winter Road Congress*, pages 113–121. Permanent International Association of Road Congresses (PIARC), 14-16 March 1990. Tromsø, Norwegen.
- [Sve07] J. Svendenius. Tire Modeling and Friction Estimation. Dissertation thesis, 2007. Lund University.

- [SZZ13] A.A.A. Salih, N.L.A.C.A. Zaini, and A. Zhahir. The Suitability of GPS Receivers Update Rates for Navigation Applications. *World Academy of Science, Engineering and Technology*, 7(6):214–221, 2013.
- [TS06] E. Tomasch and H. Steffan. ZEDATU - Zentrale Datenbank tödlicher Unfälle in Österreich - A Central Database of Fatalities in Austria. In *Proceedings of the International - Expert Symposium on Accident Research (ESAR)*, 1 September 2006. Hannover, Germany.
- [TSC06] M. Tanelli, S.M. Savaresi, and C. Cantoni. Longitudinal Vehicle Speed Estimation for Traction and Braking Control Systems. In *Proceedings of IEEE International Conference on Control Applications*, pages 2790–2795. IEEE Computer Society, 4-6 October 2006. Munich, Germany.
- [TSH⁺08] A. Tuononen, P. Sainio, C. Hartweg, T. Hüseman, S. Nord, A. Rautiainen, A. Nepote, F. Mancosu, and M. Liukkula. Tyre Sensing Approach for Friction Estimation in FRICTIN Project. In *Proceedings of 17. Aachener Kolloquium Fahrzeug- und Motorentchnik*, pages 647–658, 6-8 October 2008. Aachen, Germany.
- [Uch01] M. R. Uchanski. Road friction estimation for automobiles using digital signal processing methods. Dissertation thesis, 2001. University of California, Berkeley.
- [Urd12] J. Barace Urdánóz. Benefit of Driver Assistance Systems. Bachelor thesis, 2012. Graz University of Technology.
- [VdFM08] J. Villagra, B. d’Andréa-Novel, M. Fliess, and H. Mounier. Estimation of longitudinal and lateral vehicle velocities: an algebraic approach. In *Proceedings of American Control Conference (ACC)*, pages 3941–3946. IEEE Computer Society, 11-13 June 2008. Seattle, Washington, USA.
- [VdFM11] J. Villagra, B. d’Andréa-Novel, M. Fliess, and H. Mounier. A diagnosis-based approach for tire-road forces and maximum friction estimation. *Control Engineering Practice*, 19(2):174–184, 2 2011.
- [WA01] C. Wallman and H. Aström. Friction measurement methods and the correlation between road friction and traffic safety. A literature review. Technical Report 911A, Swedish National Road and Transport Research Institute (VTI), Linköping, Sweden, 2001.

Bibliography

- [Wat06] D. Watzenig. Bayesian inference for process tomography from measured electrical capacitance data. Dissertation thesis, 2006. Graz University of Technology.
- [WDS09] H. Winner, B. Danner, and J. Steinle. *Adaptive Cruise Control*, chapter 32, pages 478–521. Handbuch Fahrerassistenzsysteme Grundlagen, Komponenten und Systeme für aktive Sicherheit und Komfort. Vieweg+Teubner, 1. edition, 2009.
- [Web04] I. Weber. Verbesserungspotenzial von Stabilisierungssystemen im Pkw durch eine Reibwertsensorik. Dissertation thesis, 2004. Darmstadt University of Technology.
- [Web05] I. Weber. The Benefit of Tire and Friction adaptive Vehicle Control Strategies. In *Proceedings of Tire Tech Expo*. UKIP Media & Events, 22 May 2005. Cologne, Germany.
- [Weg09] M. Wegscheider. Modellbasierte Komfortbewertung von Fahrerassistenzsystemen. Dissertation thesis, 2009. Graz University of Technology.
- [WHW02] G. Rill W. Hirschberg and H. Weinfurter. User-Appropriate Tyre-Modelling for Vehicle Dynamics in Standard and Limit Situations. *Vehicle System Dynamics*, 38(2):103–125, 2002.
- [WHW09a] H. Winner, S. Hakuli, and G. Wolf. *Einleitung*, pages 1–2. Handbuch Fahrerassistenzsysteme Grundlagen, Komponenten und Systeme für aktive Sicherheit und Komfort. Vieweg+Teubner, 1. edition, 2009.
- [WHW09b] H. Winner, S. Hakuli, and G. Wolf. *Glossar*, pages 1–2. Handbuch Fahrerassistenzsysteme Grundlagen, Komponenten und Systeme für aktive Sicherheit und Komfort. Vieweg+Teubner, 1. edition, 2009.
- [Win09a] H. Winner. *Frontalkollisionsschutzsysteme*, chapter 33, pages 522–542. Handbuch Fahrerassistenzsysteme Grundlagen, Komponenten und Systeme für aktive Sicherheit und Komfort. Vieweg+Teubner, 1. edition, 2009.
- [Win09b] H. Winner. *Radarsensorik*, chapter 12, pages 123–171. Handbuch Fahrerassistenzsysteme Grundlagen, Komponenten und Systeme für aktive Sicherheit und Komfort. Vieweg+Teubner, 1. edition, 2009.

- [WWO97] C. Wallman, P. Wretling, and G. Öberg. Effects of Winter Road Maintenance. State-of-the-Art. Technical Report 423A, Swedish National Road and Transport Research Institute (VTI), Linköping, Sweden, 1997.
- [Zam95] J. Zamow. Messung des Reifenverhaltens auf unterschiedlichen Prüfständen. *VDI Berichte*, 1224:43–60, 1995.
- [ZLC11] L.-H. Zhao, Z.-H. Liu, and H. Chen. Design of a Nonlinear Observer for Vehicle Velocity Estimation and Experiments. *IEEE Transactions on Control System Technology*, 19(3):664–672, 2011.